This thesis has been modified and differs from the one that was originally approved and accepted for deposit with the Graduate College in the following way:

- Page v has been altered for confidentiality.

Date of modification: Oct. 2019

METAL-CAVITY SURFACE-EMITTING NANOLASERS

BY

CHIEN-YAO LU

DISSERTATION

Submitted in partial fulfillment of the requirements
for the degree of Doctor of Philosophy in Electrical and Computer Engineering
in the Graduate College of the
University of Illinois at Urbana-Champaign, 2012

Urbana, Illinois

Doctoral Committee:

Professor Shun Lien Chuang, Chair
Professor James Eckstein
Assistant Professor Lynford Goddard
Professor Jean-Pierre Leburton

ABSTRACT

Metal-cavity surface-emitting micro/nanolasers are proposed and demonstrated. The design uses metals as both the cavity sidewall and the top/bottom reflectors and maintains the surface-emitting nature. As a result of the large permittivity contrast between the dielectric and metal, the optical energy can be well-confined inside the metal nanocavity. Flip-bonding the device to a silicon substrate with a conductive metal provides efficient heat removal. Several excellent performance characteristics have been observed such as ultra-narrow linewidth, low thermal impedance, and circular beam shapes. The devices proposed and realized are substrate-free with transferability to other platforms. The size of the proposed structure can be further reduced without severe degradation in the performance. This work provides a detailed theoretical model starting from the waveguide analysis to full structure simulations by taking into account both the geometry and the metal dispersion. Several substrate-free metal-cavity surface emitters are demonstrated. Advanced metal-cavity surface-emitting microlasers with submonolayer quantum dots are used as the active medium. Fabrication and experimental data are reported for electrical injection metal-cavity quantum-dot surface-emitting microlasers at room temperature. Detailed studies are conducted of size-dependent cavity modes for future size reduction. This thesis presents the accomplishment of the first room temperature metal-cavity surface-emitting microlaser with the best performance among the existing metal-cavity lasers. A further size reduction strategy for future work will be discussed and analyzed theoretically.

To my parents, for their love and support.

ACKNOWLEDGMENTS

I would like to thank my adviser, Professor Shun Lien Chuang, for the great opportunity to work in his research group. Although we often had different opinions on research issues,I deeply appreciate his patience and support. I think it was lucky for me to join his group timely, I had the chance and freedom to setup a new lab environment with the accumulated knowledge from previous group members. Of course, I also benefited from his never ending jokes and stories. In addition, I would like to thank Professor Chuang's wife, Lolita, for the encouragement during my study here.

I appreciate the time and suggestions from my thesis committee members: Professor James Eckstein, Assistant Professor Lynford Goddard, and Professor Jean-Pierre Leburton.

Every study stage is an accumulation process. I learned a lot from everyone I worked with and, of course, from previous group members. Among all the group members, I am very indebted to Dr. Shu-Wei Chang for his guidance in research and life philosophy. Although he is a theoretician, the suggestions and discussions from him benefited me a lot in designing experiments. For the setup of equipment in the lab, I have to thank Prof. Donghan Lee for teaching me how to setup the Ti:Sapphire laser. My graduate student life would have been boring without officemates. I am grateful to my officemate Akira Matsudaira for help in experiment and many expected/unexpected interesting things, Daniel Zuo for Beerio-kart competition and lots of fun in his apartment, Meng Zhang for the help in calculation, Benjamin Kesler for making pleasant noise all the time (even though nobody paid attention to him) and naming the nano-coin laser, Thomas O'Brien for showing me what is d–r–a and his sensitive radar. Also, I would like to thank Chi-Yu Ni, Michael Pengfei Qiao, and Eric Wei for their support in some of the experiments and discussions. Besides current group members, I would like to thank previous group members I have worked with, Dr. Adam Petschke, Martin Mandl, Wendy Ou, and Andrew Millard.

In addition to our group members, I am deeply appreciated Professor Dr. Dieter Bimberg at Technical University of Berlin and his group members. Through the collaboration, I was able to learn the most advanced device design and measurement systems. I also thank the support from Prof. Bimberg to visit his group and research opportunities.

I would like to thank my parents and family for their support. Finally, I would like to thank my wife, [redacted], for all her understanding and support

TABLE OF CONTENTS

CHAPTER 1 INTRODUCTION 1
1.1 Trend of Laser Miniaturization 1
1.2 Issues with Current Technology 1
1.3 Current Status of Nanolasers 3

CHAPTER 2 METAL OPTICS AND ITS APPLICATIONS TO SEMICONDUCTOR LASERS 7
2.1 Introduction 7
2.2 Surface Plasma and Optical Mode Compressions 8
2.3 Issues for Applications 14

CHAPTER 3 FUNDAMENTALS OF METAL-CAVITY SURFACE-EMITTING NANOLASERS 15
3.1 Introduction 15
3.2 Metal-Cavity Nanocavities 16
3.3 Design Considerations 17
3.4 Fabry-Pérot Formalism and Comparison with FDTD and FEM 23

CHAPTER 4 METAL-CAVITY SURFACE-EMITTING MICROLASERS WITH DISTRIBUTED BRAGG MIRRORS 31
4.1 Configuration and Device Design 31
4.2 Process and Fabrication Technology 34
4.3 Results on 980 nm Metal-Cavity Surface-Emitting Microlasers 35
4.4 Results on 850 nm Metal-Cavity Surface-Emitting Microlasers 39

CHAPTER 5 METAL-CAVITY SURFACE-EMITTING NANOLASERS 48
5.1 Strategy for Size Reduction 48
5.2 Design of Metal-Cavity Surface-Emitting Nanolasers 48
5.3 Simulation Results of the Cavity Properties 52
5.4 Design Optimization of Metal-Nanocavity Lasers 58
5.5 Threshold Analysis and the Light Output Power 63

CHAPTER 6 ADVANCED METAL-CAVITY SURFACE-EMITTING MICRO- AND NANOLASERS 67
6.1 Metal-Cavity Quantum-Dot Surface-Emitting Nanolasers 67
6.2 Metal-Cavity Quantum-Well Surface-Emitting Nanolasers 79

6.3 Toward the Realization of Metal-Cavity Nanolasers 82

CHAPTER 7 OUTLOOK 84

REFERENCES 86

CHAPTER 1

INTRODUCTION

1.1 Trend of Laser Miniaturization

Since the invention of the first laser by Maiman in 1960 [1] and semiconductor lasers by Hall and three other groups [2–5] in 1962, the size of lasers has been reduced significantly. As shown in Fig. 1.1, ultra-small lasers such as VCSELs [6], microdisk lasers [7], and photonic crystal lasers [8] have been realized with electrical injection toward micro- and nanoscales during the past few decades. There are a lot of advantages of making ultra-small lasers. Properties such as low threshold currents and reduced power consumption, ultra-small footprint, and ultra-fast switching make nanolasers an excellent candidate for future hyper-uniform optical sources in photonic integrated circuits [9]. Currently communication signals onto and off of chips are still carried almost exclusively by electronic signals. The development in transmitting high speed electronic signals will eventually saturate for many reasons such as the transmission-line limit due to copper loss and the lack of high speed transducers in the terabits per second regime. Recent progress in photonics has paved a new way toward future high speed optical data communication architectures.

1.2 Issues with Current Technology

Due to the enormous increase in data transmission, electronic-based systems are saturating in their capability of carrying signals. The invention of world wide web leads to a rapid increase of digital information in our daily life. Telecommunication is gaining its own importance

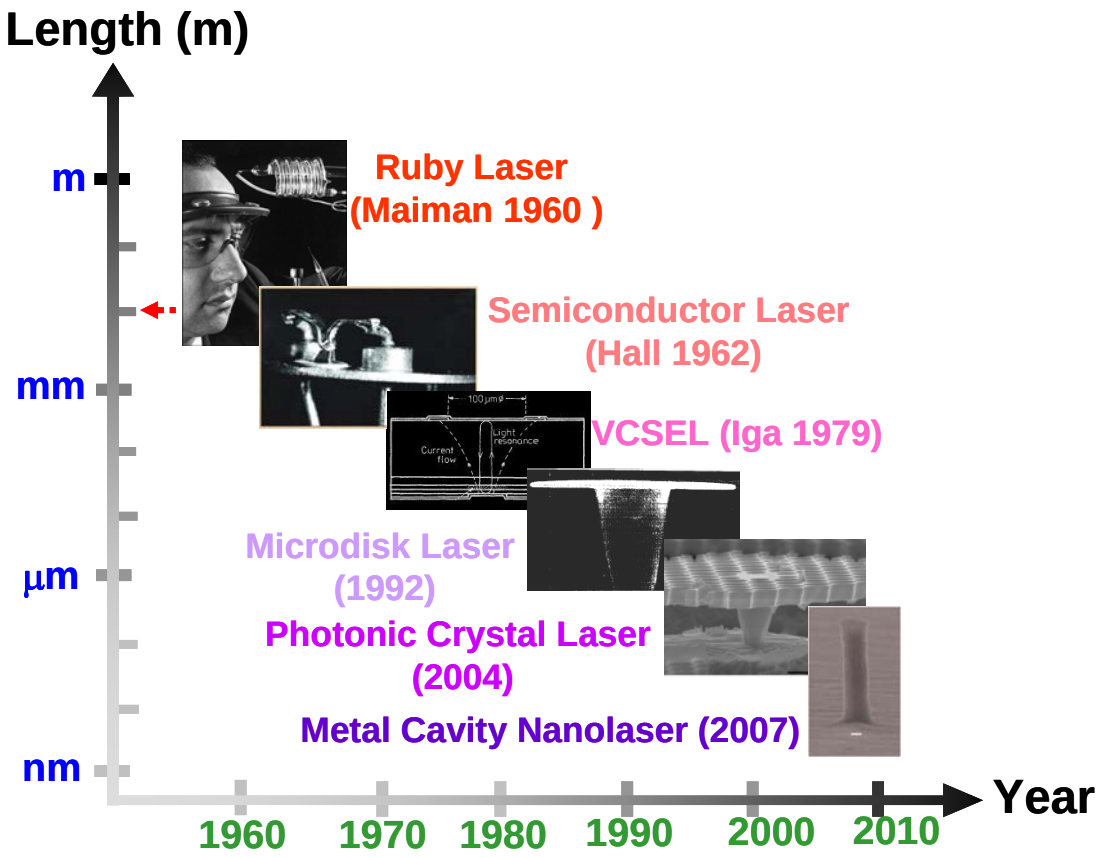

Figure 1.1: The trend of miniaturization of lasers [10]. The sizes of lasers have been greatly reduced since their invention in the 1960s. Recent metal-cavity nanolasers have demonstrated the possibility of breaking the diffraction limit toward subwavelength scale.

owing to the growing market of portable devices. People nowadays stay connected and share informations through the Internet. At the same time, the digital information is also growing in size. As shown in Fig. 1.2, the communication network has extended from commercial servers to personal computers, or even to mobile phones today. The data storage for different purposes also increase in its capacity. An energy-efficient, platform-insensitive, and mass producible inter/intra-chip architecture is in strong demand. In Fig. 1.3, Intel company predicted the saturation of the node size shrinkage as well as the high speed limit of the copper transmission line high speed limit, and is now developing new technologies (as shown in Fig. 1.4) to gradually migrate to a hybrid opto-electronic structure built by optical interconnect. However, due to the difficulties in integrating III-V mesoscopic emitters with

silicon, a platform-friendly source for carrying signals on chip is still immature.

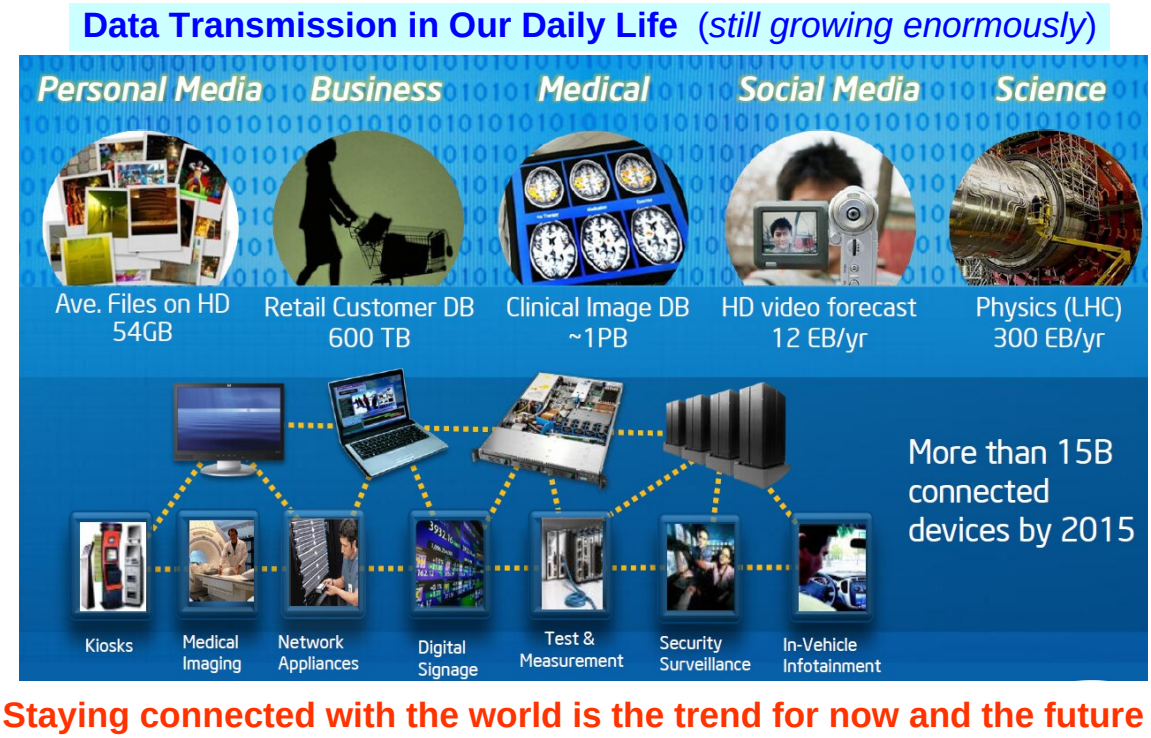

Figure 1.2: Data transmission and communication in our daily life. A rapid increase is expected in the near future. From [11].

1.3 Current Status of Nanolasers

Compact nanocavities such as photonic crystals or distributed Bragg reflectors (DBR) have been used to tightly confine the optical field in a tiny volume [8, 13]. Because at least a few pairs of these feedback structures are required to achieve a high quality factor, the sizes are usually several times larger than the wavelength. In the past few years, plasmonic structures have been extensively studied for photonic applications, especially for manipulating optical fields within a subwavelength scale. Metals exhibit a large negative permittivity in the optical regime due to the interaction of electromagnetic fields with free electrons. Nanolasers with a metal cavity can reduce the optical volume below the diffraction limit with the help of surface plasmon resonance [14]. Also, with the use of the metal, it is possible to have a crosstalk-

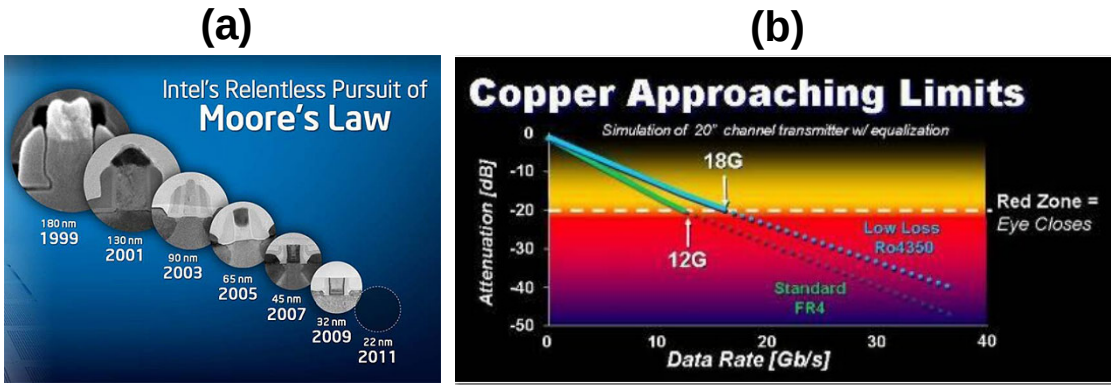

Figure 1.3: (a) Moore's la6 and the saturation of the node size shrinkage. (b) The copper transmission line limit over the chip distance. From [11].

free environment for dense photonic integration. The challenges for practical applications are how to realize continuous-wave operation by electrical injection at room temperature, light collection, performance, and integration. A few types of metal-cavity micro/nanolasers have been demonstrated [10, 15–24]. Designs with metal as parts of the cavity wall and feedback structures to compress the optical mode have been analyzed and demonstrated by optical pumping from low to high temperature [19–21]. Room temperature operation of metal-cavity lasers by optical pumping was demonstrated with an optimized plug-in structure for both mode confinement and metal loss reduction [21]. Figure 1.5 summarizes the performance and sizes of the state-of-the-art metal-cavity lasers. In 2007, Hill *et al.* demonstrated the first metal-cavity nanolaser under CW current injection at 78 K with the idea of using the cutoff mode to improve the mode confinement [22], and in 2009, the same idea was applied to Fabry-Pérot type laser which operated under pulsed current injection at 298 K [23]. Optically pumped nanopatch lasers at liquid-nitrogen temperature (77 K) by Yu et al. [19] and metal-coated nanopan lasers by Kwon et al at liquid helium temperature [20] further pushed the size to subwavelength in different dimensions. In 2010, Nezhad et al. [15] demonstrated a 3-dimensional subwavelength room temperature laser by optical pumping. In 2011, Lee et al. [25] also demonstrated an electrically-driven version of Nezhad's laser at low temperatures with the current injection structure. Due to the strong distortion of optical fields in certain

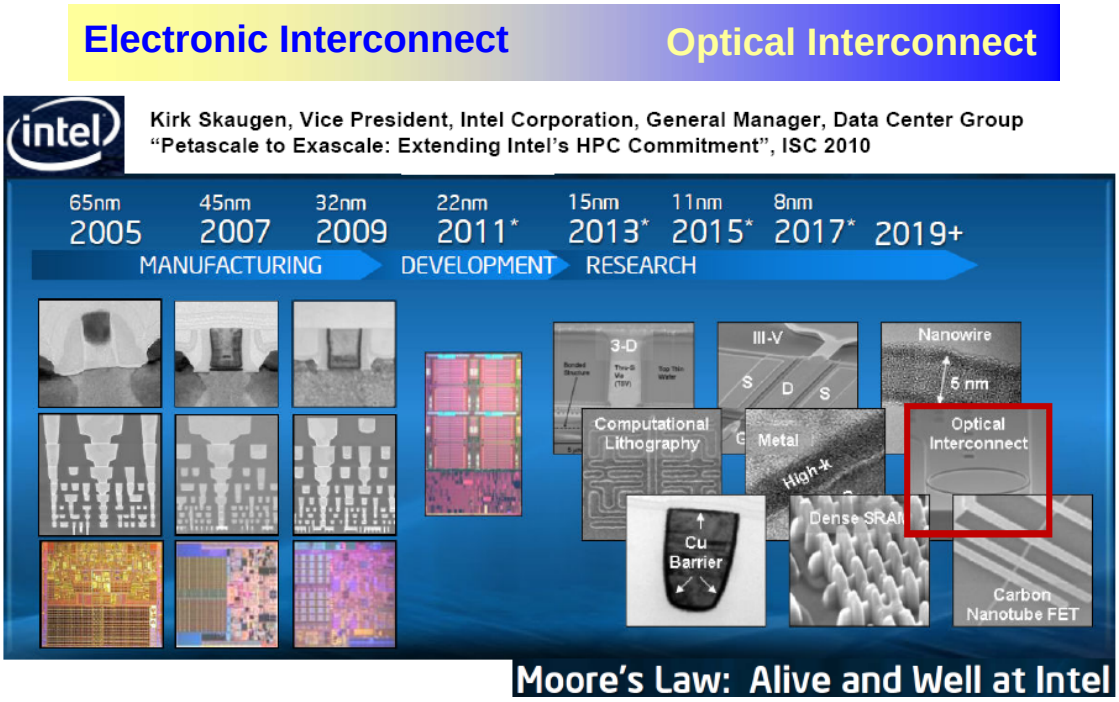

Figure 1.4: Intel's strate6y toward new generation technology. From [12].

directions, those metal-cavity nanolasers all suffer from low output power and poor beam shape. With the full coverage of metal, the light can only emit through the substrate, which makes the collection inefficient [21–23]. Vertical-cavity surface-emitting lasers (VCSELs) have been studied extensively during the past few decades, and significant improvements have been made such as small cavity volumes (for example, 1.5 μm diameter, $\backsimeq 8\lambda_0^3$ volume), high-power arrays, and high speed applications [26–28]. To further reduce the size of VCSELs, the high reflection window of DBR will become extremely sensitive to the modal dispersion, and the scattering loss from the sidewall irregularity will be a dominant issue. Recently, at UIUC we have proposed and realized the metal-cavity surface-emitting micro/nanolasers with DBR as part of the feedback structure under continuous-wave current injection at room temperature [10, 15–18]. With the surface-emitting configuration, the performance of metal-cavity lasers has been significantly improved, including microwatt output power, ultra-narrow linewidth, circular beam shape, and extremely low thermal impedance. From an application point of view, a compatible platform for advanced stacking with integrated circuits is also

an important issue [29]. The metal-cavity surface-emitting nanolasers are substrate-free with the transferability to other platforms. A further improvement with hybrid metal-DBR mirrors of these metal-cavity lasers is analyzed in Ref. [17] and demonstrated experimentally in Ref. [18]. Even though several metal-cavity lasers were demonstrated, the fundamental limit of the smallest realizable metal-cavity nanolaser is still under investigation.

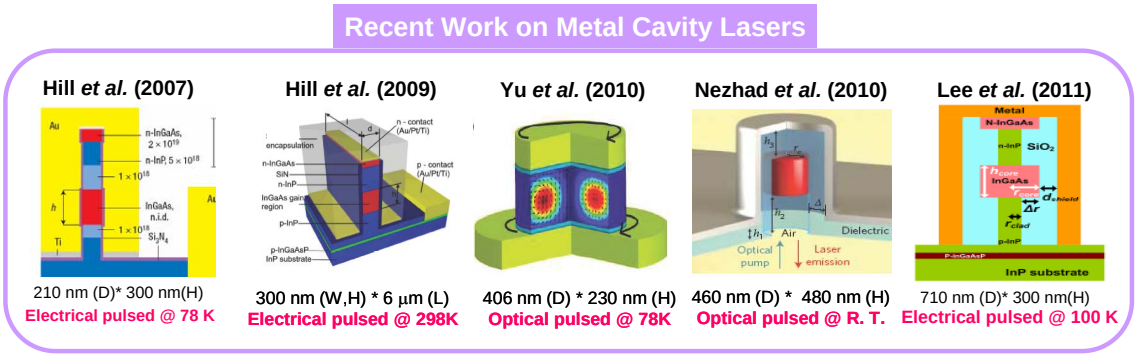

Figure 1.5: Recent works on metal-cavity lasers. Metal cavity electrical injection nanolaser was demonstrated by Hill et al. in 2007 [22] at 77 K and in 2009 [23] at 298 K. Ultrasmall optically pumped laser was demonstrated by Yu et al. at 77 K [19] and Nezhad et al. at room temperature in 2010 [21]. In 2011, Lee et al. demonstrated the electrical injection version of Nezhad's structure at 100 K [25].

CHAPTER 2

METAL OPTICS AND ITS APPLICATIONS TO SEMICONDUCTOR LASERS

2.1 Introduction

Electrons inside metals react as a plasma when interacting with electromagnetic waves, and the corresponding plasma behavior gives rise to the large negative permittivity at optical frequencies. The large and negative permittivity of metal allows the electromagnetic excitations to propagate at the interface as a surface wave (i.e. surface plasmon polariton) and more importantly functions as a barrier into which the optical energy decays evanescently. For this reason, when it comes to a dielectric cavity for confining the electromagnetic energy, metals are always one of the best choices as the cavity walls for tight confinement. In the optical regime, the ohmic loss from inelastic electron movement inside the metal increases. Even though a good confinement can still be made for a large discontinuity of permittivity, issues of efficiency should be solved for practical applications. During the past few decades, as a result of advances in nanofabrication, several ideas such as photonic crystals and distributed feedback structures have been proposed and realized to have a better control over the photons. Although the optical fields are well-controlled in these structures, the size and long periods make the whole device much larger than the wavelength and may not be the best choice for bridging the gap between electronic platform and photonic ones due to size mismatch. In order to further reduce the optical volume while keeping the overall size within a wavelength or even subwavelength scale, metals are proposed for future photonics and optical interconnects.

2.2 Surface Plasma and Optical Mode Compressions

2.2.1 Metal optics and surface plasma

The basic idea of metal optics can be understood by studying the single dielectric/metal interface problem. Considering a slab composed of metal and dielectric on each side as shown in Fig. 2.1(a), the field at the interface is determined by the boundary conditions of the Maxwell's equations:

$$\hat{n} \times \mathbf{E_m} = \hat{\mathbf{n}} \times \mathbf{E_d} \tag{2.1a}$$

$$\epsilon_m \hat{n} \cdot \mathbf{E_m} = \epsilon_\mathbf{d} \hat{\mathbf{n}} \cdot \mathbf{E_d} \tag{2.1b}$$

where ϵ_m and ϵ_d are the permittivities of the metal and the dielectric. To properly include the plasma behavior of metal, permittivitiy can be modeled with Drude electron model [30],

$$\frac{\epsilon_m(\omega)}{\epsilon_0} = \epsilon_\infty - \frac{\omega_p^2}{\omega^2 + i\gamma\omega} \tag{2.2a}$$

$$= \epsilon_\infty - \frac{\omega_p^2(\omega - i\gamma)}{\omega(\omega^2 + \gamma^2)} = \epsilon_r(\omega) + i\epsilon_i(\omega) \tag{2.2b}$$

where ω is the angular frequency, ω_p is the metal bulk plasma frequency, and ϵ_m can be

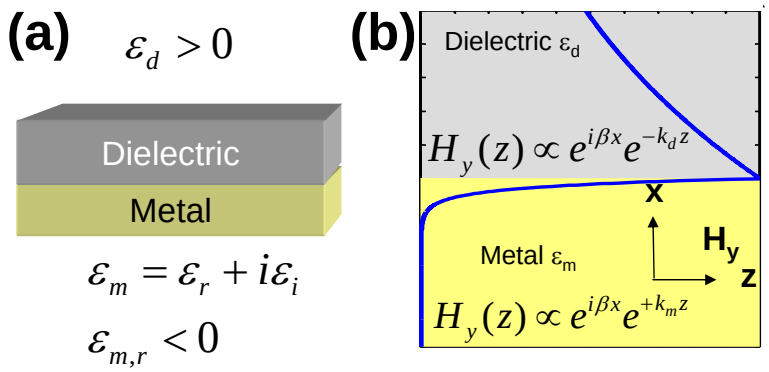

Figure 2.1: (a) Illustration of an interface formed of dielectric and metal slabs. The metal permittivity is a complex and represented by $\epsilon_r + i\epsilon_i$ with a negative ϵ_r. (b) A transverse magnetic (TM) mode supporting a surface-wave at the interface. An exponential decay tail into both regions shows the energy confinement at the interface.

further separated to

$$\frac{\epsilon_r(\omega)}{\epsilon_0} = \epsilon_\infty - \frac{\omega_p^2\tau^2}{1+\omega^2\tau^2} \tag{2.3a}$$

$$\frac{\epsilon_i(\omega)}{\epsilon_0} = \frac{\omega_p^2\tau}{\omega(1+\omega^2\tau^2)} \quad (\text{where } \tau = \frac{1}{\gamma}) \tag{2.3b}$$

The limiting cases are

$$\begin{cases} \epsilon_m \to \infty i & \text{as } \omega \to 0 \\ \epsilon_m \to \epsilon_\infty \epsilon_0 & \text{as } \omega \to \infty \end{cases} \tag{2.4}$$

For frequencies far below the plasma frequency ω_p, the electrons respond properly to the slow field variation and create an opposite field; as a result, the metal behaves like a perfect electrical conductor with permittivity of ∞i. However, at very high frequencies, the electrons fail to catch up with the field variation and the effects are canceled. The resulting property will be the same as the background permittivity ϵ_∞. In optical range, the real part of the permittivity is usually negative with a small imaginary part corresponding to the ohmic loss of the electrons inside metals. For example, the relative permittivity ϵ_m/ϵ_0 of gold at 1.55 μm is $-93.04 + 11.10i$. To be suitable for photonic application, metals with a large negative real part and a close to zero imaginary part of permittivity should be considered. Figure 2.1(b) shows a magnetic field pattern of the surface wave supported at the interface (TM mode). The exponential decay tail into both the metal and the dielectric region further proves its surface wave properties and the energy confinement at the interface.

2.2.2 Optical mode compression in metallic waveguides

Considering a simple structure composed of dielectric slabs with a high permittivity guiding region $\epsilon_d = 11.56\epsilon_0$ and an outer low permittivity cladding region $\epsilon_{d,low} = 10.5625\epsilon_0$, as shown in Fig. 2.2(a), and a similar structure (b) with metal cladding ($\epsilon_m = -100\epsilon_0$), the relative electric field intensities of various guiding thicknesses are plotted in Fig. 2.3 for TM modes for a wavelength of 1.55 μm. For the dielectric slab waveguide, a long decay tail is

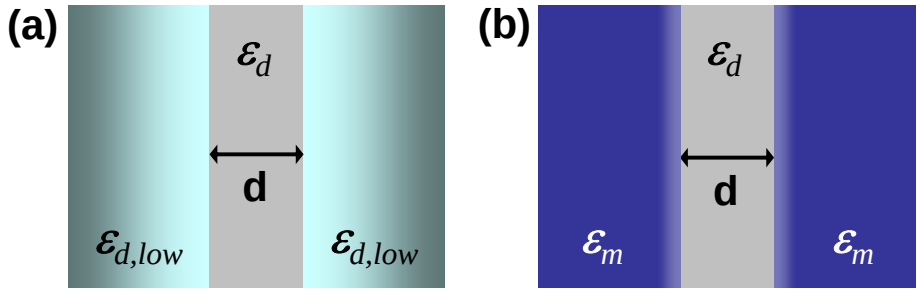

Figure 2.2: (a) A dielectric slab waveguide composed of a guiding layer with permittivity ϵ_d and a cladding layer with permittivity $\epsilon_{d,low}$. (b) A metallic slab waveguide of similar structure with the metal with permittivity ϵ_m as the cladding layer. d is the thickness of the waveguide.

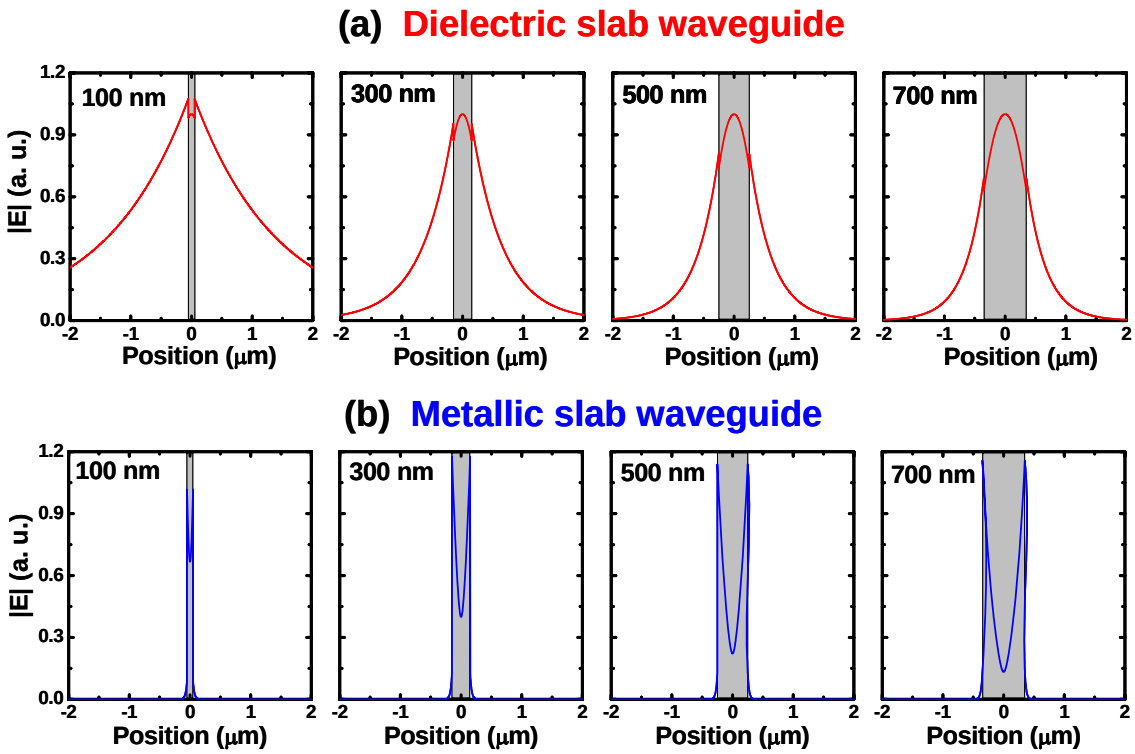

Figure 2.3: (a) The electric field intensity $|\mathbf{E}|$ profiles of a dielectric slab waveguide with different thickness at 1.55 μm wavelength. The permittivities are $\epsilon_d = 11.56\epsilon_0$ and $\epsilon_{d,low} = 10.5625\epsilon_0$.(b) The electric field intensity $|\mathbf{E}|$ profiles of a metallic slab waveguide of similar structure with the metal with a permittivity $\epsilon_m = -100\epsilon_0$ as the cladding layer. d is the thickness of the waveguide. A strong optical energy confinement is observed for the metallic waveguide case while a significant leakage of the field out of the waveguide region occurs for dielectric ones.

observed for all cases, especially when the waveguide width d is approaching or smaller than the effective wavelength inside the slab. The decay rate outside of the waveguide becomes slower for smaller d due to the weak guiding effect. As for the metallic waveguide, the large permittivity discontinuity results in a tight optical confinement and gives rise to a fast decay tail into the metal (*skin depth*). More importantly, the continuity of the normal **D**-field at the interface further enhances the field inside the waveguide. As a result, the metallic waveguide shows a property of compressing the optical energy well inside the waveguide even in the subwavelength region. Figure 2.4 compares the energy confinement inside the dielectric slab waveguide and its counterpart, the metallic slab waveguide. The energy stored

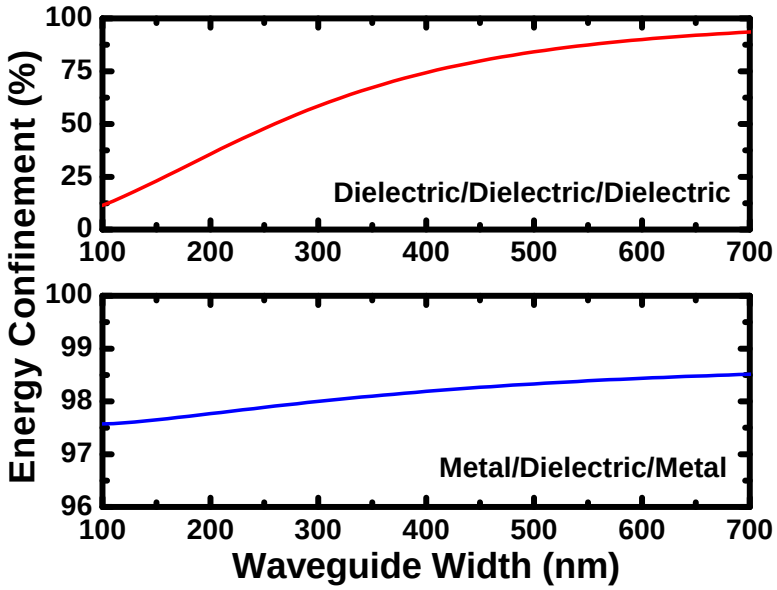

Figure 2.4: Energy confinement inside the guiding region as a function of the guiding layer thickness of a dielectric slab waveguide and a metallic one. For the dielectric case, the energy inside drops quickly when the size approaches the wavelength; however, the metallic case can hold the energy over 97% even when the thickness is in the subwavelength region.

in the guiding region of a dielectric waveguide drops dramatically when the size approaches the wavelength and has less than 20% for $d = 100$ nm, while the metallic ones can hold more than 97% for the same waveguide thickness. In general, the trade-off of tight confinement is the high optical loss due to the penetration of fields into metal. Figure 2.5 shows an example of an open cavity formed by a gold bowtie resonant nanoantenna. The intense optical field

induced at the tips of the dimers helps the light localization within the tip region and forms a cavity without a definite cavity wall. As shown in the simulation field pattern in (a), the field strongly concentrates at the tip region within a cylinder volume of $\sim 2.5 \times 10^{-5}$ μ m^3. In Fig. 2.5(b), the dark field scattering spectroscopy shows a resonance wavelength of this nano structure at 1.1 μm with a full-width-at-half-maximum (FWHM) of 150 nm which leads to a estimation of quality factor $Q = \lambda/\Delta\lambda = 7.33$. The low quality factor comes from the field penetration of optical fields into the metal, which is roughly the skin depth ($\sim 20 - 30$ nm in this case). Even though the optical energy is confined in this 100 nm region, the non-negligible penetration into metals dissipates a significant amount of energy, and, thus, reduces the quality factor.

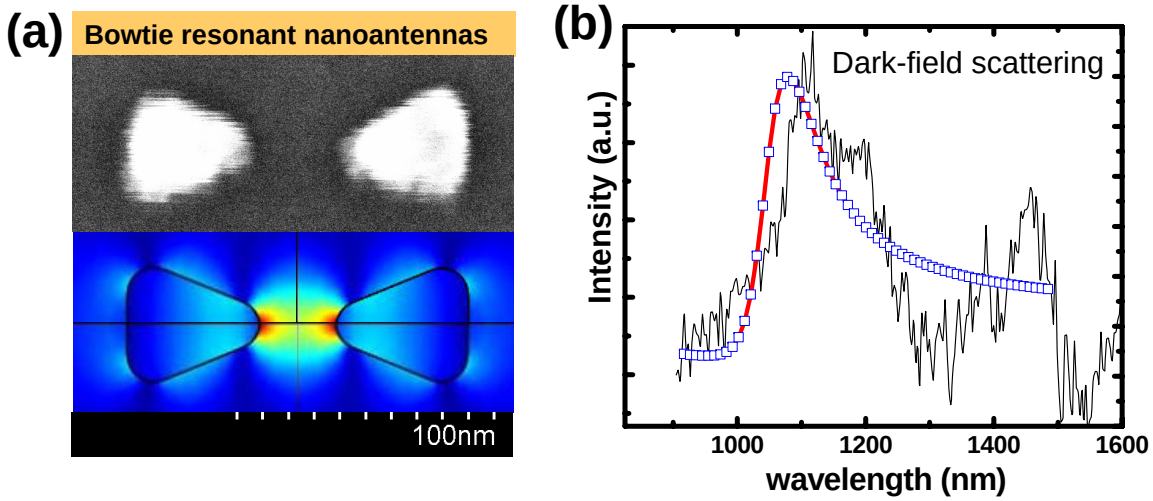

Figure 2.5: Bowtie resonant nanoantennas. (a) (top) The scanning electron micrograph (SEM) of bowtie nanoantenna formed of Au nanodimers atop GaAs substrate. (bottom) The simulated electric field intensity E of the fabricated structure at resonance. The strong localization near the tip region forms an open cavity. (b) The dark field scattering spectroscopy taken at room temperature. The result shows a good agreement with our simulation. The quality factor is estimated to be ~ 7.5.

2.2.3 Crosstalk reduction for dense photonic integrations

The large permittivity contrast between semiconductor and metal enhances strongly the optical confinement as compared to those of conventional dielectric cavities with a large size.

Besides the size issue, the distance between devices also determines the capacity of photonic integration. The electronic fabrication technology has emerged to a much smaller dimension than a wavelength of optical communication window. The crosstalk will definitely put a barrier on future dense optical integration. Metal, with a tiny skin-depth in electromagnetic waves, can function as a barrier that isolates individual devices. In Figure 2.6 (a) and (c), a simulation result is given to show the shielding effect of metal for isolating devices. Without metal shielding, as shown in Fig. 2.6(b) and (d), the waveguide mode coupling starts to become obvious when the distance is smaller than 300 nm. However, silver-shielded waveguide shows no obvious coupling even within 100 nm distance. This shielding effect from metal greatly boosts the capacity of ultra dense photonic integration.

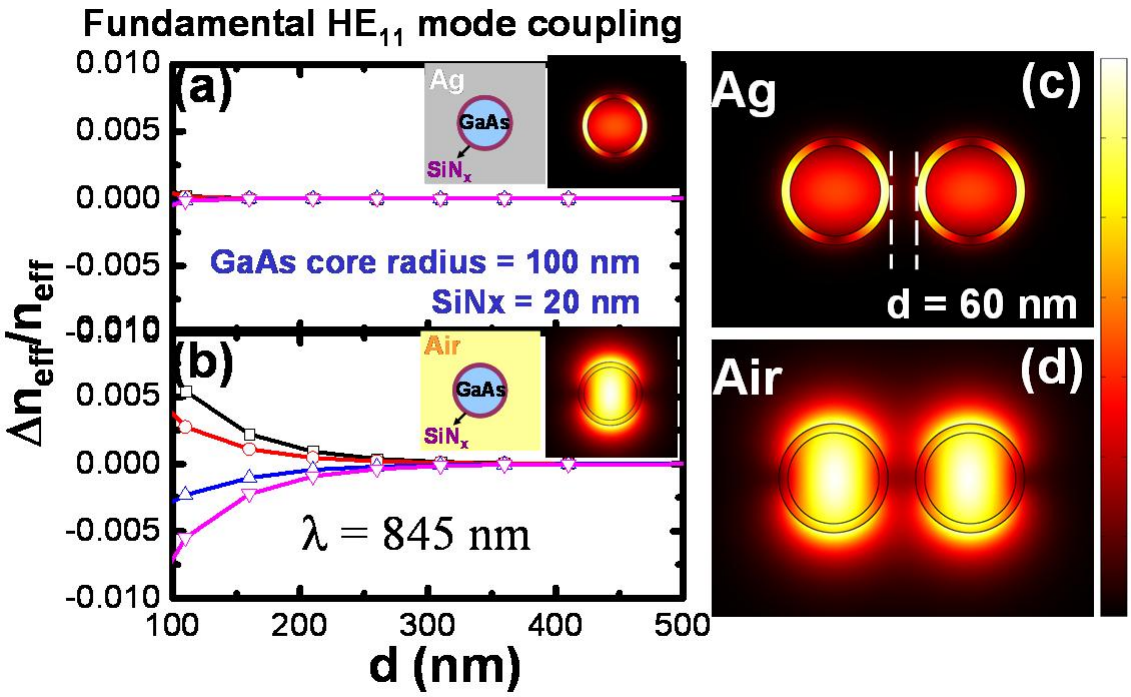

Figure 2.6: (a) and (b) Effective index change of the HE_{11} mode at 845 nm as a function of distance between two waveguides. (a: silver-coated) (b: air-surrounded) (Inset: field patterns $|\mathbf{E}|$ of an isolated waveguide). A clear coupling is observed for the air-surrounded waveguides when d $\leq$ 300 nm, and no coupling observed for silver-coated ones. (c) Field pattern $|\mathbf{E}|$ of two adjacent silver-coated waveguides with d = 60 nm. No field coupling is observed. (d) Field pattern $|\mathbf{E}|$ of two adjacent air-surrounded waveguide with d = 60 nm. Strong field leakage out of waveguide contributes to the coupling.

2.3 Issues for Applications

Although metals can help efficient optical mode compression, the non-negligible imaginary part of the permittivity at optical frequency, especially at room temperature, dissipates the energy and is not favorable for photonic applications, which often require a low loss environment. For active devices, such as lasers or light emitting diodes, the minimization of the metal ohmic loss is essential to the device performance. Several ideas have been proposed to reduce both the radiation loss and metal loss while keeping the volume small. One of the ideas is the application of an optical buffer layer, for example, a thin silicon nitride to allow field decay inside the lossless optical buffer before entering the lossy metal. The discussion of optical buffer to reduce the loss can be found in Sec. 3.3.1. Other ideas such as a cutoff plug-in section of waveguide for reducing the light penetration into the metal [31] or mode mismatch by introducing a discontinuity in propagation direction [22] may also reduce the laser threshold due to the improvement in the mirror reflectivity.

CHAPTER 3

FUNDAMENTALS OF METAL-CAVITY SURFACE-EMITTING NANOLASERS

3.1 Introduction

Metals, as highly reflective materials, are good and simple feedback reflectors to form an optical cavity. They can serve as both contacts and cavity walls. Due to the large permittivity contrast between metals and dielectrics, metal-cavities can confine the optical energy well inside the cavity wall formed of metals. The negative permittivity of metals makes the energy more confined within a few tens of nanometers and thus can keep the whole cavity size at a minimum. However, a full metal-coverage cavity is not yet available for semiconductor laser application. Several types of metal-cavities have been proposed and realized. Hill demonstrated the first metal-cavity nanolasers with a cut-off waveguide as a feedback structure [22]. The cut-off concept has been successfully applied to cavities with circular and pillar structures and all lased under pulsed electrical injection at cryogenic temperatures [22, 23]. Recently, nearly room-temperature operation was reported by Arizona State University with the same structure [32]. Current nanolasers still rely on cut-off structures or periodic feedback structures to confine the optical volume. A further size reduction will eventually become problematic due to the wave nature of the photon, especially when the size approaches a half wavelength in all three directions.

3.2 Metal-Cavity Nanocavities

In order to implement a practical nanodevice, we designed the surface emitting configuration for metal-cavity nanolasers with the following major innovations: *i*) Substrate-free configuration to avoid propagation or scattering loss through the thick substrate and to remove the thermal barrier from the substrate. *ii*) Metal-defined cavity and complete coverage with metal for efficient optical mode confinement, efficient heat removal, and most importantly, a crosstalk-free environment for future high density photonic integration. *iii*) Circular cavity top-emitting design, which serves as the best shape of laser sources compared to a slit or rectangle that usually distorts the optical field in certain directions and is not efficient for practical usage. *iv*) Transferability to all existing platforms via a substrate-free metal cavity. The great thing about substrate-free is that the design allows our devices to be transferred to all kinds of substrates, including solid semiconductors (i.e. GaAs/Si), metals (i.e. copper, aluminum), and soft materials (i.e. metal-foil, plastics). This practice broadens the application areas of semiconductor lasers and is the key feature that has been realized recently on metal-cavity microlasers [15,16]. The proposed design not only eases the necessity of specific substrates but also is flexible in further size reduction without serious performance degradation. Although metal-cavity lasers with modal cut-off structures have been demonstrated [22, 23] successfully, the design rule strongly depends on the geometry and small refractive index mismatch between material guiding and cut-off regions. A precise control on the nanometer scale is necessary in order to balance the feedback and output power. In other structures, like nanopatches, due to its emission from side walls, the geometry affects the interference in the normal direction and makes the beam quality unstable. The proposed structure of the fundamental HE_{11} mode with mirrors at both ends eases the above-mentioned drawbacks and is suitable for future size reduction.

3.3 Design Considerations

3.3.1 Metal-clad waveguide

In a metal-clad inhomogeneous circular waveguide, the normal modes are either hybrid mode (HE_{mn} or EH_{mn}) for azimuthal order $m \geq 1$ or transverse mode (TE_{0n} or TM_{0n}) for $m = 0$, where n represents the order of radial distribution [33, 34]. Figure 3.1 shows such a circular waveguide with an inhomogeneous radial distribution ($In_{0.53}Ga_{0.47}As$ semiconductor core with a SiN_x shell and a silver metal wall) and its corresponding mode patterns (in the basis of $cos(m\phi)$ and $sin(m\phi)$) calculated by the finite element method (FEM). To have a large modal gain, a mode with good overlap between optical field and core gain material should be considered. Figure 3.1 lists our calculated field distribution (electric field norm: $|\mathbf{E}|$; magnetic field norm: $|\mathbf{H}|$) of the first 5 lowest order modes (HE_{11}, TM_{01}, HE_{21}, TE_{01}, EH_{11}) at 1550 nm with a core radius of 250 nm and a shell thickness of 50 nm. For the transverse mode TM_{01} (TE_{01}), both the magnetic (electric) field and its resulting time-averaged power along the waveguide direction (P_z) have a node at the center due to the nature of Bessel functions and their lack of longitudinal magnetic (electric) field components. Since the periphery of the waveguide usually degrades during fabrication, configurations with a node at the center will result in an inefficient interaction between the gain materials and the optical fields when propagating back and forth along the z-direction. Optical modes with $m > 1$ are not suitable here because of their whispering-gallery behaviors, which usually experience more perturbation from the periphery than the lower order modes and have a power node at the center.

A simplified perfect electric conductor (PEC) model can be used to capture the guiding properties of a circular metallic waveguide. For a homogeneous metallic waveguide, the propagation constant k_z should satisfy the following equation,

$$k_\rho^2 + k_z^2 = \omega^2 \mu \epsilon_{core} = \left(\frac{2\pi}{\lambda_0} n_{core}^2 \right) \tag{3.1}$$

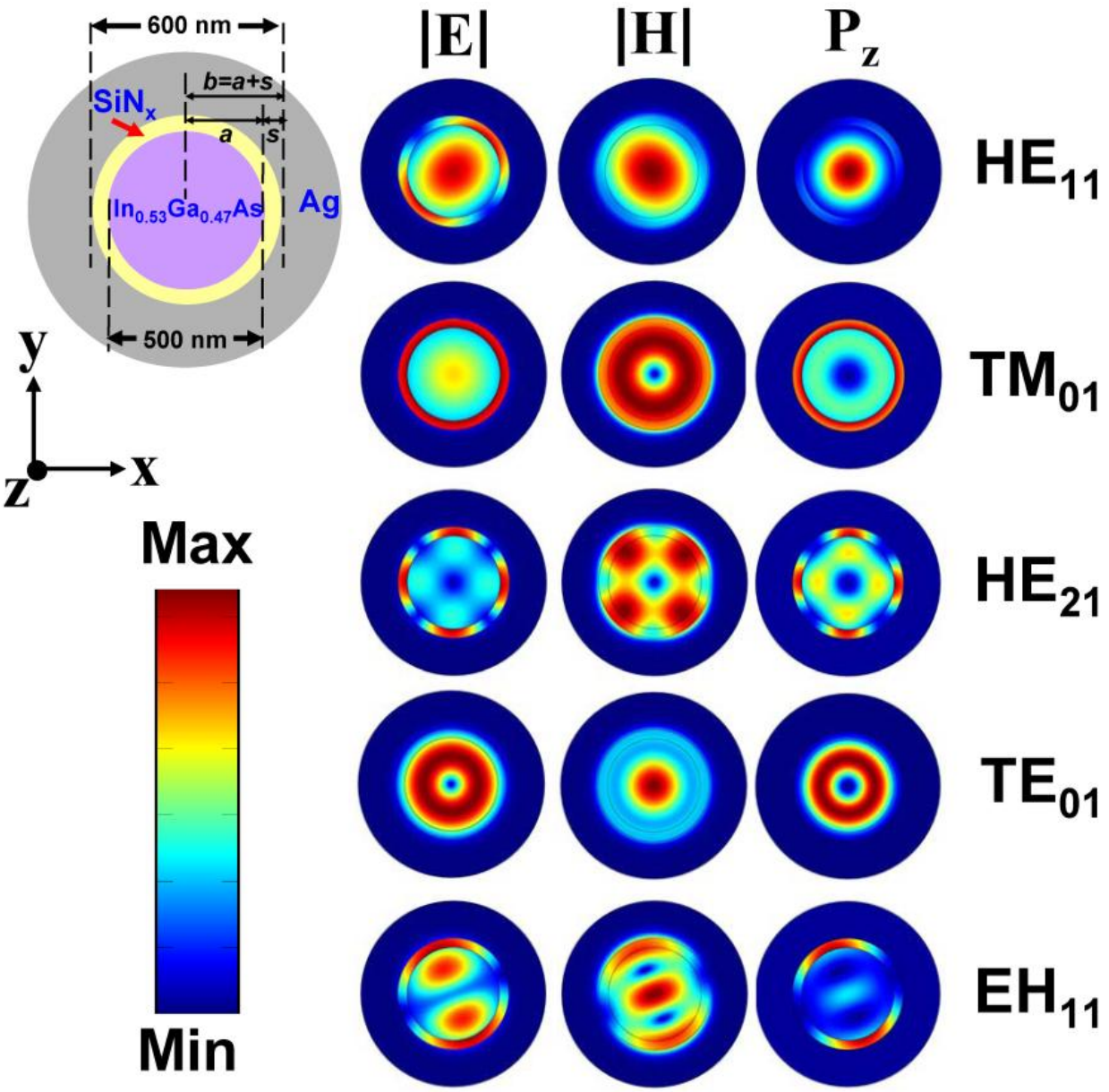

Figure 3.1: Mode patterns of a circular metallic waveguide with a core-shell structure inside, calculated by the finite element method (FEM). Top left: Cross-sectional view of the waveguide layered structure. Silver is used to surround the circular waveguide with an $In_{0.53}Ga_{0.47}As$ core of radius $a = 250$ nm and a thin SiN_x shell layer of thickness $s = 50$ nm. Five lowest order mode patterns ($|\mathbf{E}|$, $|\mathbf{H}|$, and P_z) are plotted correspondingly. Power nodes at the waveguide center are observed in TM_{01}, HE_{21}, and TE_{01} modes.

where $k\rho$ is equal to χ_{mn}/b, χ_{mn} is the root of Bessel functions or their derivatives, b is the outer radius as shown in Fig. 3.2, ϵ_{core} is the permittivity of the homogeneous waveguide core, and n_{core} and λ_0 are the refractive index of the core and the free space wavelength. The mode cutoff occurs at $k_z = 0$, or equivalently,

$$\left(\frac{2\pi}{\lambda_c} n_{core}\right) = k_\rho = \chi_{mn}/b \tag{3.2}$$

The resulting cutoff wavelength (λ_c) is then equal to $2\pi b n_{core}/\chi_{mn}$. For a PEC waveguide with a homogeneous cross-section, the value $\chi_{mn}\lambda_c/2\pi n_{core} b$ should be 1.

In the descending order of cutoff wavelengths, the dominant modes are HE_{11}, TM_{01}, HE_{21}, TE_{01}, and EH_{11}. Figure 3.2(a) shows the cutoff wavelengths (λ_c) as a function of the outer radius (b) calculated with a SiN_x shell thicknesses of 50 nm and material (metal and semiconductor) permittivities from Ref. [35, 36]. To ensure a propagating behavior inside the cavity within the window of material emission spectrum, the radius with a cutoff wavelength longer than the emission wavelength should be chosen. For example, at around 1550 nm (corresponding to $In_{0.53}Ga_{0.47}As$ emission), the HE_{11} (EH_{11}) mode can only propagate when the radius (b) is larger than 130 nm (260 nm) as shown in Fig. 3.2(a). The fundamental mode HE_{11} has the longest cutoff wavelength for the same size, and thus can potentially be a good choice in designing an optical cavity with a minimal transverse dimension [37].

Figure 3.2(b) plots the value $\chi_{mn}\lambda_c/[2\pi n_{core}(b+\Delta)]$ as a function of the outer radius b, where χ_{mn} is the root of Bessel functions or their derivatives (HE_{11}: 1.84, TM_{01}: 2.405, HE_{21}: 3.05, TE_{01}: 3.83, and EH_{11}: 3.83), Δ is the penetration skin depth, and n_{core} is the core ($In_{0.53}Ga_{0.47}As$) refractive index. The values deviate from unity as the radius decreases. It means that the approximation by a homogeneous circular waveguide with a real dispersive metal replaced by a PEC wall and receding by the penetration depth fails in this region. This discrepancy comes from the non-negligible permittivity transition from the semiconductor core to the insulator SiN_x shell. Moreover, for hybrid modes which should not occur in a homogeneous waveguide with a PEC wall, the approximation will hold only when the radius

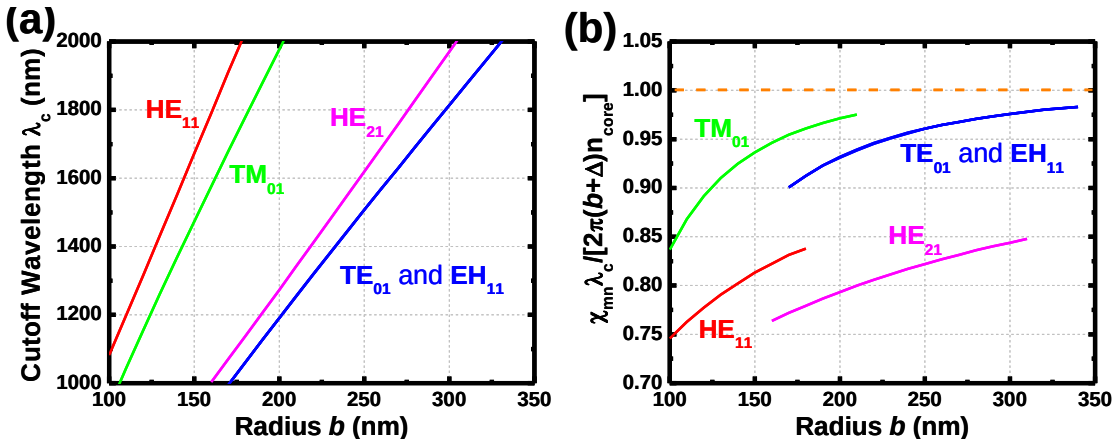

Figure 3.2: (a) Cutoff wavelengths of different modes as a function of core radius. The fundamental mode HE11 has the longest cutoff frequency among all the other modes and can be used to design a cavity of a minimal radial dimension. (b) $\chi_{mn}\lambda_c/[2\pi n_{core}(b+\Delta)]$ as function of core radius. χ_{mn} is the root of Bessel functions or their derivatives (HE_{11}: 1.84, TM_{01}: 2.405, HE_{21}: 3.05, TE_{01}: 3.83, and EH_{11}: 3.83). The dashed line represents the prediction by the use of homogeneous waveguide with a receded PEC wall by a skin depth . The actual cutoff wavelength will be close to the prediction when the wavelengths are long enough such that the thin cladding layer becomes negligible.

is large enough for the hybrid modes to be considered as transverse modes and the cutoff wavelength is long enough to ignore the shell thickness. In an inhomogeneous waveguide such as a core-shell structure (assuming $n_{core} > n_{shell}$ in this paper) with a real metal surrounding in Fig. 3.1, there are three propagating modes in the waveguide: surface (plasmonic) mode, core-shell mode, and core (dielectric or fiber-optical) mode. The surface mode exists when the propagation constant k_z of the mode is larger than $k_{core} = 2\pi n_{core}/\lambda_0$, where λ_0 is the free space wavelength, or equivalently, the effective index n_{eff} (defined by $k_z = (2\pi n_{eff}/\lambda_0)$) is larger than the material indices inside the waveguide ($n_{shell} < n_{core} < n_{eff}$). In surface mode, the optical energy is concentrated near the metal-dielectric interface and decays exponentially into both regions. As a result of large field penetration into metal, this mode usually suffers from a high propagation loss. The core-shell mode exists when $n_{eff} < n_{shell}$, and in this case, a significant field leaks out of the core region and propagates (with a real k_ρ) inside the shell region. The optical power is actually guided in both the core and the shell regions. The core mode represents $n_{shell} < n_{eff} < n_{core}$, which is the normal propagation mode (or

dielectric mode or fiber-optical mode) with power propagation mostly inside the core with an evanescent decay to the shell region, and is expected to be the most lossless among all three modes. The design with the core mode not only helps reduce the sidewall metal loss but also concentrates the energy more into the center region. Figure 3.3(a) shows a two-dimensional (2D) plot of the effective index n_{eff} as a function of radius a with a constant SiN_x thickness ($s = 50$ nm) and the wavelength. Figure 3.3(b) shows a 2D plot of the guiding wavelength as a function of the core radius (a) and the effective index.

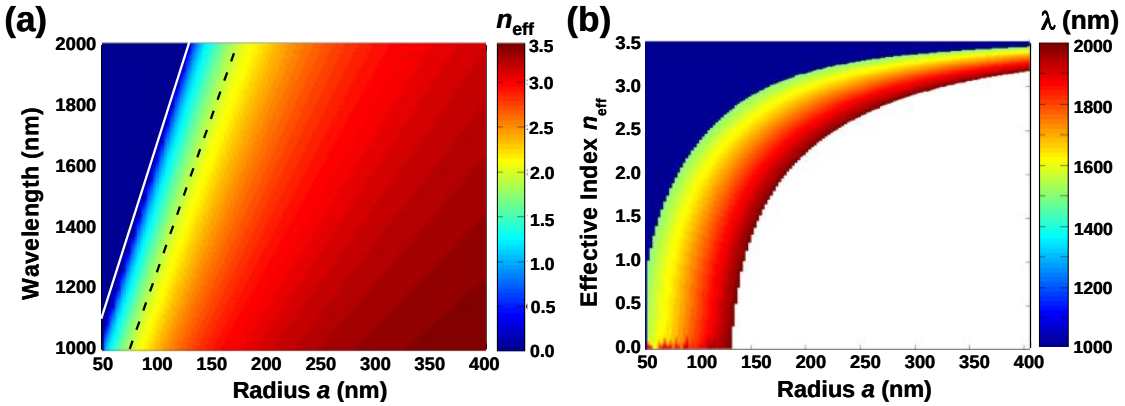

Figure 3.3: (a) The effective index as a function of core radius a and the guiding wavelength of the HE_{11} mode of a silver-coated circular waveguide with an $In_{0.53}Ga_{0.47}As$ core and a SiN_x shell (50 nm) as shown in Fig. 3.1. (b) The guiding wavelength as a function of core radius a and effective index. The wavelength is plotted only in the window of 1000-2000 nm. The white line represents the cutoff wavelength of the HE_{11} mode, on which the effective index and the propagation constant $Re(k_z)$ equals zero. To have a mode guiding inside the core region, the effective index has to be larger than the refractive index of SiN_x (~ 2.0: dashed line in (a)). This also requires the choice of cavity radius to be larger than ~ 70 nm.

3.3.2 Energy confinement factors and threshold analysis

To have an optimized design for achieving laser action, the most important issues are to reduce the loss from radiation out of the cavity and the material dissipation from dielectric materials inside the cavity or from the cavity walls, and to have a good matter-light interaction (i.e. good overlap between optical energy and active materials). The loss can be quantified by the cavity quality factor Q which is defined as

$$Q = 2\pi \frac{\text{energy stored in cavity}}{\text{power loss per optical cycle}} = \frac{\omega W}{P_{loss}} \tag{3.3}$$

where P_{loss} represents the total power loss and can be separated into loss from material (P_{mat}) and loss from radiation (P_{rad}). W is the energy stored in the cavity. As a result, the quality factor can be separated as

$$Q^{-1} = \frac{P_{loss}}{\omega W} = \frac{P_{mat} + P_{mat}}{\omega W} = Q_{mat}^{-1} + Q_{rad}^{-1} \tag{3.4}$$

in which Q_{mat} is the material quality factor and Q_{rad} is the radiation quality factor. A good feedback mirror will help the increase of Q_{rad}, but at the expense of decrease in output power. As described in Sec. 3.3.1, the material loss can be minimized by inserting the optical buffer layers in between the semiconductor and lossy metallic cavity walls.

In dealing with small lasers, especially with dispersive plasmonic materials like metals, the confinement factor associated with energy should be used to better account for the dispersive and plasmonic effects. The use of the energy confinement factor corrects the improper use of the negative power flow and negative energy resulting from negative permittivity of metals. The energy confinement factor is defined as [38]

$$\Gamma_E = \frac{\int_{V_a} d\mathbf{r} \frac{\epsilon_0}{4} \left\{ \epsilon_{g,a}(\omega) + Re\left[\epsilon_a(\omega)\right] \right\} \left|\mathbf{E}(\mathbf{r})\right|^2}{\int_V d\mathbf{r} \frac{\epsilon_0}{4} \left\{ \epsilon_g(\omega) + Re\left[\epsilon(\omega)\right] \right\} \left|\mathbf{E}(\mathbf{r})\right|^2}, \tag{3.5}$$

where $\epsilon_g(\mathbf{r},\omega)$ is the group permittivity defined as $\partial Re[\omega\epsilon(\mathbf{r},\omega)]/\partial\omega$, n_g is the active material group index and c is the speed of light in vacuum.

The threshold material gain can be formulated as [38]

$$g_{th} = \frac{\omega n_g}{c\Gamma_E Q} \tag{3.6}$$

The idea for lasing is to make Γ_E and Q as large as possible.

3.4 Fabry-Pérot Formalism and Comparison with FDTD and FEM

3.4.1 Fabry-Pérot model for plane waves

The simplest one-dimensional cavity model for laser applications consists of two mirrors and a gain medium sandwiched in between. As shown in Fig. 3.4, the cavity feedback is provided by two mirrors M_1 and M_2 with reflection coefficients r_1 and r_2, respectively. The cavity length L is defined by the distance between two mirror surfaces. A gain medium is placed uniformly in the cavity to provide optical gain when the light is bouncing back and forth inside the cavity. With carrier injection, the round-trip condition has to satisfy the equation to achieve the laser oscillation [39]:

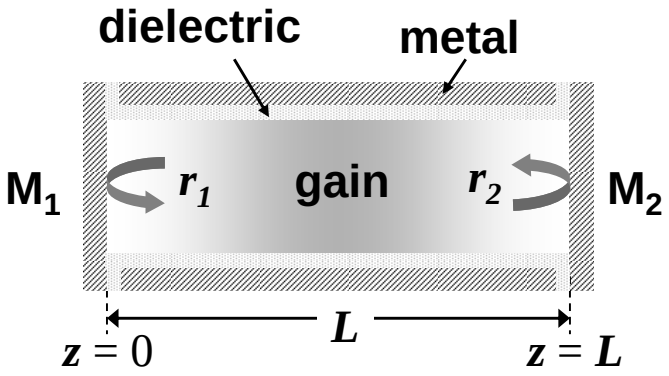

Figure 3.4: Schematics of a Fabry-Pérot cavity with a gain medium. The gain medium is sandwiched between two mirrors M_1 and M_2 with reflection coefficients r_1 and r_2, respectively. The total cavity length from M_1 to M_2 is L.

$$r_1 r_2 e^{[i2k'_z L+(g-\alpha_i)L]} = 1 \tag{3.7}$$

where k'_z is the propagation constant of the waveguide mode inside the cavity, α_i is the intrinsic loss experienced by the light propagation, and g is the gain coefficient inside the cavity. In general the reflectivities of the mirrors are complex numbers and can be expressed as $r_i = |r_i|e^{i\phi_i}$, where ϕ_i is the phase difference from the reflection. Equation (3.7) leads to

the well-known magnitude and phase conditions for lasing threshold,

$$g_{th} = \alpha_i + \frac{1}{L} ln \left(\frac{1}{|r_1||r_2|} \right) = \alpha_i + \alpha_m \tag{3.8a}$$

$$2k_z' L + \phi_1 + \phi_2 = 2m\pi. \quad (m\text{=integer}) \tag{3.8b}$$

where α_m is the mirror loss of the cavity.

3.4.2 Fabry-Pérot model for plasmonic waveguides

In real cases, especially for waveguides of transverse dimensions comparable to the wavelength, the plane wave approximation fails due to the modal dispersion. Also, the field inside the waveguide tends to spread out evanescently while propagating. In order to include the modal properties, the metal dispersion, and the effect of passivating insulator, the modal effective index of each layer in the vertical direction should be used as the input for the design. The diameter-dependent effective indices of the HE_{11} mode in a cylindrical structure with a variable GaAs core diameter, a 60 nm silicon nitride (SiN_x) insulator, and surrounding silver metal at the wavelength of 870 nm are plotted in Fig. 3.5. A significant deviation from its bulk value of GaAs resulting from the size reduction needs be taken into consideration, especially when the device size is comparable to the wavelength.

Figure 3.6 shows the typical cross-section of a Fabry-Pérot plasmonic nanolaser; the semiconductor core is surrounded by a thin insulator and an outer metal coverage which serves as a cavity wall. To properly include the modal properties, the effective index ($\bar{n}_{eff}$) corresponding to the waveguide mode should be used instead of material index [37].

The effective index can be solved from the Maxwell's equation,

$$\left[\nabla_t^2 + n(\boldsymbol{\rho})^2 k_0^2\right] \begin{pmatrix} E_z \\ H_z \end{pmatrix} = k_z^2 \begin{pmatrix} E_z \\ H_z \end{pmatrix} \tag{3.9}$$

where ∇_t is the transverse Laplace operator, $n(\boldsymbol{\rho})$ is the refractive index profile at transverse

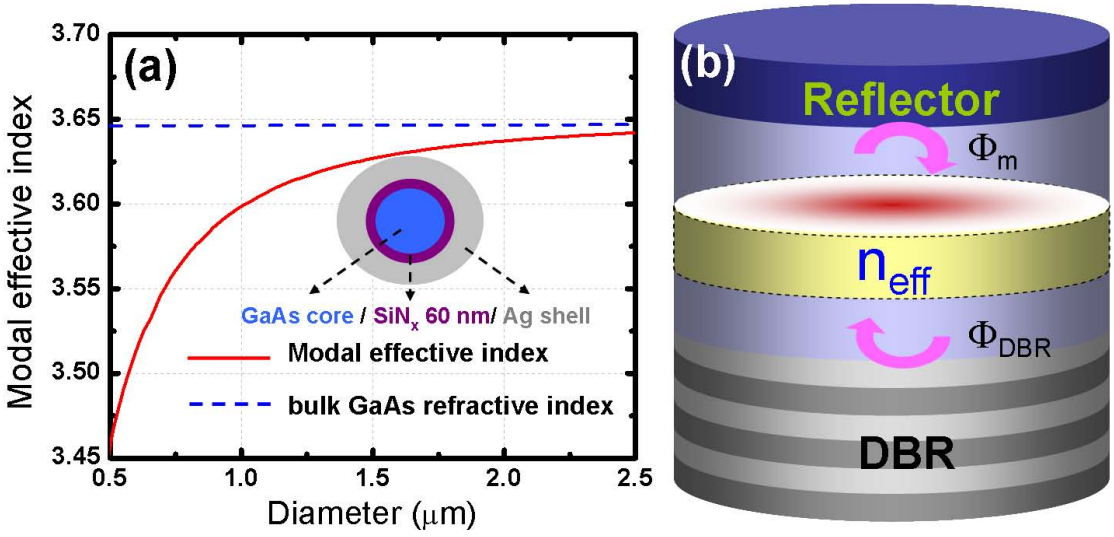

Figure 3.5: (a) The modal effective indices (solid curve) of a core-shell structure (GaAs core/SiN_x(60 nm)/Ag shell) as a function of the core diameter. The deviation from the GaAs bulk value (dashed) is significant when the core diameter is small. (b) A schematic of our designed structure with the metal effect included via the modal effective index (n_{eff}); m and DBR are the corresponding reflection phase shifts from the metal and the DBR reflector, respectively.

position $\boldsymbol{\rho}$, k_0 is the free space wavenumber ($k_0 = 2\pi/\lambda$, λ = free space wavelength), and E_z and H_z are the z component of the electric and magnetic fields, respectively. The transverse electric and magnetic fields are then expressible in terms of E_z and H_z components. The complex propagation constant k_z is obtained by solving the boundary value problem. In general, the complex effective index $\bar{n}_{eff}$ for a metal-clad passive waveguide before carrier injection, after solving k_z, is obtained as:

$$k_z = k_0 \bar{n}_{eff} \tag{3.10a}$$

$$\bar{n}_{eff} = n_{eff} + i\frac{\alpha_i}{2k_0} \tag{3.10b}$$

where n_{eff} is the real part of the effective index and α_i is the corresponding intrinsic loss of that waveguide section.

For a waveguide with a multilayer structure along the propagation direction (i.e. z direction), the phase condition in Eq. (3.8b) should be modified to

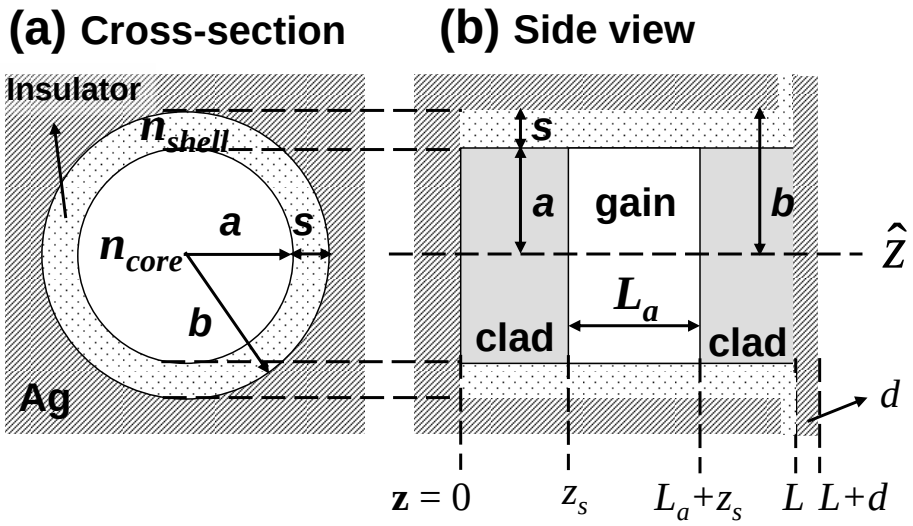

Figure 3.6: (a) Cross-section and (b) side view of a core-shell metallic waveguide. The core region is filled with a semiconductor material with refractive index n_{core} and the shell is an insulator layer with refractive index n_{shell}. The core radius is a and insulator thickness is s. In (b), the cavity length is L with a active region placed in $z_s < z < z_s + L_a$. The output mirror metal thickness is d.

$$2\left(\sum_j k_0 n_{eff,j} L_j\right) + \phi_1 + \phi_2 = 2m\pi, \tag{3.11}$$

where j is the layer index. In semiconductor lasers, the gain material occupies only a portion of the waveguide. The round-trip optical travel between two mirrors only experiences the optical gain during the pass through the gain material. To relate the gain coefficient in the FP model in Eq. (3.7) to the modal gain (g_M) in partially-gain-filled waveguide case, a longitudinal confinement factor (Γ_z) has to be introduced,

$$\Gamma_z = \frac{\int_{active} |\Phi(z)|^2 dz}{\int_{cavity} |\Phi(z)|^2 dz} \tag{3.12}$$

in which $\Phi(z)$ is the amplitude function of the dominant electric field component as a function of the propagation direction. For a cavity fully filled with gain material, $\Gamma_z = 1$. To relate the modal gain (g_M) to material gain (g_m) by considering the occupation of gain medium in the transverse direction, a confinement factor (Γ_{wg}) based on the overlap between optical

field and gain medium should be included. The gain coefficient g can be further written as

$$g = \Gamma_z g_M = \Gamma_z \Gamma_{wg} g_m. \tag{3.13}$$

The waveguide confinement factor (Γ_{wg}) which accounts for the transverse confinement is defined as [38]

$$\Gamma_{wg} \equiv \frac{\left(\frac{n_a}{2\eta_0}\right) \int_{active} d\boldsymbol{\rho} |\mathbf{E}(\boldsymbol{\rho})|^2}{\int_A d\boldsymbol{\rho} Re\left[\frac{1}{2}\mathbf{E}(\boldsymbol{\rho}) \times \mathbf{H}^*(\boldsymbol{\rho})\right] \cdot \hat{z}} \tag{3.14}$$

in which $\mathbf{E}(\boldsymbol{\rho})$ and $\mathbf{H}(\boldsymbol{\rho})$ are the electric and magnetic field at the transverse position $\boldsymbol{\rho}$, n_a is the refractive index of the active region, and $\eta_0 = \sqrt{\mu_0/\eta_0}$ is the characteristic impedance, μ_0 is the permeability and ϵ_0 is the permittivity of the free space. The integration domain A is the entire transverse plane and $d\boldsymbol{\rho} = \rho d\rho d\phi$.

By using Eq. (3.8a), (3.14), and (3.16), the threshold material gain ($g_{m,th}$) for a mutisectional Fabry-P*é*rot cavity is defined as

$$g_{m,th} = \frac{1}{\Gamma_z \Gamma_{wg}} \left[\langle \alpha_i \rangle + \frac{1}{L} ln\left(\frac{1}{|r_1||r_2|}\right)\right] \tag{3.15}$$

where

$$\langle \alpha_i \rangle \equiv \frac{\sum_j \alpha_{i,j} L_j}{\sum_j L_j} = \frac{\sum_j \alpha_{i,j} L_j}{L} \tag{3.16}$$

which accounts for the intrinsic loss $\alpha_{i,j}$ of each layer and $L = \sum_j L_j$ is the total length.

3.4.3 Quality factor of Fabry-P*é*rot nanocavities

The photon life time (τ_p) associated with the Fabry-P*é*rot cavity can be derived as [37]

$$\frac{1}{\tau_p} \equiv \frac{\omega}{Q} = \frac{\omega}{Q_{abs}} + \frac{\omega}{Q_{rad}} \tag{3.17}$$

where ω is the angular frequency, and Q is the total cavity quality factor. Q_{abs} is the quality factor associated with the intrinsic modal absorption loss,

$$\frac{\omega}{Q_{abs}} = \langle \upsilon_g \alpha_i \rangle = \frac{1}{L} \sum_j \upsilon_{g,j} \alpha_{i,j} \tag{3.18}$$

Q_{rad} is the quality factor associated with the radiation mirror loss,

$$\frac{\omega}{Q_{rad}} = \frac{\alpha_m}{\upsilon_g^{-1}} = \frac{\alpha_m L}{\sum_j \upsilon_{g,j}^{-1} L_j} \tag{3.19}$$

and $\upsilon_{g,j}$ is the group velocity in the layer section j,

$$\upsilon_{g,j} \cong \left[\frac{\partial k_{z,j}(\omega)}{\partial \omega} \right]^{-1} \tag{3.20}$$

3.4.4 Longitudinal confinement factor

With the modal and material dispersion included in the effective indices, the cavity can now be characterized using the 1-D Fabry-Pérot model. To properly include the mirror effect from imperfect reflectivity and phase, special care has to be made to have an accurate design [39]. Besides the round-trip phase condition in 3.11, due to the short cavity length, the reflection phase from imperfect mirrors, especially real metals, would result in a significant deviation of the longitudinal confinement from a perfect electric conductor (PEC) mirror model, which has a transverse electric field node at the mirror boundaries. At optical frequency, electrons in metals react with the optical field and form a plasma inside the metal. Due to the ohmic loss in the metal, the oscillation of plasma damps out gradually and results in a complex permittivity. Unlike the PEC case, reflectors composed of real metals will have non-zero electric fields at the mirror boundary.

Here we consider only the TE-like modes, which have dominant electric field in the transverse directions and will experience less metallic loss from the mirrors. For example, considering the fundamental HE_{11} mode, which is similar to TE_{11} mode with dominant electric

fields in the transverse directions, the standing wave profile can be approximately written as

$$\Phi(z) = \Phi_0 \begin{cases} \sin(n_{eff,clad}k_0 z + \frac{\Delta\phi_1}{2}), & (z \le z_s) \\ \sin\left[n_{eff,a}k_0(z - z_s) + n_{eff,clad}k_0 z_s + \frac{\Delta\phi_1}{2}\right], & (z_s < z \le z_s + L_a) \\ \sin\left[n_{eff,clad}k_0(z - L_a) + n_{eff,a}k_0 L_a + \frac{\Delta\phi_1}{2}\right]. & (z_s + L_a < z \le L) \end{cases} , \quad (3.21)$$

where $\Delta\phi_i$ comes from the reflection $r_i = |r_i| \exp(-i\pi + i\Delta\phi_i)$ and is the phase difference between PEC and the real metal, $n_{eff,clad}$ and $n_{eff,a}$ represent the real part of the effective index of the cladding and the gain region, and Φ_0 is a constant. The phase condition is satisfied by

$$2k_0 n_{eff,clad}(L - L_a) + 2k_0 n_{eff,a} L_a + \Delta\phi_1 + \Delta\phi_2 = 2m\pi. \quad (3.22)$$

The reflection coefficients from metal reflectors are usually close to -π and the standing wave patterns are similar to the node type (minimum at the boundary).

3.4.5 Numerical example: metal-cavity surface-emitting nanolasers

Considering a waveguide such as that shown in Fig. 3.6, the simulated structure consists of $In_{0.53}Ga_{0.47}As$ gain material of length 255 nm with p-type and n-type InP cladding layers, both 270 nm. The semiconductor radius is denoted as a and the insulator SiN_x (n_{shell} = 2.0) thickness s is kept at 50 nm. The waveguide is completely surrounded by silver thicker than the penetration depth except for the output mirror. The effect of output mirror silver thickness d will be discussed later. The refractive indices of the semiconductors are taken from experiment data [36]. The dispersive permittivity of silver is included by the Drude model with parameters from the literature [35]. To evaluate the accuracy of the FP model, a full structure FDTD calculation was performed for comparison. Figure 3.7 shows the comparison of both methods. The resonance wavelength in Fig. 3.7(a) shows an excellent agreement between FP model (Line) and FDTD (Symbol). The term p represents the longitudinal standing wave numbers between two mirrors. For design with p = 3, the

resonance wavelength falls into the gain spectrum of $In_{0.53}Ga_{0.47}As$ [40]. In Fig. 3.7(b), the quality factors calculated by both methods agree well with each other, and they increase with the longitudinal order p, or, equivalently, the effective wavelength inside the waveguide becomes shorter. The quality factor calculated by the FP method is slightly lower than that of the full structure FDTD calculation. The small discrepancy comes from the reflectivity estimation from the Fresnel formula which usually underestimates the reflectivity, especially when the waveguide cross-section is comparable to the wavelength [37].

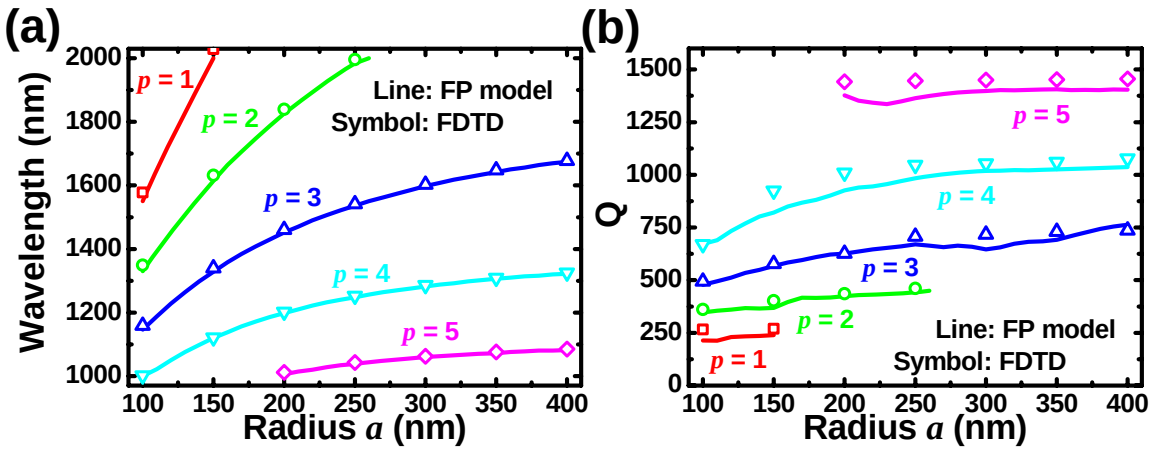

Figure 3.7: Comparison of the Fabry-Pérot model (lines) with full structure FDTD simulation (symbols) of a cavity with an active length $L_a = 255$ nm and InP cladding layers of 270 nm. (a) Resonance wavelengths as a function of core radius a. The term p represents number of the longitudinal standing waves inside the cavity. The excellent agreement shows the validity of the FP model. (b) Quality factors as a function of the core radius a.

CHAPTER 4

METAL-CAVITY SURFACE-EMITTING MICROLASERS WITH DISTRIBUTED BRAGG MIRRORS

In this chapter, we present the realization of microlasers with metal as the cavity wall and DBRs functioning as part of the reflectors. The device configuration, wafer design, and fabrication techniques are discussed in detail. The experimental data for devices aimed at 980 nm and 850 nm are shown with analyses from FDTD. Improvements such as the beam profile, thermal management, and possible size reduction schemes are included at the end of this chapter.

4.1 Configuration and Device Design

Conceptually, the design originates from the proper termination (i.e. feedback mirror) of the optical fiber mode supported by the metallic waveguide. Figure 4.1(a) shows the proposed structure with top-emitting configuration. The feedback structure with metals truncates the outstretched long optical tail and results in a more compact size and more efficient loss reduction. The waveguiding effect and material dispersions will be modeled and properly incorporated into the effective index by solving the Maxwell's equations associated with the multilayered cylindrical waveguide profile. The cavity structure can thus be treated as a Fabry-Pérot cavity with specific reflectors at the two ends. Figure 4.1(b) shows four feedback schemes formed of distributed Bragg reflectors (DBR) and metals: (i) metal-metal, (ii) top DBR-bottom metal, (iii) top metal-bottom DBR, and (iv) DBR-DBR reflectors. The emission reflector should be designed with enough transmission (i.e. thin metal or only few pairs of DBR) to allow a reasonable power output. The reflection coefficients from bottom

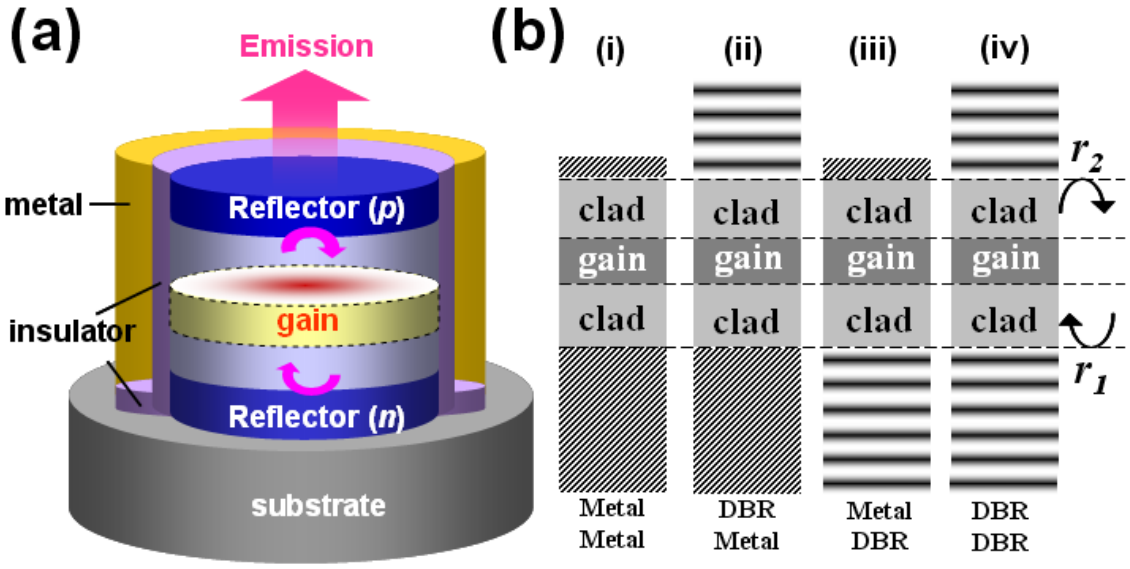

Figure 4.1: (a) Proposed structure of metal-cavity surface-emitting nanolasers. The cavity is formed by terminating both ends of the metallic waveguide with reflectors. The insulator in between the semiconductor and the metal ensures the blocking of current flow as well as functions as an optical buffer. The current-injection scheme allows top emission and substrate-free properties. (b)1-D configurations with different reflectors. (i) metal-metal, (ii) top DBR-bottom metal, (iii) top metal-bottom DBR, and (iv) DBR-DBR reflectors. r_1 and r_2 are the reflection coefficients of the bottom and top mirrors, respectively.

and top mirrors are r_1 and r_2. In general, they are complex numbers due to the absorption inside the mirrors. To properly include the mirror effect from imperfect reflectivity and phase, special care has to be taken to have an accurate design [39]. According to different boundary conditions at the semiconductor/mirror interface, there are four types of standing wave patterns inside the cavity (bottom-top boundaries): node-node, node-peak, peak-node, and peak-peak. The phases of the reflection coefficients from metal reflectors are usually close to -π and the standing wave patterns are similar to the node type (minimum at the boundary). As for DBR, the reflection can be either peak type (maximum at the boundary) or node type depending on the arrangement of the alternative high and low indices inside the DBR [39]. Table 4.1 summarizes different reflection phase differences from PEC of four types of cavities in Fig. 4.1 (b).

Table 4.1: Reflection phase difference from the PEC case for metallic and DBR mirrors

Type (bottom-top)	(i) Metal-Metal	(ii) Metal-DBR	(iii) DBR-Metal	(iv) DBR-DBR
Node-Node	$0 < \Delta\phi_1 < \pi/2$ $0 < \Delta\phi_2 < \pi/2$	$0 < \Delta\phi_1 < \pi/2$ $\Delta\phi_2 = 0$	$\Delta\phi_1 = 0$ $0 < \Delta\phi_2 < \pi/2$	$\Delta\phi_1 = 0$ $\Delta\phi_2 = 0$
Node-Peak	*	$0 < \Delta\phi_1 < \pi/2$ $\Delta\phi_2 = \pi$	*	$\Delta\phi_1 = 0$ $\Delta\phi_2 = \pi$
Peak-Node	*	*	$\Delta\phi_1 = 0$ $0 < \Delta\phi_2 = \pi/2$	$\Delta\phi_1 = \pi$ $\Delta\phi_2 = 0$
Peak-Peak	*	*	*	$\Delta\phi_1 = \pi$ $\Delta\phi_2 = \pi$

4.1.1 DBR and metal hybrid mirror

The reflectivity from the hybrid mirror with the insertion of a few pairs of DBR is increased significantly. As shown in Fig. 4.2(a), with the silver backup, the reflectivity of the hybrid mirror with only 4 pairs of $Al_{0.15}Ga_{0.85}As$ /$Al_{0.90}Ga_{0.10}As$ exceeds 99% while a pure DBR requires more than 15 pairs to achieve 99%. Another benefit from a hybrid mirror is the expansion of high reflection window. As shown in Fig. 4.2(b), for mirrors over 99.97%

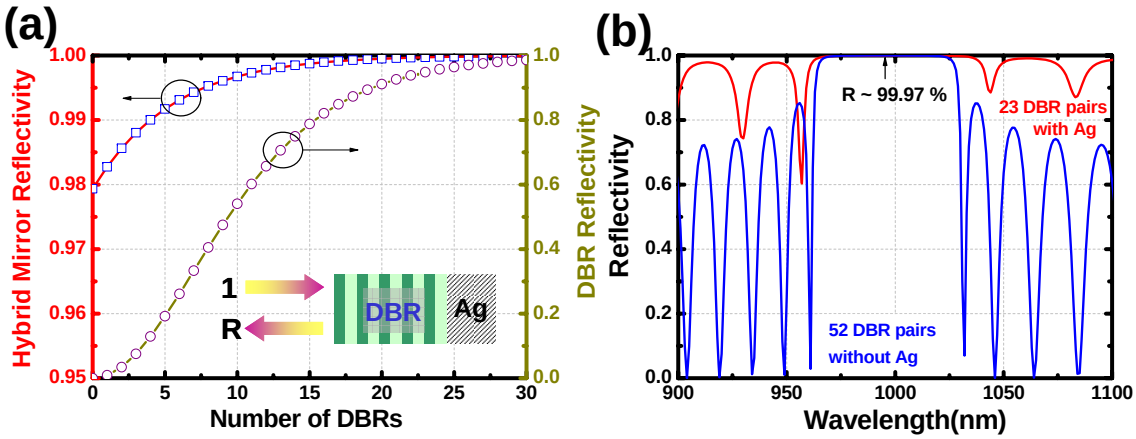

Figure 4.2: (a) Reflectivities of a hybrid mirror, which consists of a silver (Ag) region and an $Al_{0.15}Ga_{0.85}As/Al_{0.90}Ga_{0.10}As$ DBR with different number of pairs and its counterpart without silver. A large increase in reflectivity (or reduction in the required number of DBR pairs) is observed due to the high reflectivity of metal. (b) Reflection spectra of a hybrid mirror with 23 DBR pairs coated by silver and a 52-DBR-pair mirror without coating with R 99.97 %. The high reflection window for the hybrid mirror is 25 % wider than that of a DBR only mirror.

reflectivity, the high reflection window for the hybrid mirror (23 DBR pairs + Ag) can be 25% wider compared to that of a mirror with only DBR (52 DBR pairs). This allows a size reduction of 50% without downgrading the reflectivity. This expansion of high reflection window is crucial and allows for further size reduction in which the resonance is extremely sensitive to the geometry, i.e., the modal dispersion becomes large when the size approaches the wavelength.

4.2 Process and Fabrication Technology

Figure 4.3 depicts the main process steps of metal-cavity laser structures: *i*) The epi-structures are in general grown by industry standard metal-organic vapor-phase epitaxy (MOVPE), metal-organic chemical-vapor epitaxy (MOCVD), or molecular beam epitaxy

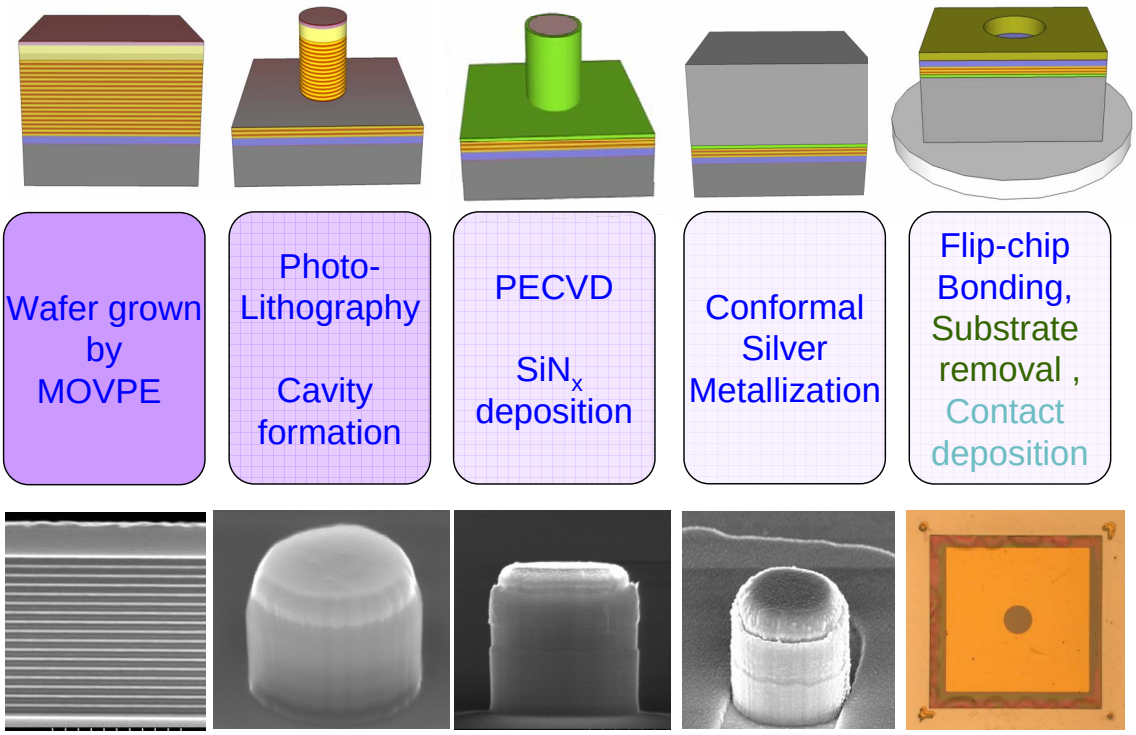

Figure 4.3: The process flow for metal-cavity devices. Scanning electron micrographs and a optical microscope image of the final step are shown below. The process steps are *i*) epi-wafer, *ii*) cavity formation by photolithograhpy, *iii*) SiNx passivation layer coating and top removal for contacts, *iv*) conformal metallization, *v*) bonding, substrate removal, and contact deposition.

(MBE). *ii*) An etching mask of silicon nitride (SiN_x) is deposited by plasma-enhanced chemical vapor deposition (PECVD) and patterned by optical lithography. A freon reactive ion etcher (RIE) is used to transfer the circular patterns to SiN_x which serves as a hard mask for the following dry etching. A deep etch on the epiwafer by an inductively-coupled plasma reactive ion etcher (ICP-RIE) defines the semiconductor cavity. *iii*) A thin SiN_x layer is conformally deposited after the removal of the top silicon-nitride mask. Planarization by resists and developers helps the exposure of the top of the post covered by silicon nitride. The exposed SiN_x is then removed to facilitate the following contact formation. *iv*) Metal evaporation coats the device with 200 nm silver conformally on the surface. *v*) The sample is flip-bonded to a gold-coated silicon receptor wafer with silver epoxy. The substrate removal is followed by the contacts formation for current injection.

4.3 Results on 980 nm Metal-Cavity Surface-Emitting Microlasers

In this design, we use a hybrid mirror with 23 DBR pairs and silver as the bottom mirror, as shown in Fig. 4.4. Figure 4.4(b) shows the cavity quality factor (Q), energy confinement factor (Γ_E), and the resonance wavelength as a function of the number of DBR pairs. The simulation shows that the addition of a few DBR pairs in between the top silver mirror and the active materials greatly increases the cavity quality factor due to the increased reflectivity of the hybrid mirror. Even though the quality factor changes a lot, the resonance wavelength does not shift much due to the insertion of quarter-wavelength DBRs (i.e. additional 2π phase shift). As shown in Fig. 4.4(b), due to the truncation of optical fields by metal, reducing the pairs of DBRs results in an increase of the energy confinement factor and, thus, is another benefit of the hybrid mirror. A significant reduction in threshold gain can be made by increasing either Γ_E or Q. For example, Fig. 4.4(a) shows the schematic diagram of the device structure with a 23-DBR-pair coated by silver as a hybrid mirror. The structure has an energy confinement factor of about 0.0214 and a Q of 1,534. The threshold gain is

estimated to be 7,041 cm^{-1}. Figure 4.4(c) shows the standing wave pattern (norm of electric field: $|\mathbf{E}|$) inside the micropost with a cavity height of 4.0 μm and 1.0 μm in radius.

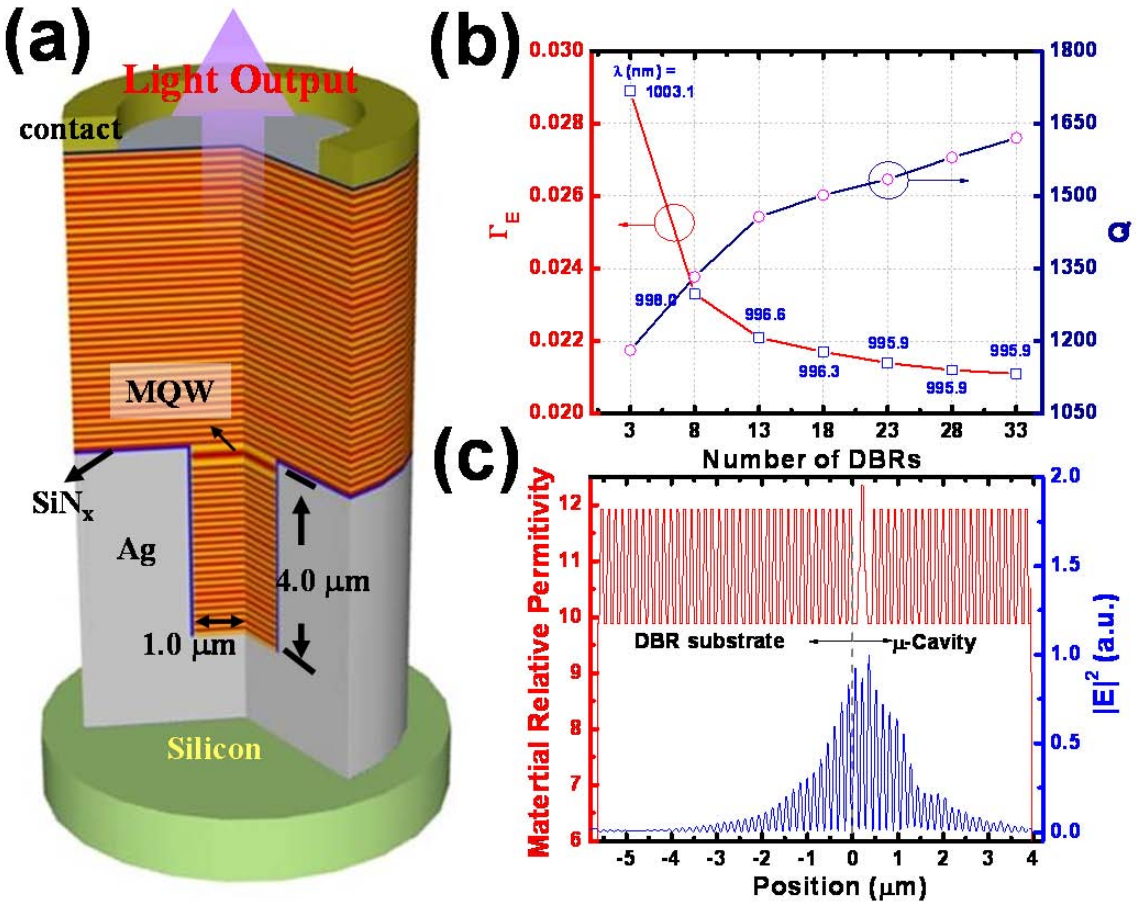

Figure 4.4: (a) Schematic of our new device, which is flip-chip bonded to a silicon substrate. The bottom mirror consists of a 23-pair DBR and silver. The optical cavity is formed between the bottom hybrid DBR and the top DBR. The cavity has a radius of 1.0 m and a height of 4.0 μm. (b) The energy confinement factor (Γ_E) and cavity quality factor (Q) as a function of the number of DBR pairs. Cavity Q increases due to the increase of reflectivity. The insertion of DBR elongates the optical field extension and thus gradually reduces the energy confinement factor. (c) The electric field distribution ($|\mathbf{E}|^2$) inside the cavity and DBR substrate.

4.3.1 Laser performance

The *epi*-structure used in the device fabrication was grown by metal-organic vapor-phase epitaxy (MOVPE). The micropost was defined by an inductively-coupled plasma reactive

ion etcher (ICP-RIE). Silver metal was coated conformally to serve as a cavity wall and a p-type contact. In between the semiconductor and metal, a thin silicon nitride layer was deposited to block the current flow. The defined micropost has a radius of ~ 1.0 μm and a height of ~ 4.0 μm (just through the active region), corresponding to a volume of 12.6 λ_0^3. After the transfer of devices to a silicon substrate, the original GaAs substrate was removed by wet etching. Due to the high etching selectivity between the GaAs and AlGaAs layers, the etching stops right at the exposure of DBR layers. An n-contact was then formed on top of the exposed DBR as shown in Fig. 4.4(a). The fabricated device was tested by a DC current source and maintained at 300 K with a thermoelectric cooler. The light output power versus current (L-I) and the differential efficiency curves are shown in Fig. 4.5(a). A clear turn-on in the L-I curve represents the onset of stimulated emission. From the

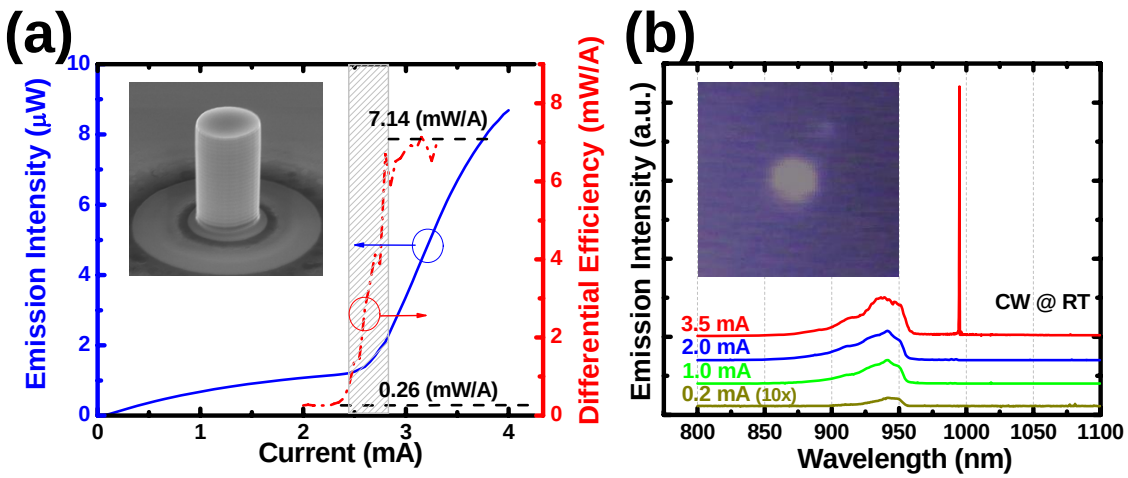

Figure 4.5: (a) The light output power vs. the injection current (L-I), and differential efficiency of the fabricated device. A transition region (gray) from 2.45 mA to 2.80 mA can be identified from differential efficiency. (Inset: a scanning electron micrograph of a 2.0-μm diameter device before metallization.) (b) The corresponding current-dependent spectra. A broad spontaneous emission spectrum was observed due to the transmission window of DBR. The lasing peak at 995 nm appears when the injection current exceeds the threshold. (Inset: camera image of the device under operation.)

differential efficiency plot, a gray transition region in between 2.45 mA and 2.80 mA depicts the transition from spontaneous emission to laser action. Along with the transition, the efficiency switches from a value of 0.26 mW/A in the spontaneous emission region to 7.14

mW/A in the stimulated emission region with an on/off ratio of about 27. The saturation is attributed to the heating and/or detuning of cavity with gain spectra at room temperature with continuous-wave operation. As a result of metal loss at optical frequency, the intrinsic loss is dominating the photon loss and resulting a low quantum efficiency. Moreover, the output coupling through the DBR emission window also limits the light extraction from the cavity. A further improvement in the transmission optimization will increase the power extraction and quantum efficiency. The inset in Fig. 4.5(a) shows a scanning electron micrograph of the device before silver metallization.

4.3.2 FDTD analysis and far field images

An important feature of the designed device is its omni-directional emission pattern due to the cylindrical symmetry and HE_{11} modal properties. A simulation of the full structure using the FDTD method was performed showing both the near-field and far-field patterns of the designed laser. Figure 4.6(a) shows the transverse electric field distribution as the wave propagates. A field distribution (magnitude $|\mathbf{E}|^2$ of the HE_{11} mode) at the cross-section of the active region is plotted in Fig. 4.6(b). Unlike the other nanolasers with squeezed dimension or notches along a certain direction due to strong compression of non-uniform optical mode, the circular design using HE_{11} mode focuses the optical mode toward the normal direction. As shown in Fig. 4.6(c), the normalized power radiation pattern (in the basis of $\exp(\pm im\phi)$) shows a single lobe with a beam width of 110^o. Although it is slightly larger due to the small dimension of the micropost output aperture, unlike other metal-cavity lasers with a rectangle slot output aperture, our laser preserves the circular light output and has no nulls in its radiation pattern. Moreover, the long propagation through the DBR substrate also expands the beam width; a clear field spread-out can be observed due to the aperture diffraction effect when exiting the micropost.

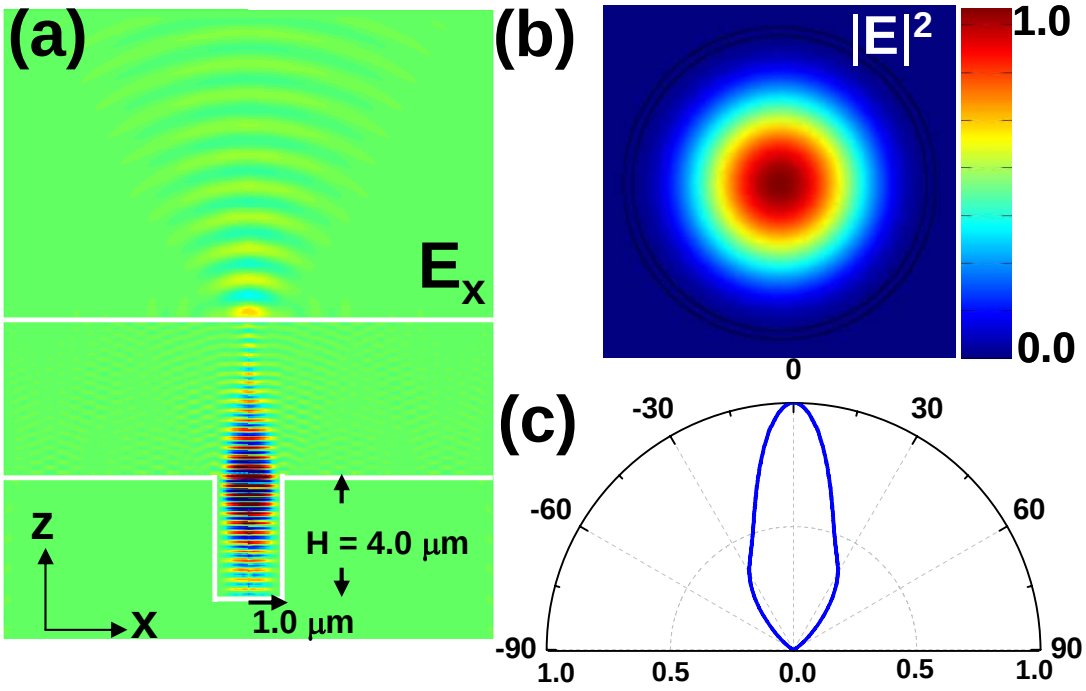

Figure 4.6: (a) The near-field and far-field pattern of our designed structure with 23-pair DBR simulated by the FDTD method. (b) The electric field squared distribution $|\mathbf{E}|^2$ of the cross section at in the active region. The circular geometry supports the fundamental HE_{11} mode which preserves the circular output. (c) A far-field radiation power pattern. A single lobe with a span of $\tilde{1}10^o$ comes from the output of the circular microcavity.

4.4 Results on 850 nm Metal-Cavity Surface-Emitting Microlasers

Figure 4.7(a) shows the schematics of our fabricated device. The devices are fabricated using a metal-organic chemical vapor deposition (MOCVD) grown wafer with an n-type Si-doped GaAs substrate. In order to have a better overlap with optical fields inside the cavity, the active region consists of 3 pairs of GaAs/$Al_{0.3}Ga_{0.7}As$ (6 nm/8 nm) quantum wells positioned at the peak of the $\lambda/2$ cavity. The 34-pair (n-type) and 22-pair (p-type) DBR consisting of alternating $Al_{0.12}Ga_{0.88}As/Al_{0.9}Ga_{0.1}As$ quarter-wavelength layers are grown before and after the growth of the active region. The high selectivity of $Al_{0.9}Ga_{0.1}As$ over GaAs makes it an excellent etch-stop layer for substrate removal hereafter. The growth of the epi-layers is ended with a heavily doped p^+ phase-matching $Al_{0.12}Ga_{0.88}As$ layer (doping $1 \times 10^{19} cm^{-3}$)

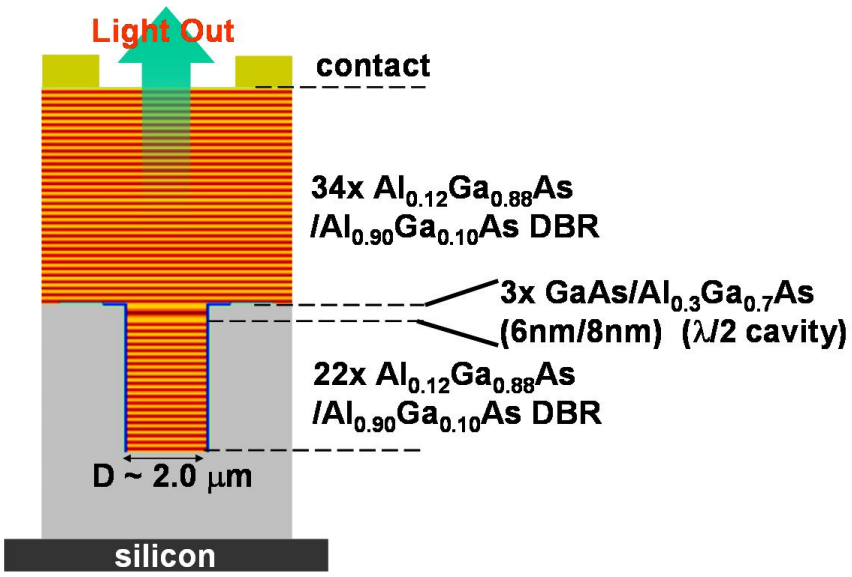

Figure 4.7: Schematic diagram of the device flip-chip bonded to silicon. Multiple quantum wells are sandwiched between silver and hybrid DBR/metal reflector. The whole device is surrounded by silicon nitride and silver to form an optical cavity. The GaAs substrate below the DBR has been removed. The physical size of the device is 2.0 μm in diameter and 3.5 μm in height. The micropillar etching depth is controlled just through the active material. The device is flip-chip bonded to a silicon substrate which in turn supports the contact and serves as a heatsink.

and a thin contact p^+ GaAs layer ($1 \times 10^{19}\text{cm}^{-3}$) for lowering the contact resistance. In order to match the round-trip phase condition, the thickness of each layer is determined by the transfer matrix method with the metal effect included in effective modal indices. A 1.0 μm radius circular mask is defined by photolithography on a chemical-vapor-deposited silicon nitride layer on the wafer. An inductively coupled plasma/reactive ion etcher with $SiCl_4$/Ar mixture is used to form a cylinder 3.5 μm in height. A thick silver metal is coformally coated after the encapsulation of a thin silicon nitride. Before the substrate removal, the devices are flipped and transferred to a gold-coated silicon substrate. The bottom contact composed of AuGe/Ni/Au is deposited on the n-type etch-stop layer by e-beam metallization. Subsequent curing in N_2 ambient environment at 150 ^{o}C for 30 minutes is done to strengthen the bonding and the contact.

4.4.1 Laser performance

The measurements were performed at 300 K with a thermoelectrically-cooled copper heat sink on which the devices were mounted. A DC current source with a 10 μA precision was used to drive these devices. The emission was collected by an objective lens (50X, 0.60 NA) and dispersed by a 1.25 m monocromator with a liquid-nitrogen-cooled germanium detector. The current versus voltage (I-V) and light output power versus current (L-I) curves shown in Fig. 4.8(a) indicate a turn-on threshold at around 1.66 mA, beyond which a lasing peak emerges at 868 nm with a gradual red-shift as the driving current increases [Fig. 4.8(b)]. We also notice that a second mode started to lase at a wavelength 0.4 nm shorter than

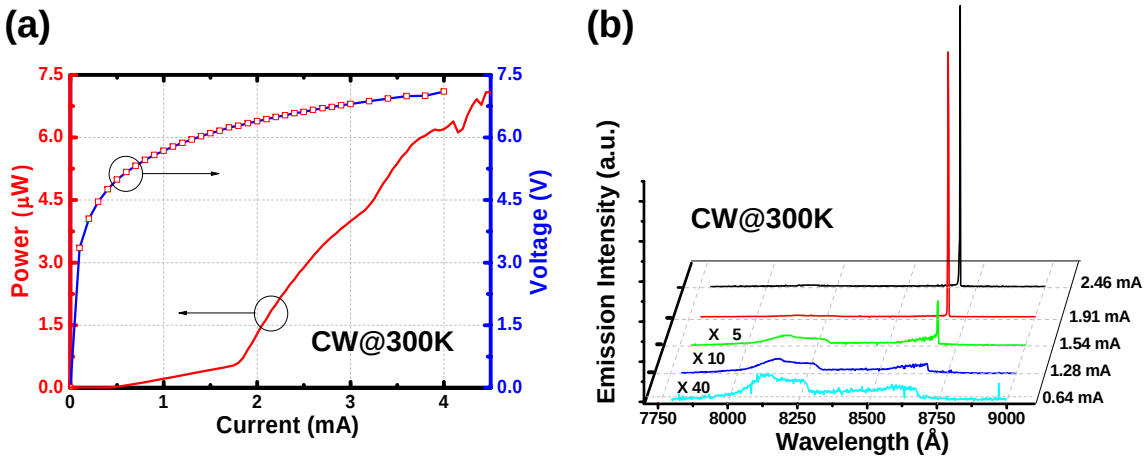

Figure 4.8: (a) Current vs. voltage (I-V) and light output power vs. current (L-I) plots measured at room temperature (300 K) under DC current injection. The L-I curve shows a threshold of 1.66 mA. (b) The corresponding current-dependent spectra. Below threshold, a broad spontaneous emission spectrum was observed. The lasing peak around 868 nm appeared when the injection current exceeded the threshold value.

the first lasing peak. This additional mode comes from the splitting of HE_{11} mode into two orthogonal and quasi-linearly-polarized modes (namely, $\exp(\pm\phi)$) due to a small imperfection or asymmetry of the waveguide structure. As shown in Fig. 4.8(a), the kink in the L-I curve around 3.2 mA corresponds to the onset of the second peak. To identify the origin of the second peak, we show the polarization-resolved L-I curves of individual modes in Fig. 4.9(a). Each curve shows a clear threshold behavior. From Fig. 4.9(b), the onset of the second lasing

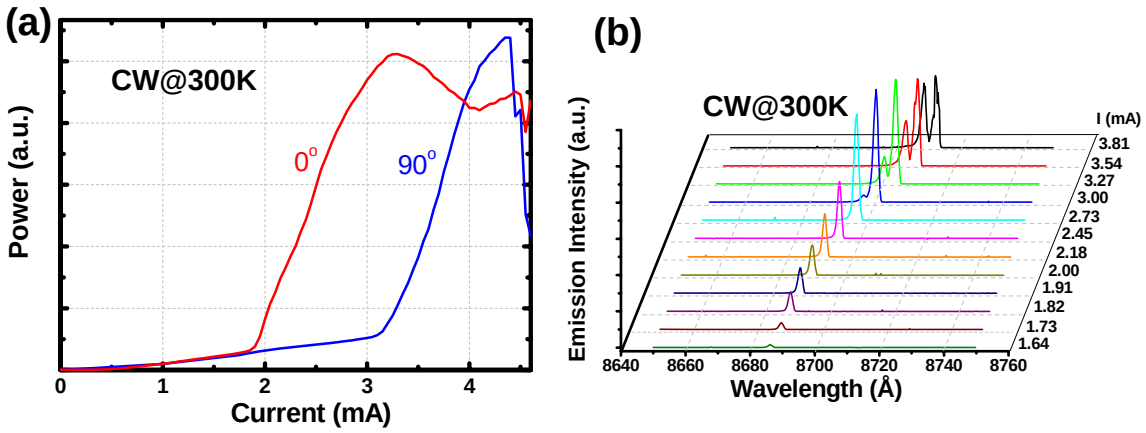

Figure 4.9: (a) The polarization-resolved L-I curves distinguish two modes due to the splitting of two degenerate HE_{11} modes. A clear onset of the second mode around 3.30 mA was observed. (b) The spectral evolution of the two lasing peaks with increasing current. The second peak emerged above its threshold. A clear red shift due to heat was observed when the current increased. All data were taken with continuous-wave operation at 300 K.

peak reflects the kink in the L-I curve shown in Fig. 4.8(a). Near threshold, the linewidth of the lasing peak was estimated to be around 1.5 nm (@ 1.45 mA), which gave a Q factor of 580. The narrowest setup-resolvable linewidth is 67 pm at 2.73 mA, obtained just below the threshold of the second peak. The threshold current density was estimated to be 52.8 kA/cm2. With the lossy metal coating and high radiation loss from the moderate reflectivity of the silver mirror, the threshold current density is high compared to the data reported in the literature.

4.4.2 Thermal impedance

Due to the short cavities, VCSELs usually suffer from severe thermal effects, which in turn result in the saturation of optical output power and modulation bandwidth [41]. An effective heat sink becomes a critical issue to the performance of the lasers. Although metals were used as reflectors for large VCSELs since 1979, the advantages of metal for heat removal for small devices are not obvious yet. Early works on VCSELs show an inevitable heat transport problem when the size becomes smaller than few microns [26]. Recent work on electroplated

gold and copper as heatsinks has shown a significantly reduced thermal impedance of VCSELs down to 1.0 ^{o}C/mW for devices with 9 μm apertures [42]. Moreover, previous work [43] showed the reduction of VCSEL thermal impedance by flip-bonding to integrated circuits. Further reduction of the thermal impedance of VCSELs will be limited by the series resistance of the top and bottom distributed Bragg reflectors (DBRs), especially when the device size shrinks. On the other hand, the insulator surrounding the device can also impede the efficient heat conduction to the heatsink. The supporting material near the contact for small devices such as polymers can also increase the thermal impedance [41, 42]. Metal, due to its excellent thermal and electrical conductivities, is commonly used as the electrical contact and heatsink. Also, researches on different active materials, like QD, with novel cavity structures have shown good thermal stability under high power operation [44]. Although metal-cavity lasers have been reported recently [15, 19, 22, 32], the thermal properties have not yet been analyzed.

To investigate the thermal impedance of the fabricated metal-cavity microlasers, the devices are mounted on a thermoelectric-controlled copper heatsink to hold a constant substrate temperature. The emission light is collected by a microscope system with an objective lens with a 0.60 numerical aperture and 8 mm clear aperture. A monochromator of 1.25 m focus length is used to disperse the collected emission. The dispersed light is detected by a germanium detector kept at the liquid nitrogen temperature. Figure 4.10 shows the light output - current - voltage (L-I-V) curves of a 1.0 μm radius and 3.5 μm height device under DC current injection at 20 ^{o}C. The fabricated laser has a threshold of 4.1 mA and a series resistance of 300Ω after the diode-like turn-on. The high value of series resistance results from the small diameter of the device. Figure 4.11(a) shows temperature-dependent L-I curves of Device A and from which the threshold currents and differential efficiency are extracted and plotted in Fig. 4.10(b). Despite its small aperture, due to the efficient heat removal benefited from metal, the threshold current changes only 10% in the range of 15-80 ^{o}C and the differential efficiency remains almost constant up to 50 ^{o}C. The thermal impedance is

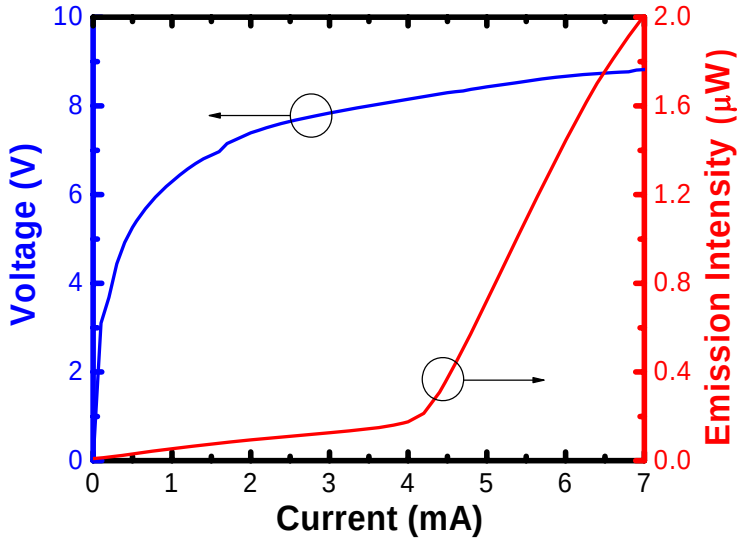

Figure 4.10: The L-I-V curve under DC current injection at 20 ^{o}C. The device is 1.0 μm in radius and 3.5 μm in height. A threshold of 4.1 mA is observed. The series resistance after turn-on is 300 Ω.

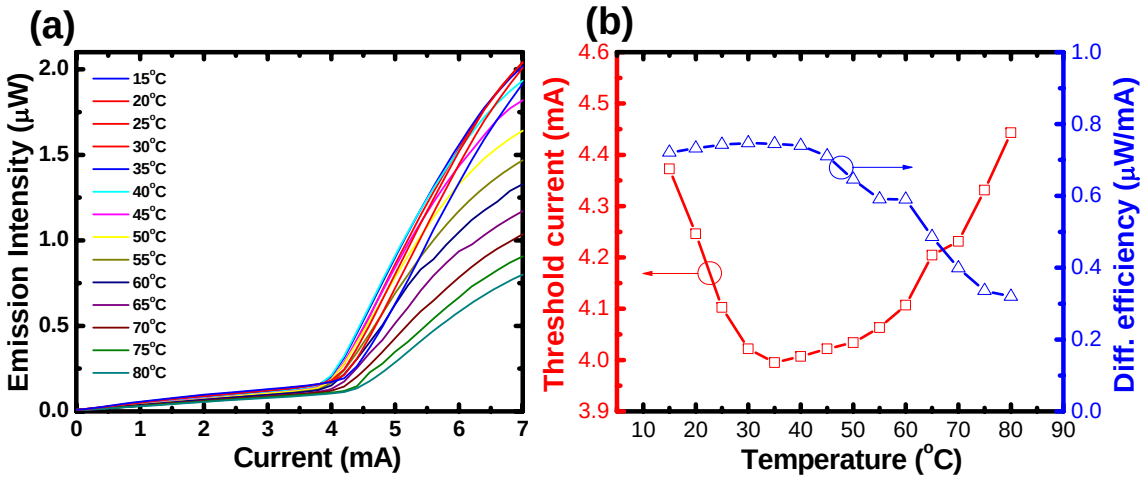

Figure 4.11: (a) Temperature-dependent L-I curves under CW current injection. (b) The threshold current (red) and differential efficiency (blue) as functions of temperature. Both curves show a stable behavior around room temperature.

defined as [45, 46]

$$z = \frac{\Delta T}{\Delta P_{heat}} \tag{4.1}$$

where ΔP_{heat} is the power dissipation due to the thermal effect, and ΔT is the relative temperature difference inside the cavity, reflecting the dissipated power into heat. The power dissipation into heat can be estimated as

$$\Delta P_{heat} = VI - P_{light} \tag{4.2}$$

where V is the voltage drop across the device, I is the driving current, and P_{light} is the light output power. The temperature difference due to the change of injected power can be monitored by

$$\Delta T = \frac{dT}{d\lambda} \times \Delta\lambda \tag{4.3}$$

where $dT/d\lambda$ can be estimated by measuring the wavelength shift as a function of substrate temperature under fixed current near threshold. Our metal-cavity microlaser also shows an improved linewidth [15] compared to others [19,22,23,25,32], which makes the determination of peak position more accurate. Due to the almost full coverage of thick metal, the main heat flow is conducted through the DBR into the metal-covered substrate, which is kept at a constant temperature. Also, the metal coverage on the sidewall further spreads the heat flow toward the metal and silicon substrate, and therefore helps the heat removal through the sidewall metal.

Just above the threshold, the wavelength dependence on the substrate temperature at the fixed current injection is plotted in Fig. 4.12(a). The measured $dT/d\lambda$ is 22.9 ^{o}C/nm (corresponding $d\lambda/dT$ is 4.367×10^{-2} nm/^{o}C). Figure 4.12(b) shows the lasing wavelength as a function of heat dissipation power of the laser (ΔP_{heat}). The temperature shift (ΔT: relative to substrate 20 ^{o}C) versus heat dissipation power can be converted from the peak wavelength versus heat dissipation by Eq. (4.3) using the inverse of the measured slope $d\lambda/dT$ in Fig. 4.12(a).

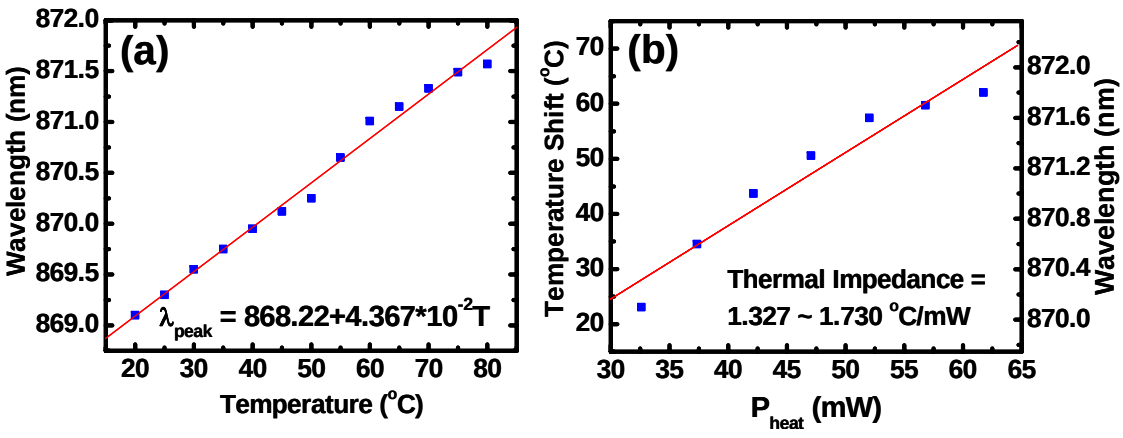

Figure 4.12: (a) The peak wavelength as a function of substrate temperature. The driving current is kept at 4.0 mA. The extracted slope of $d\lambda/dT$ is around 4.367×10^{-2}nm/^{o}C. (b) The thermal impedance of the device with 1.0 μm radius and 3.5 μm height. The measured value is 1.327-1.730 ^{o}C/mW in measurement window (20-80 ^{o}C).

By plotting the temperature shift as a function of heat dissipation power, the thermal impedance of the devices is 1.327 ^{o}C/mW and shows a value of 1.730^{o}C/mW at elevated temperatures. The nonlinearity originates from the accumulation of intrinsic material thermal properties and possibly the material expansion. Compared to other VCSELs with similar sizes summarized in Fig. 4.13 [41–43, 47, 48], our measurement (star) indicates a minimal thermal effect and a comparably lower thermal impedance. Our thermal impedance is much smaller than those of VCSELs with small diameters (less than $4\mu m$) and is as good as those with larger diameters of size 16 μm.

The improvement includes the full metal coverage, which has been shown to help the thermal spreading [41, 42] and the elimination of substrate effect [43, 48]. The reduction of thermal impedance by thinning the substrate has been demonstrated and measured recently [48]. In our work, the complete removal of the substrate from our devices not only reduces heat accumulation due to finite conductivity of the substrate, but also shortens the distance to the metal heatsink. Our substrate-free configuration reduces the substrate effect to a minimal extent. This reduction of thermal impedance is attributed to the metal surrounding, large-area metal bonding, and substrate-free configuration, which help spread and remove

heat more efficiently.

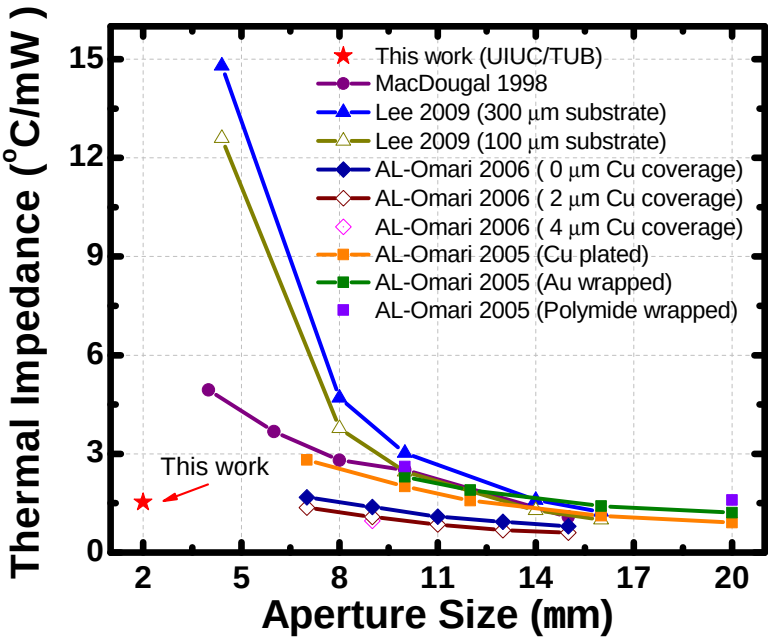

Figure 4.13: The thermal impedance as function of aperture sizes in the literature and this work (star). Our data show a thermal impedance below 1.730 ^{o}C/mW, comparable to those of VCSELs with aperture as large as 10 μm. The reduction of thermal impedance by metal coverage has been shown in Ref. [41,42]. Moreover, the complete removal of substrate significantly helps the reduction of thermal impedance compared to the data from Ref. [48]

CHAPTER 5

METAL-CAVITY SURFACE-EMITTING NANOLASERS

5.1 Strategy for Size Reduction

In the previous chapter, a new class of metal-cavity surface-emitting microlasers is proposed and realized through the help of DBR. The concept of the hybrid mirror consisting of DBR and metal has been used as part of the size reduction scheme. To further reduce the size, the feedback structure has to be shrunk by reducing the number of DBR pairs with a metal hybrid mirror or completely metallic reflector. Figure 5.1 shows the feasibility of further size reduction by tailoring the feedback structures. The device takes advantage of its substrate-free and surface-emitting properties and makes the size reduction flexible.

5.2 Design of Metal-Cavity Surface-Emitting Nanolasers

In this section, we propose and analyze a new class of electrical-injection metal-nanocavity (*nano-coin*) lasers with full coverage of metal, which preserves the surface-emitting and substrate-free configurations. Our design uses metal as a cavity wall on all sides, which eases the requirement of precise design of optical feedback structures such as DBR or cutoff waveguides. With a proper design, the metal-cavity nanolaser can achieve room temperature operation with a physical cavity volume of only 0.01 λ_0^3. The proposed three-dimensional metal-nanocavity laser is shown in Fig. 5.2, which consists of an $In_{0.53}Ga_{0.47}As$ bulk gain material with InP as carrier injectors. To investigate which cavity mode is the best one for laser application, the full structure simulation with real experimental material parameters

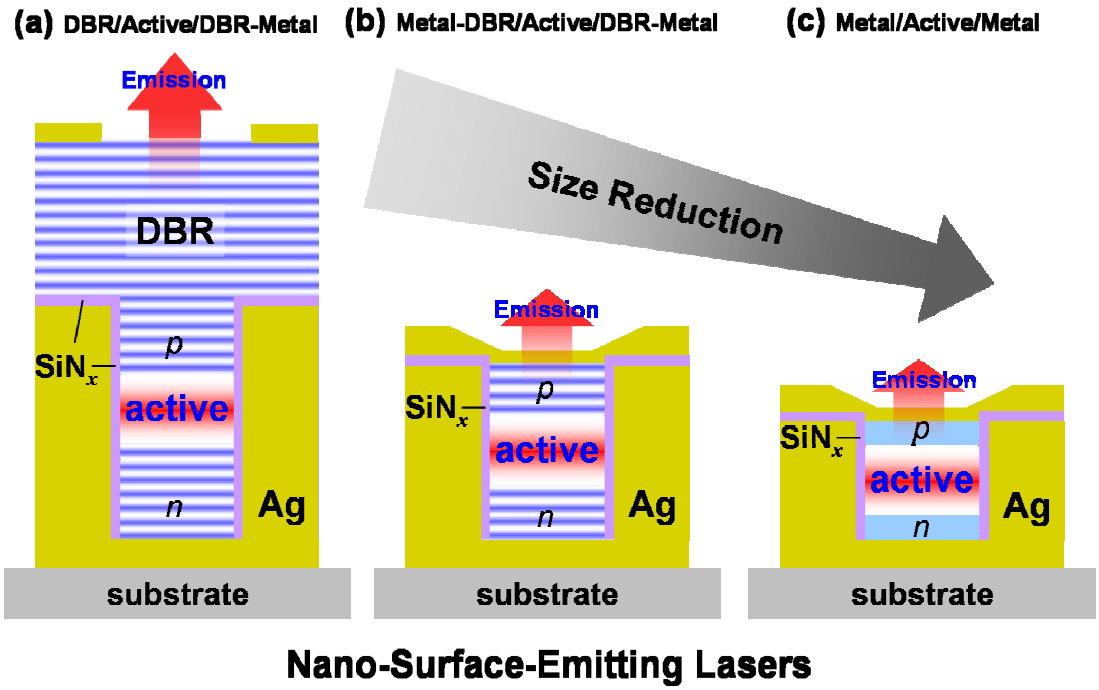

Figure 5.1: The proposed structure and the size reduction scheme with different reflectors: (a) a cavity with feedback from DBR on both sides, (b) a cavity with hybrid DBR/metal reflector as the feedback mirror, and (c) a complete metal feedback. The structures are all shielded by metal (Ag) with a thin silicon nitride (SiN_x) optical and electrical buffer layer. The active materials are sandwiched in between p-n (or n-p) carrier injection layers with an emission window defined on top. Substrate removal and flip-chip bonding on a silicon substrate further reduce the physical size and improve thermal conductivity [49].

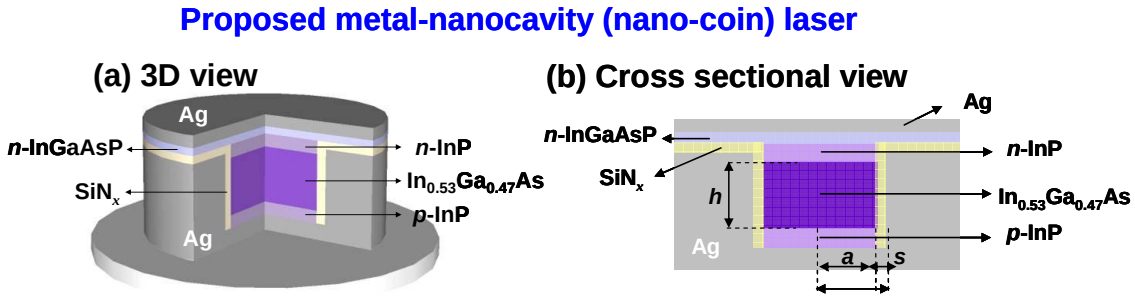

Figure 5.2: Our proposed surface-emitting three-dimensional (3D) metal-nanocavity ($nano-coin$) laser. The active region is composed of a bulk $In_{0.53}Ga_{0.47}As$ with a height h in the active region height and a in radius. InP is used as both electron and hole injectors. An InGaAsP layer serves as a contact layer for n-contact. The whole device is encapsulated in silver with SiN_x as a current blocker. (a) A 3D view and (b) a cross sectional view of the structure [40].

is performed. Figure 5.3(a) shows the resonance wavelengths of the six lowest cavity modes (TM_{010}, HE_{111}, TM_{011}, HE_{211}, TE_{011}, EH_{111}) calculated by FDTD. The structure is shown in Fig. 5.2(a) with vertical 160-nm $In_{0.53}Ga_{0.47}As$, 30-nm n- and p-InP, and 20-nm InGaAsP layer thickness, and a conformal insulator layer of 50-nm SiN_x. The material parameters can be found in Ref. [35,36]. According to the waveguide analysis in section 3.3.1, all modes

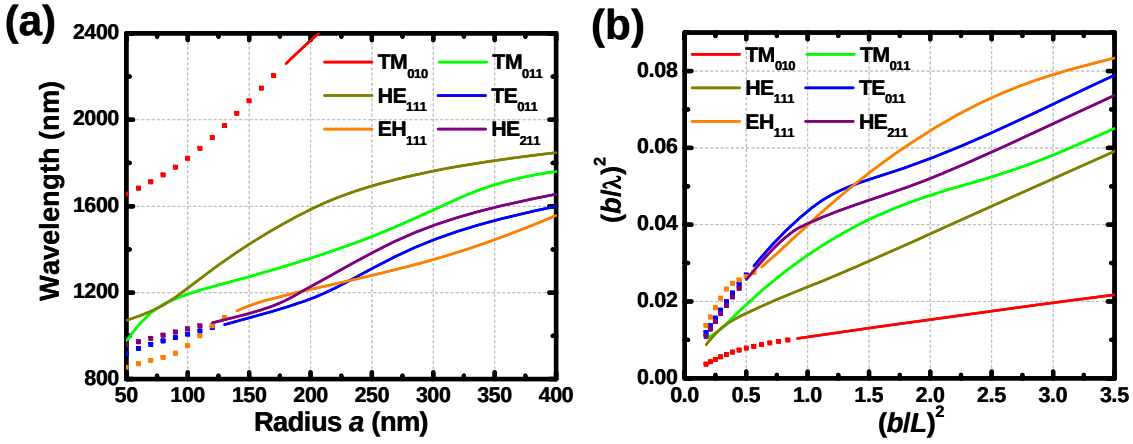

Figure 5.3: Calculated resonance wavelengths of the higher order modes by a full 3D structure FDTD simulation. (a) The resonance wavelengths as a function of the core radius a of the six lowest order modes. (b) Mode chart of the structure curves with the same slope corresponding to the same longitudinal mode number $(p/2n_{op})^2$.

except HE_{111} have a node in either the electric field or the power (P_z) distribution. This node will make a poor overlap between the gain region and the optical field. The dotted line indicates that the resonant wavelength is in the cutoff region of the corresponding waveguide mode. The fundamental mode TM_{010} has a wavelength far greater than the rest due to the zeroth order in the z direction. For a PEC homogeneous cavity (simplified model for understanding), k_z is quantized to $p\pi/L$, and Eq. (3.1) leads to the modal characteristic equation,

$$\left(\frac{b}{\lambda}\right)^2 = \left(\frac{p}{2n_{core}}\right)^2 \left(\frac{b}{\lambda}\right)^2 + \left(\frac{\chi_{mn}}{2\pi n_{core}}\right)^2 \tag{5.1}$$

and the resonant wavelength can be written as

$$\lambda_{mnp} = \frac{2\pi n_{core}}{\sqrt{\left(\frac{\chi_{mn}}{b}\right)^2 + \left(\frac{p\pi}{L}\right)^2}} = \frac{2\pi n_{core}}{\sqrt{\left(\frac{\chi_{mn}}{a+s}\right)^2 + \left(\frac{p\pi}{L}\right)^2}} \tag{5.2}$$

The mode chart for the realistic core-shell-metal planar structure is plotted in Fig. 5.3(b) with the slope representing $(p/2n_{op})^2$, where n_{op} is the effective index (instead of n_{core}) seen by the optical field. In Fig. 5.3(b), the outer radius (core radius a plus shell thickness s) is labeled as b. Although the resonant wavelength of HE_{111} mode is slightly larger than those of the other modes (except TM_{010}) and will result in a slightly larger cavity size, the corresponding waveguide mode (HE_{11}) has the longest cutoff wavelength as shown in Fig. 3.2(a) and allows for a wider range of detuning. The nonzero slope of TM_{010} mode comes from the inhomogeneous permittivity inside the cavity and the asymmetry in the z direction. Moreover, the HE_{111} mode is the most suitable mode for achieving a high gain and optical field overlap. In the following analysis, we will focus on the design for the HE_{111} mode. For an inhomogeneous waveguide with a small permittivity variation, perturbation method can be applied to calculate the resonance wavelength shift from that of a homogeneous waveguide [37, 50]. However, the permittivity contrast between insulator and semiconductor is usually too large to be considered as a perturbation. To properly include the effect of the shell layer, a model with a multilayered structure should be used. As a result of a large negative real part of silver permittivity at the near IR region, the optical modes inside the nanolaser surrounded by silver will be similar to those surrounded by a PEC wall. Figure 5.4 shows the theoretical calculation of the cavity resonance wavelength of the HE_{111} mode in Fig. 5.3, based on the PEC model with the metal wall receding by a skin depth, as a function of the core radius a for various cavity lengths L = 180 to 320 nm. The resonance wavelength gradually becomes shorter and approaches the waveguide cutoff as the geometry shrinks. A transition from core (dielectric) mode (solid lines) to core-shell mode (dashed lines) is indicated by the dispersion curve with the effective index $n_{eff} = n_{shell} = 2.0$. This

transition marks the onset of propagating fields inside the shell region. In the design with real metals, the transition also means more energy penetration into the metal plasma and, thus, results in a higher propagation loss while propagating along the waveguide.

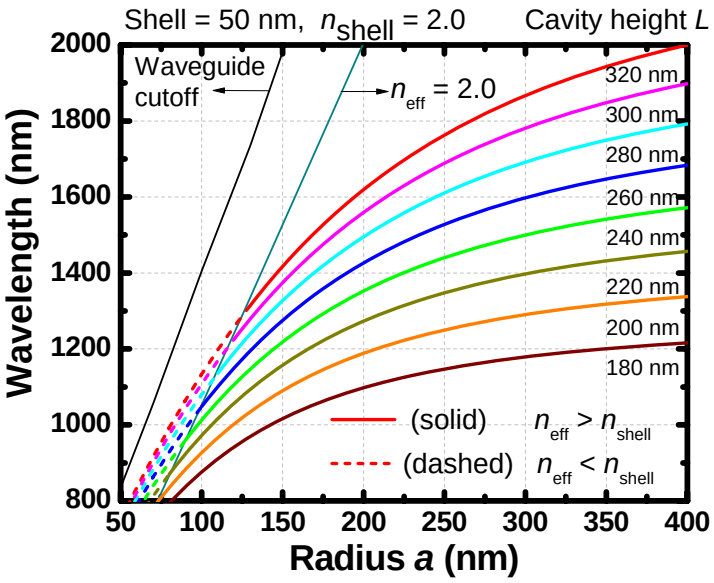

Figure 5.4: The cavity resonance wavelength as a function of the core radius a of various cavity heights L from 180 to 320 nm. The SiN_x shell thickness is fixed at 50 nm. The resonance wavelength with a solid curve is the core (dielectric) mode with $n_{eff} > n_{shell}$. Fields concentrate inside the core region. The resonance wavelength with a dashed curve is the shell mode with $n_{eff} < n_{shell}$. Fields leak out of the core region and the wave can propagate inside the shell region. Lines of waveguide cutoff and transition from core mode to shell mode ($n_{eff} = n_{shell} = 2.0$) are plotted. A PEC model with the metal wall receding by a skin-depth is used in these calculations.

5.3 Simulation Results of the Cavity Properties

To analyze the full nanolaser structure in Fig. 5.2 with specific material properties, we carried out the simulation using the FDTD method. In our design, $In_{0.53}Ga_{0.47}As$ is used as the active material with p- and n- doped InP layers as cladding for contact. The thickness is fixed at 30 nm for both n- and p-doped regions. Also, an n-doped 20-nm InGaAsP layer is used to support the contact area. Silver is used to encapsulate the whole cavity with a low-index material SiN_x in between the semiconductor and metal as a current blocker. At

the output, a thin coat of silver is added to increase the reflectivity and serves as a part of the contact. The material parameters used in the simulation are taken from Ref. [35,36]. Drude model is adopted to fit the metal permittivity for simplicity. In Fig. 5.5, all HE_{111} field plots of our proposed cavity with a radius $a = 190$ nm, $b = 240$ nm, and cavity height $L = 240$ nm are shown. The top view in (a) with the z-component of both E and H fields at the center of the cavity shows their $m = 1$ azimuthal distribution (in the form of $\sin m\phi$ and $\cos m\phi$). Also, the lack of nodal point along the ϕ-direction represents the radial order $n = 1$. In Fig. 5.5(b), the side view of the field components follows HE_{111} mode in their z distribution. Note, in the Fig. 5.5(b) plots, that the azimuthal dependence has been suppressed for simplicity. The symmetry follows the model with $p = 1$ and the field patterns closely resemble those of the PEC waveguide. Figure 5.6 shows the calculated resonance wavelengths and the corresponding quality factors with various heights (220 nm - 300 nm). The thicknesses of SiN_x and the thin silver reflector are both set to 50 nm. The effect of varying these values will be discussed in next section. In Fig. 5.6(a) the resonance wavelength of various cavity

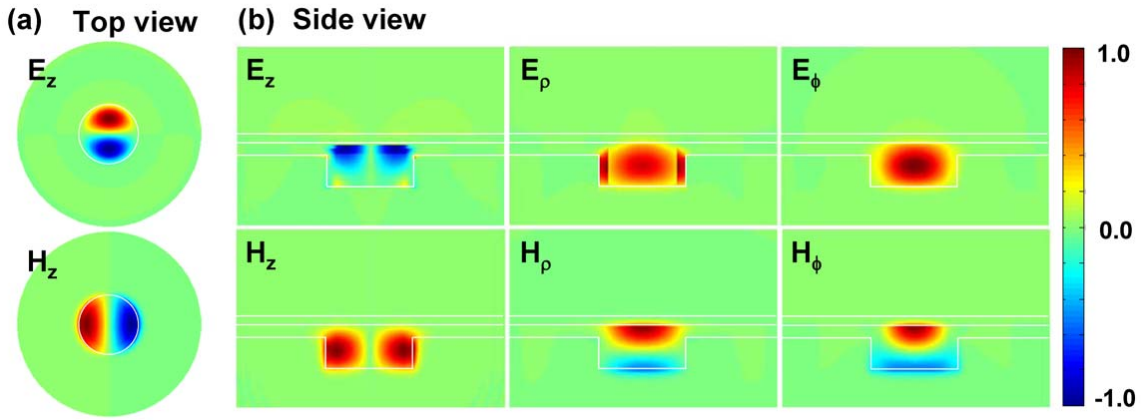

Figure 5.5: (a) Top view of z component of electric and magnetic fields of HE_{111} mode. (b) Side view of all field components inside the cavity. Note the azimuthal dependence for (b) has been suppressed for simplicity.

heights as a function of the core radius can be modeled using the structure analyzed in the previous section by receding the metal wall with a penetration (skin) depth to account for

the finite permittivity in real metals. The dashed lines in Fig. 5.6(a) show the result from the model. Compared to the full structure calculation by the FDTD method, the simplified model agrees very well except at the small radius region where the field leaks into SiN_x and InGaAsP layers. It starts to dominate especially when the effective index becomes smaller than that of the shielding SiN_x layer. By taking the Fourier transform of the time varying

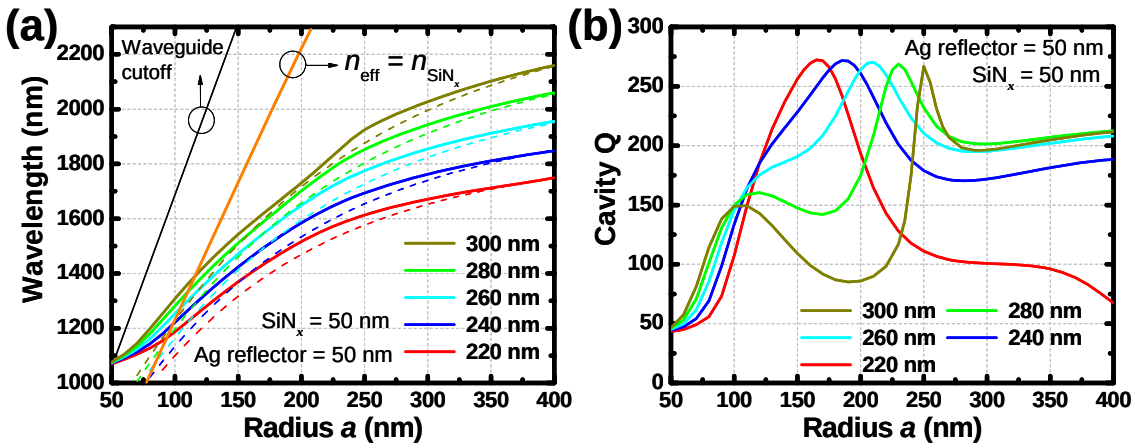

Figure 5.6: (a) Calculated resonance wavelengths of various cavity heights as a function of radius a using the FDTD method (solid curves) for the real structure (including the complex permittivity of the metal) compared with those using the PEC model (dashed curves) presented in previous section. (b) Calculated cavity quality factors as a function of radius. The maximum quality factor is around 275 for all cavity heights.

field inside the cavity, the complex resonant frequency ($\omega_{res} = \omega_r - \omega_i$) of the cavity with metal dispersions can be obtained. ω_r represents the oscillation frequency of the optical field and ω_i is the attenuation due to the loss (both material and radiation). The cold cavity quality factor can be expressed as $Q = \omega_r/2\omega_i$ [51]. Figure 5.6(b) shows the corresponding ideal cold cavity quality factor Q. A clear drop of Q below 100-nm core radius is caused by the energy leakage to SiN_x and InGaAsP layers as described above. The quality factor can be separated into two parts: Q_{rad} from radiation out of the cavity and Q_{mat} from material loss (metal loss). With the calculated field components from the FDTD method, Q_{rad} can

be evaluated from the definition [50, 51],

$$Q_{rad} = 2\pi \frac{\text{Energy stored in cavity}}{\text{Radiated energy per optical periods}} = \frac{\omega W}{P_{rad}} = \frac{\omega \int_V d\mathbf{r} \frac{\epsilon_0}{4} \left[\epsilon_g(\omega, \mathbf{r}) + \epsilon_R(\omega, \mathbf{r})\right] |\mathbf{E}(\mathbf{r})|^2}{\int_S d\mathbf{s} \frac{1}{2} \mathrm{Re}\left[\mathbf{E}(\mathbf{r}) \times \mathbf{H}^*(\mathbf{r})\right] \cdot \hat{n}} \tag{5.3}$$

where W is the total electromagnetic energy inside the cavity, P_{rad} is the radiated power outside of the cavity surface, $\hat{n}$ is the unit normal to the surface, $\epsilon_R(\mathbf{r})$ and $\epsilon_g(\mathbf{r})$ are, respectively, the real part of the relative permittivity and the relative group permittivity, which is defined as [38]

$$\epsilon_g(\omega, \mathbf{r}) = \frac{\partial[\omega \epsilon_R(\omega, \mathbf{r})]}{\partial \omega} \tag{5.4}$$

The material quality factor Q_{mat} due to absorption can then be obtained from Eq. (3.4). The results are shown in Fig. 5.7. The radiation loss has a minimum which originates from minimum energy coupling to a resonant circular slot structure near the output facet [52]. Due to the coupling at this radius, the radiation loss through the composite waveguide of

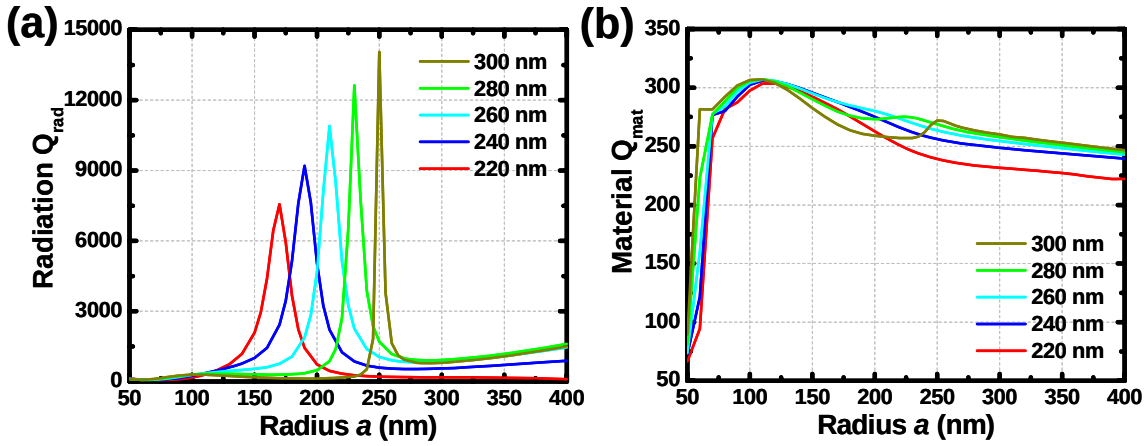

Figure 5.7: (a) The radiation quality factor Qrad of cavities as a function of the core radius a for various heights $L = 220$ to 300 nm. The peaks represent the coupling to a resonance structure. (b) The material quality factor Qmat as a function of radius. The material quality factor has only a minimum change among different cavity heights and radii. A sharp drop at around $R = 100$ nm depicts the transition from core modes to shell modes.

InGaAsP and SiN_x is significantly reduced. According to the result of Q_{mat}, the material

loss has a smooth change and reduces as the radius decreases. This reduction comes from the effective increase of shell layer portion inside the cavity, which buffers the field penetration into metal [31]. One should note the sharp increase of material loss below radius 100 nm. The sharp transition region represents the transition from core (dielectric) mode of the waveguide to its shell mode as discussed before.

In dealing with small lasers, especially with dispersive plasmonic materials like metals, the confinement factor associated with energy should be used to better account for the dispersive and plasmonic effects. The use of the energy confinement factor corrects the improper use of the negative power flow and negative energy resulting from negative permittivity of metals. The energy confinement factor in Eq. (3.5) should be used. In Fig. 5.8(a), the energy confinement factor is shown for various cavity heights. The energy confinement factor

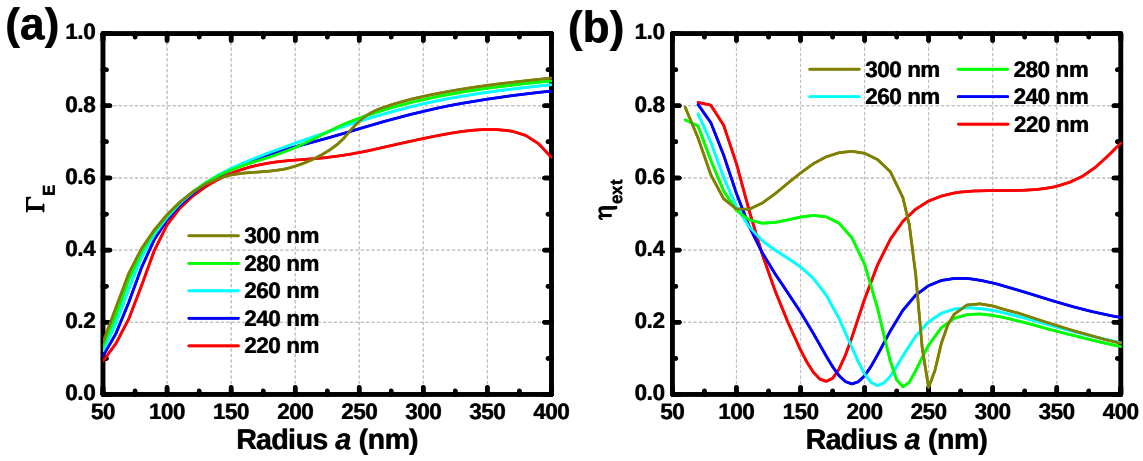

Figure 5.8: The energy confinement factor (a) and extraction efficiency (b) of the cavity as a function of the core radius a with different cavity heights (220 nm - 300 nm). In the inner mode region, Γ_E is above 0.6.

associated with the percentage of active material over the whole cavity increases as both the core radius and height increase. As the radius shrinks, especially when $n_{eff} < n_{SiN_x}$, the energy starts to leak out and results in a reduction in the energy confinement. The overall confinement factors are more than 60% for devices with a radius larger than 100 nm. For a given height, the energy confinement factor approaches a constant and corresponds to the

case that the SiN_x has a minimal effect. Compared to conventional dielectric lasers, which usually have lower values due to poor dielectric confinement, our proposed laser structure with the full coverage by metal helps confine more energy inside the cavity. Figure 5.8(b) shows the extraction efficiency of the cavity, which is a measurement of how much loss contributes to the radiation or light output. It is defined as

$$\eta_{ext} = \frac{Q_{rad}^{-1}}{Q^{-1}} \tag{5.5}$$

A special care has to be taken to get a decent light output. Observing from Fig. 5.8(b), the design with a maximum radiation Q_{rad} can lead to a poor extraction efficiency even though the condition of lasing can be achieved more easily like photonic crystal lasers. The physical sizes are summarized in Fig. 5.9(a). Due to the nature of standing wave formation in HE111

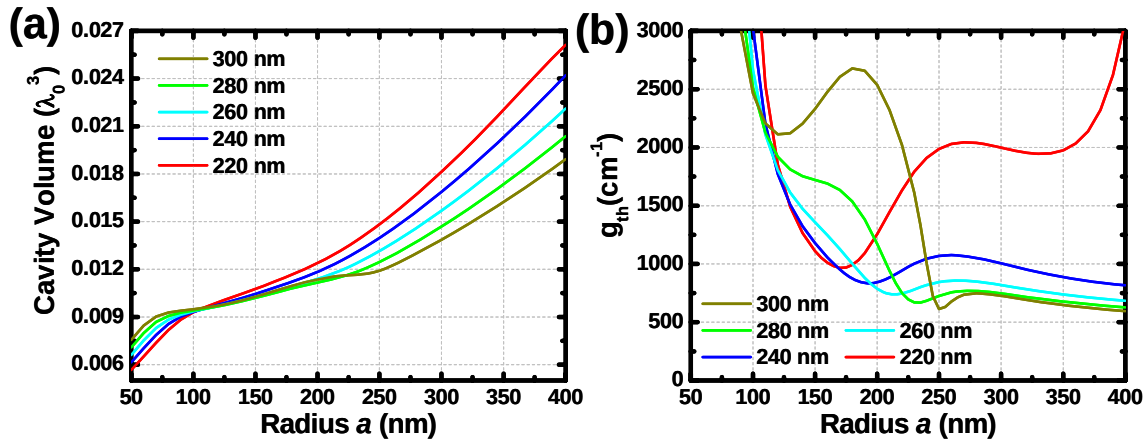

Figure 5.9: (a) The physical cavity volume and (b) the threshold material gain for different cavity heights L = 220 to 300 nm. The cavity volume approaches the diffraction limit $(\lambda_0/2n)^3$. The threshold can be as low as 600 cm^{-1} for $a \geq 250$ nm and cavity heights $L \geq 240$ nm.

mode, the size should be around the minimum standing wave volume or the diffraction limit $(\lambda_0/2n)^3$, where n represents the effective index of the optical mode. With the knowledge of cavity Q, confinement factor Γ_E, and the corresponding resonance frequency λ, the threshold material gain g_{th} can be calculated by Eq. (3.6). The values of g_{th} shown in Fig. 5.9(b) are around 600 cm^{-1} - 1,200 cm^{-1} for cavity heights (240 - 300 nm) and $a \geq 250$ nm and should

be achievable at room temperature within the emission spectrum of $In_{0.53}Ga_{0.47}As$ materials.

5.4 Design Optimization of Metal-Nanocavity Lasers

5.4.1 Effects of shell insulator layer

The shell insulator layer plays a very important role in the design of electrical injection lasers. It is not only an electrical buffer layer but also an effective optical buffer layer for reducing metal loss. Recently, a proper design of the insulator thickness was proven to be useful for reducing the laser threshold by optimizing the material loss from metal and its optical confinement factor [31]. The theoretical results of major physical parameters for a cavity with a cavity height $L = 240$ nm and various SiN_x thicknesses from 20 nm to 80 nm are shown in Fig. 5.10. Since the cavity boundary is defined by metal, it is more illustrative

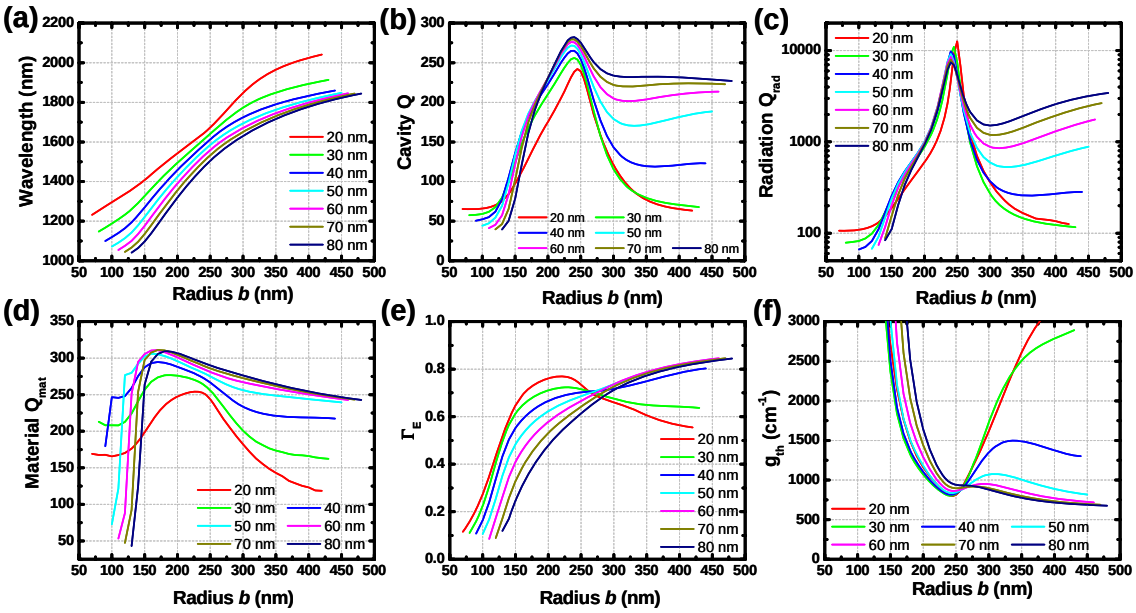

Figure 5.10: The physical properties for different SiN_x shell thicknesses $s = 20$ to 80 nm. (a) The resonance wavelength. (b) The quality factor of the cavity Q. (c) The computed radiation quality factor Q_{rad}. (d) The material quality factor Q_{mat}. (e) The energy confinement factor Γ_E. (f) The threshold material gain g_{th}.

to plot the result as a function of outer radius b (i.e. the radius of the metal wall or the sum

of the core radius a and the SiN_x shell thickness s). Since the boundary remains the same for each b, a smaller change in the resonance wavelength is expected in the larger radius case, where the SiN_x layer occupies only a small portion of the cavity and the field inside SiN_x layer is reduced. In Fig. 5.10(a), the resonance wavelength decreases with increasing SiN_x layer thickness from 20 nm to 80 nm. This is caused by the increase of the average material index inside the metal cavity, or more physically, the decrease of effective wavelength. The cavity quality factors Q in Fig. 5.10(b) are similar in all cases except in the larger radius region. The decrease of quality factor in large radius region as b increases comes mainly from their material loss, or field penetration into metal, as can be seen from Figs. 5.9(c) and (d). For longer wavelengths, the effect of SiN_x layer as a buffer layer for reducing loss becomes smaller; as a result, cavities with the same outer radii will experience more loss if SiN_x becomes relatively thinner compared with the wavelengths. Besides, a thicker SiN_x can help reduce field into the metal or minimize the field leaking out of the cavity as radiation loss. For the confinement factor Γ_E in Fig. 5.10(e), reducing the portion of SiN_x inside the cavity will result in the increase of Γ_E for small radius. For a large radius, the dependence of confinement factor on the SiN_x thickness becomes less obvious except for 20 nm and 30 nm cases in which the wavelengths are longer than the other cases and the radial electric field starts to dominate over the other components (k_ρ increases), thus experiencing more field penetration into the metal. Because of the large permittivity difference between Ag and SiN_x, the field inside the SiN_x builds up as the thickness becomes thinner and this results in the reduction of Γ_E. Figure 5.10(f) shows the corresponding threshold material gain. The minimum threshold material gain for each case has only a small dependence on SiN_x thicknesses. The insulator layer thickness has only a small effect on the resonance wavelength. The optimization should be focused on the confinement factor and material loss issues. In general, the confinement factor will increase with thinner insulator layers for $b <$ 250 nm with a sacrifice of reducing the material quality factor.

5.4.2 Effects of the output metal reflector layer

The metals on the output (or top) facet provides both optical feedback and mode confinement of the cavity. Designs with a thin metal usually suffer from both radiation loss through the metal and ohmic loss dissipated inside the metal [48, 53]. However, designs with a thick metal will regulate the output power. Unlike the other metal surrounding of the cavity, which usually has little constraint on the thickness, the metal reflector on the output facet plays an important role as a cavity wall and an output coupler. Figure 5.11(a) and (b) show the resonance wavelengths and their corresponding cavity quality factors of a 240-nm height cavity with different silver reflector thicknesses. The cavity resonance wavelength, which

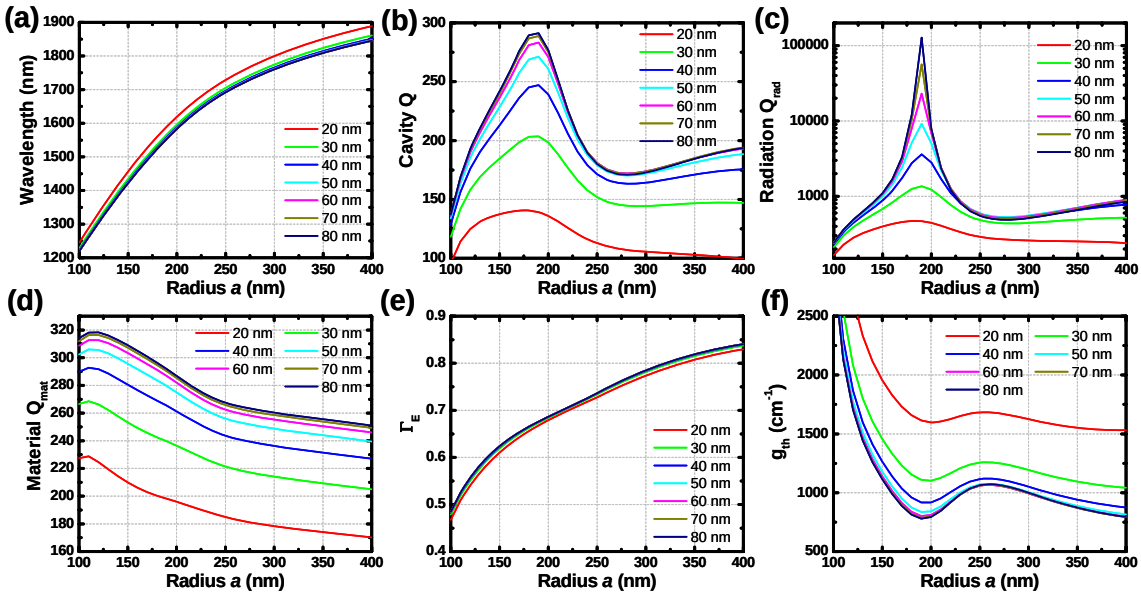

Figure 5.11: The cavity properties with different metal reflector thicknesses from 20 nm to 80 nm. (a) The resonance wavelength. (b) The quality factor of the cavity Q. (c) The computed radiation quality factor Q_{rad}. (d) The material quality factor Q_{mat}. (e) The energy confinement factor Γ_E. (f) The threshold material gain g_{th}.

is determined by the boundary conditions, has little dependence on the metal thickness, especially when the thickness is close to or thicker than its skin depth (for example 15 $\sim$ 30 nm for silver at this optical frequency). The quality factor in Fig. 5.11(b) shows a more obvious dependence on the metal thickness. The separation of Q into Q_{rad} and Q_{mat} is

plotted in Figs. 5.11(c) and (d). The material quality factor shows a strong dependence on the metal thickness. As a result of a large permittivity difference between semiconductor and metal and/or air and metal, the optical field tends to accumulate near the interface. As the metal becomes thinner, fields from both interfaces start to couple and result in a strong field distribution across the metal which in turn contributes to the high material loss for thin metals [48, 53]. In Fig. 5.11(c), the radiation Q_{rad} is shown for various metal thicknesses. Also, as shown in Fig. 5.11(e), the energy confinement factor has an almost unchanged behavior due to the quick decaying tail inside the metal, which usually contains a small portion of the total stored energy in the cavity.

In general, the radiation loss is not the main path of loss out of the cavity. However, in order to get a reasonable output power, the thickness should not be too large. A thicker metal will hinder the light penetration through, or equivalently worsen the extraction efficiency, and has only a minimal increase in the reflectivity. The threshold material gains for different metal thicknesses are shown in Fig. 5.11(f). When the thickness is over 40 nm, the required threshold material gain reduces to below 1,000 cm^{-1} and is achievable for bulk materials at room temperature. According to the calculated result, a design with a metal thickness of around 40 nm to 60 nm should meet the requirement.

5.4.3 Far field radiation pattern

The radiation pattern depends strongly on the cavity mode. For a laser with dimensions comparable to or even smaller than the wavelength, the emission pattern usually is divergent since the fields are strongly localized in the cavity with large wave vectors. In the waveguide case with an open end, the HE_{11} mode preserves the most useful radiation pattern compared to others since it has the smallest $k_\rho (\sim \chi_{11}/b)$. A cavity mode design associated with HE_{11} mode will also prevent a null at the center of the circular waveguide. The radiation pattern

$I(\theta, \phi)$ can be defined as [50–52]

$$I(\theta, \phi) = \frac{\mathbf{P}(r, \theta, \phi) \cdot \hat{r}}{\text{Max}[\mathbf{P}(r, \theta, \phi) \cdot \hat{r}]} \tag{5.6}$$

where $\mathbf{P}(r, \theta, \phi)$ is the Poynting vector in spherical coordinates and Max[·] represents the maximum value over the hemisphere with a constant radius r in the far field. In Fig. 5.12, calculated radiation fields of two dominant components (H_z, E_ρ) of the HE_{111} mode with cavity parameter L = 240 nm, R = 190 nm, R_{out} = 240 nm, and metal thickness = 50 nm are shown. The radiation comes from top metal reflector facet with a high uniform spreading toward the hemispherical space. In the E_ρ plot, a clear guided wave along the

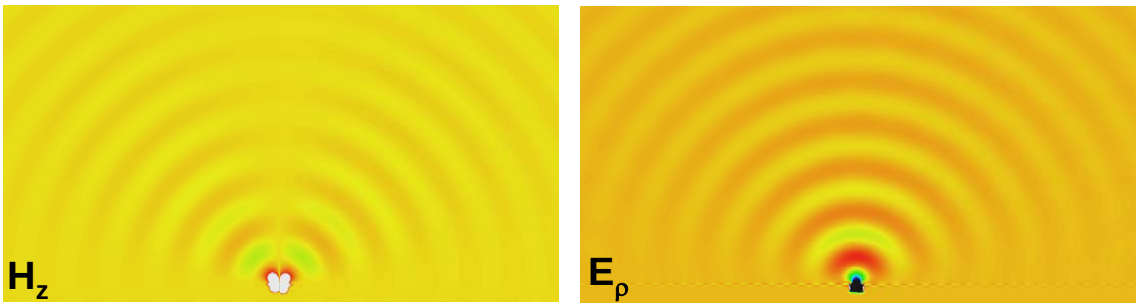

Figure 5.12: Computed far field radiation pattern of H_z and E_ρ components. Note the azimuthal dependence $\exp \pm m\phi$ has been suppressed.

radial direction can be observed in the structure composed of Ag/InGaAsP/SiN_x/Ag hybrid waveguides. These fields do not contribute to the emission into the hemispherical region and have a minimum effect on the radiation pattern. The calculated radiation patterns as a function of θ are shown in Fig. 5.13 for cavities with different radii. Note the azimuthal dependence has been assumed to be in $\exp(\pm m\phi)$ convention. The radiation pattern narrows as the radius becomes larger. The divergence comes from large radial wave component k_ρ at a small radius. A small tail near the interface ($\theta \sim 90^o$) comes from the surface plasma propagation along the Ag/air interface. Compared with nanolasers of other designs such as nanopatches [19, 24], in which the output comes from the interference of fields from the opening sides, our design of the HE_{111} mode with a direct facet output has the advantage of

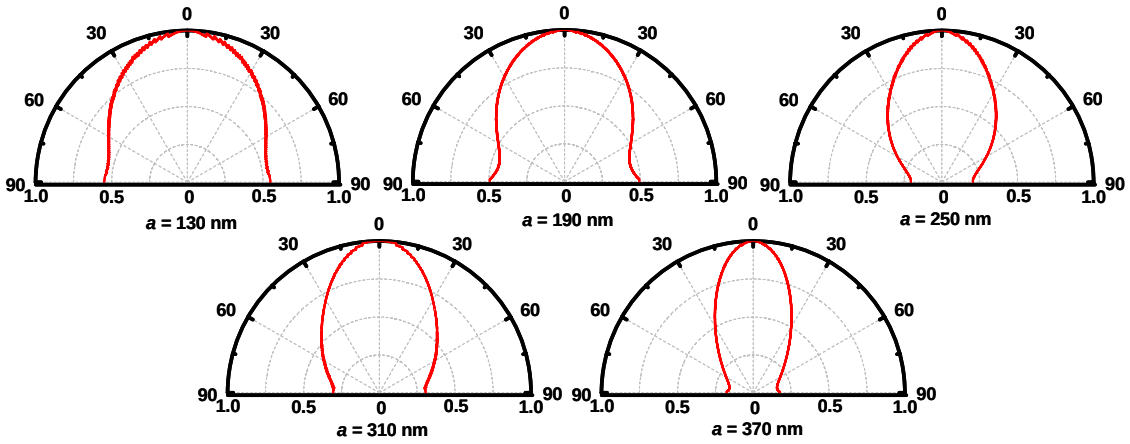

Figure 5.13: Far-field radiation patterns of cavity with different radii, a, from 130 to 370 nm. The azimuthal dependence has been assumed to be $\exp \pm m\phi$. The radiation pattern narrows as the aperture size (radius) increases.

less sensitive radiation pattern dependence on the geometry.

5.5 Threshold Analysis and the Light Output Power

To investigate the possibility of achieving an injection laser and the performance of our proposed metal-cavity structure, we use the rate equations to perform the analysis [37, 38],

$$\begin{aligned}
&\frac{\partial n}{\partial t} = \eta \frac{I}{qV_a} - R_{nr}(n) - R_{sp,cont}(n) - R_{sp} - R_{st}S, \\
&\frac{\partial S}{\partial t} = -\frac{S}{\tau_p} + \Gamma_E R_{sp}(n) + \Gamma_E R_{st}S, \\
&R_{nr}(n) = An + Cn^3, \\
&R_{sp,cont}(n) = \frac{1}{\tau_{rad}V_a} \sum_{c,v,k} f_{c,k}(1 - f_{v,k}), \\
&R_{st} = v_g g(n).
\end{aligned} \tag{5.7}$$

Here n (cm^{-3}) is the carrier density, S (cm^{-3}) is the photon density, η is the injection efficiency, q is the charge of electron, V_a (cm^3) is the volume of active region, R_{nr} ($\mathrm{cm}^{-3}\mathrm{s}^{-1}$) is the non-radiative recombination rate, $R_{sp,cont}$ ($\mathrm{cm}^{-3}\mathrm{s}^{-1}$) and R_{sp} ($\mathrm{cm}^{-3}\mathrm{s}^{-1}$) are the spontaneous emission rate into continuum modes and cavity mode, respectively, $R_{st}S$ ($\mathrm{cm}^{-3}\mathrm{s}^{-1}$)

is the stimulated emission rate, and $g(n)$ (cm^{-1}) is material gain. The non-radiative recombination rate can be modeled as a sum of surface recombination rate (An) plus Auger recombination rate (Cn^3). The coefficient A is given by $v_s A_s$, where v_s is the surface recombination velocity and is set to be 2.0 $\times 10^4$ cms^{-1} [54] and A_s is the surface area of the active region. The Auger coefficient is set to be 4.67×10^{27} $\mathrm{cm}^6\mathrm{s}^{-1}$ [37]. The spontaneous emission rate into continuum modes $R_{sp,cont}$ is calculated by the formula in Eq. (5.7), where τ_{rad} is an effective radiation lifetime (set to be 5 μs) [37] and $f_{c,k}$ and $f_{v,k}$ represent the occupation numbers at wave vector $\mathbf{k}$ in conduction and valance bands.

Figure 5.14 shows the carrier-dependent material gain spectra of the bulk $\mathrm{In_{0.53}Ga_{0.47}As}$ semiconductor calculated by Luttinger-Kohn model at room temperature [39]. Compared with the required threshold material gain for various structures discussed in the context ($\sim$ 700 cm^{-1} - 1000 cm^{-1}), $\mathrm{In_{0.53}Ga_{0.47}As}$ is suitable for achieving room temperature operation at reasonable carrier densities. In Fig. 5.15(a) the light output power as a function of the

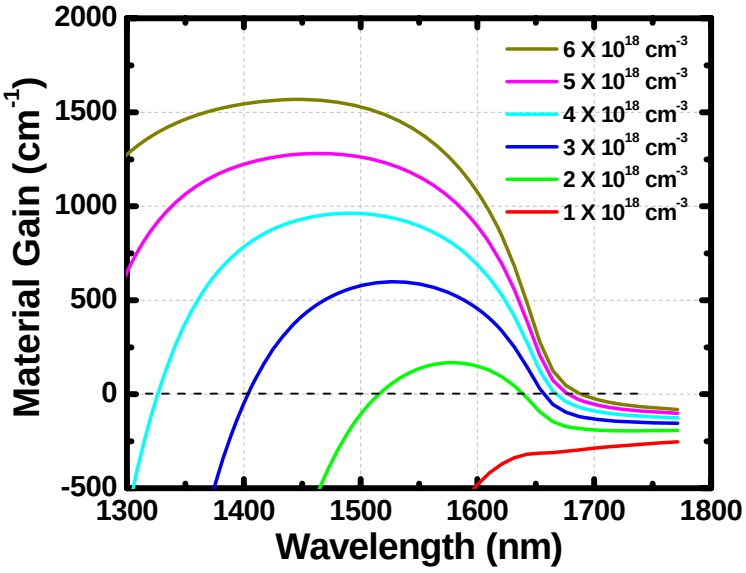

Figure 5.14: Material gain spectra of bulk $\mathrm{In_{0.53}Ga_{0.47}As}$ at different injected carrier densities at room temperature.

injection current (L-I curve) of a device with a cavity parameter L = 240 nm, a = 190 nm, SiN_x shell thickness of 50 nm, b = 240 nm, and metal thickness = 50 nm is shown.

According to the calculation, the output power is predicted to be 22 μW at 1.0 mA current injection with a threshold below 0.1 mA. In Fig. 5.15(b), the transition rates are shown at low current injection range. When the current passes 0.12 mA, the stimulated emission rate starts to take over and the injected power contributes mostly to the lasing mode. The inset shows a turning point of stimulated emission rate (red curve) from stimulated absorption to stimulated emission at $\sim$ 30 μA. The turning point also represents the injection level where the transparent carrier density injection condition is reached (i.e., the net material gain is zero). To illustrate the effect of metal reflectors, a calculation with various metal

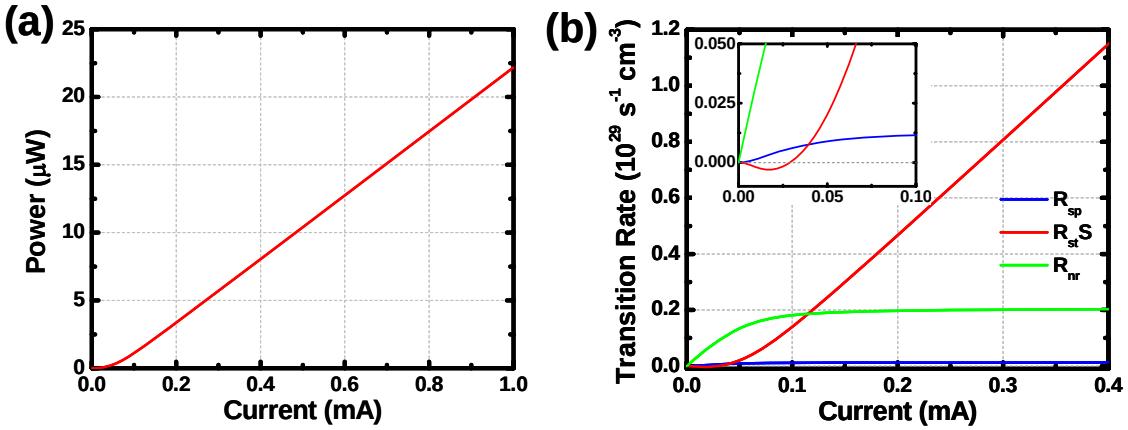

Figure 5.15: (a) The L-I curve at room temperature of a device with a = 190 nm, SiN_x shell thickness = 50 nm, b = 240 nm, metal reflector thickness = 50 nm, and cavity height = 240 nm. (b) The transition rates of the corresponding device. The stimulated emission rate starts to take over after 0.12 mA. (Inset) The turning point from stimulated absorption to stimulated emission (red).

reflector thicknesses is performed. As shown in Fig. 5.16, with a thinner metal reflector (30 nm), the output can be as high as 100 μW at the expense of a higher threshold current due to its lower quality factor. Further increase of the metal thickness will block the output power but reduce the threshold. After 50 nm, the turning point depicting the stimulated emission rate is equal to the non-radiative recombination rate, which remains pinned with increasing current injection. Therefore, further increase of metal thickness will not change the threshold but simply reduce the output power. For an optimized design of power and low

threshold, a nominal metal thickness should be around 40 to 60 nm. In a real situation, not only the thickness of the metal but also the contact resistance will affect the performance. Optimization by inserting a low bandgap material such as InGaAsP in between the p-InP and silver interface can efficiently reduce the contact resistance and, therefore, minimize the heating effect.

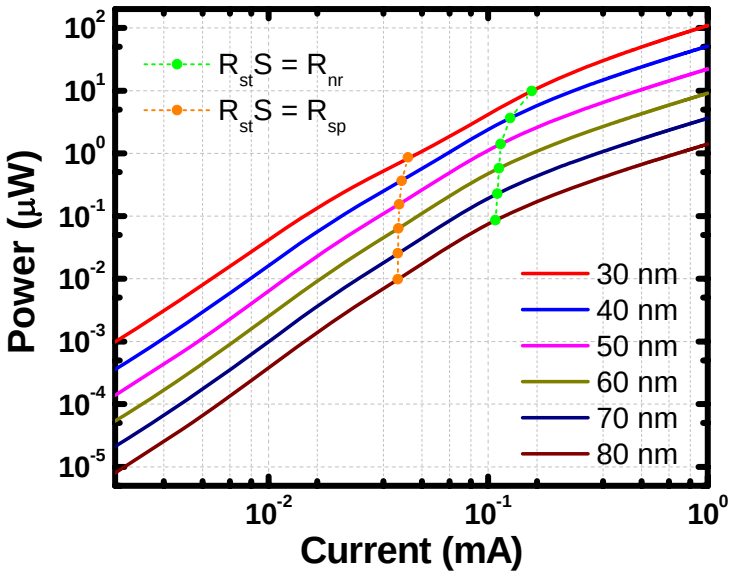

Figure 5.16: The light output power as a function of the injected current (L-I curves) of devices with different metal reflector thicknesses from 30 nm to 80 nm. A transition point when the stimulated emission rate equals the non-radiative recombination rate is plotted as the green symbols. Also, the transition point when the stimulated emission rate equals the spontaneous emission is plotted as the orange symbols.

CHAPTER 6

ADVANCED METAL-CAVITY SURFACE-EMITTING MICRO- AND NANOLASERS

In this chapter, metal-cavity surface-emitting micro- and nanolasers with quantum dots in the active region are represented. Analyses show a promising result toward even smaller devices compared to the same devices using quantum wells. Subwavelength metal-cavity LEDs with InGaAs bulk gain are presented with strategies toward the realization of nanolasers.

6.1 Metal-Cavity Quantum-Dot Surface-Emitting Nanolasers

Due to the metal loss, the realization of metal-cavity lasers so far relies on active materials such as bulk and multiple quantum wells [15,16,18,23,25,32] to provide sufficient modal gain. Although these materials can provide a large modal gain, the gain-deteriorating factors such as dry etching and oxidation would downgrade the performance and reliability. Quantum dots (QDs), as zero dimensional gain materials, have shown many advantages: good confinement of carriers, high differential gain, low chirp, high temperature stability, and reduction of non-radiative surface recombination.

6.1.1 Introduction of submonolayer quantum dots and their advantages

Advanced epitaxy techniques lead to growth of the ultra-high quality quantum dots. Recently, submonolayer (SML) growth [55, 56] further improves the quality of QDs including their ultra-high gain, low carrier diffusion, and most importantly, low material degradation due to their embedded structure in nature. The submonolayer growth method can grow QDs with a higher lateral density than that of the conventional growth method: the

Stranski-Krastanow (SK) mode. Indium arsenide quantum dots by SML are grown by a cyclic deposition of InAs submonolayer and capped by GaAs monolayers; the resulting absence of a wetting layer can lead to several advantages compared to SK QDs, such as the reduction of scattering from adjacent wetting layer states, the avoidance of wetting layer population, and a higher differential gain [57].

6.1.2 Fabrication and analysis

Figure 6.1(a) shows the schematic of our fabricated metal-cavity devices. The laser structure

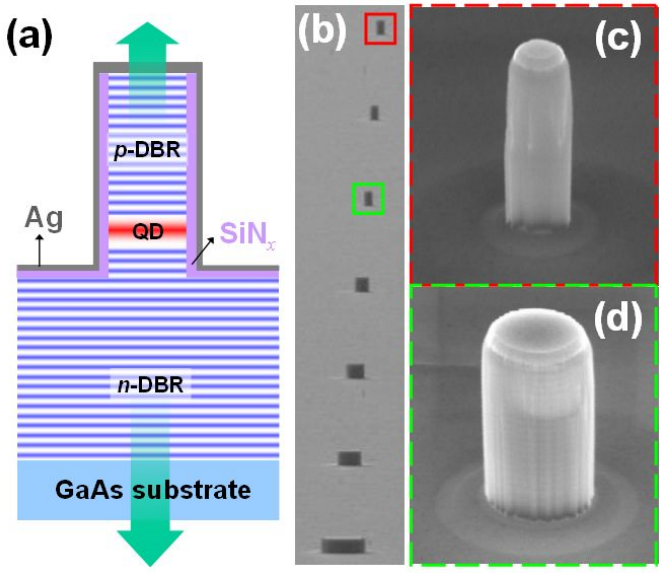

Figure 6.1: (a) Schematic of our QD metal-cavity surface-emitting microlasers. Silver is used to form the cavity which contains 3 layers of SML QDs as the gain medium. The feedback from top and bottom DBR further increases the quality factor of the metal-cavity. (b) A SEM picture showing an array of devices with various dimensions (10 μm down to 1 μm). Magnified SEM pictures of a 1 μm device and a 2 μm device after SiN_x coating are shown in (c) and (d).

was grown by molecular beam epitaxy. The active region consists of three groups (each with an 8 nm thickness) of SML QDs [55, 56] with a 13-nm-thick GaAs spacer layer, where each group has ten stacked SML QD layers, while each layer contains 0.5 monolayer (ML) of InAs capped by 2.2 ML of GaAs. The dot density is estimated to be $2-3\times10^{10}$ cm^{-2} [56]. Distributed Bragg reflectors formed by alternating $Al_{0.9}Ga_{0.1}As$/GaAs were grown to serve

as the top (bottom) mirror, in-between which the optical cavity is sandwiched. The structure is similar to that in [55] except for the 3 (instead of 4) groups of SML QDs in a $3\lambda/2n_r$ cavity with 19/32 p-doped/n-doped DBR pairs. To form the microcavity, photolithography with silicon nitride (SiN_x) as a mask defined the geometry of various diameters (10, 5, 4, 3, 2, and 1 μm). Cylindrical microcavities were then fabricated by dry-etching, which was processed 4 pairs below the active region. The scanning electron micrographs (SEMs) of a device array with various diameters after SiN_x coating are shown in Fig. 6.1(b)-(d). The smallest device is $\sim$ 1 μm in diameter. A thin silver conformal coating was applied to the cavity surface after the passivation of the sidewall by SiN_x. To reduce the metal loss, the thickness of SiN_x was optimized to buffer the optical field penetration into the metal while maintaining a good optical energy confinement factor.

Devices were mounted on a copper holder with a thermoelectric cooler to hold constant measurement environment at 293 K. A dual-mode current source with 10 μA accuracy was used to drive the device under continuous or pulsed modes. Figure 6.2 shows the light output vs. current (L-I) and voltage vs. current (I-V) curves of the QD microlaser with a diameter of 10 μm. The microlaser showed a pulsed threshold of 6.5 mA and a slightly

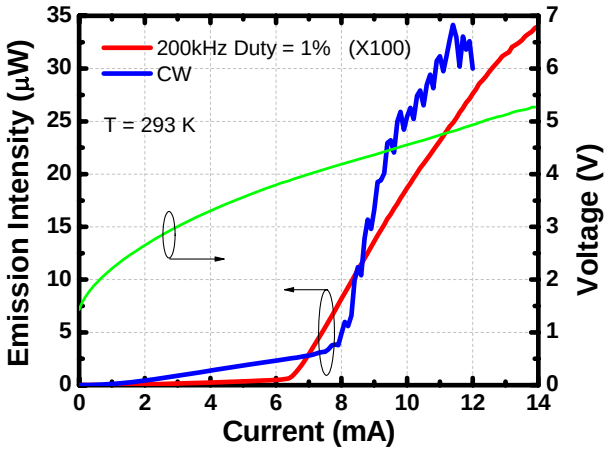

Figure 6.2: Characteristics of a 10-μm diameter device at 293 K. Blue and red curves show the L-I curves under CW and pulsed current injection. The thresholds are 6.5 mA for pulsed mode and 8.2 mA for CW mode. The output power before saturation is $\sim$ 32 μW. The green line is the I-V curve. The series resistance after diode turn-on at $\sim$ 1.5 V is 190 Ω.

higher CW threshold around 8.2 mA due to heating. The maximum power before thermal rollover was around 32 μW. The device shows a good turn-on voltage around 1.5 V and the series resistance after turn-on is 190 Ω. The unstable CW output came from the rapid mode switching which resulted from thermal jittering and mode competition. Figure 6.3 shows the room-temperature lasing spectra of a 5-μm diameter device operating at pulsed mode (200 kHz, 10 % duty cycle). The lasing peak is 967 nm. The inset in Fig. 6.3 shows the corresponding L-I curves with 10 % and 1 % duty cycles. The threshold is $\sim$ 3.7 mA for both cases. A slightly smaller threshold is observed for the 10 % case due to thermal assisted alignment of the gain peak and cavity resonance. Compared to our results on

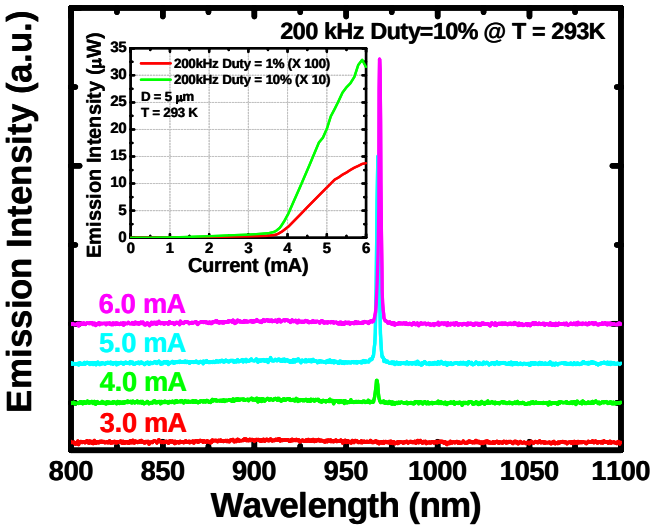

Figure 6.3: Current-dependent spectra of a 5-μm diameter device. The spectra were taken with pulsed mode (200 kHz and 10 % duty cycle). A lasing peak at 967 nm was observed after passing the threshold $\sim$ 3.7 mA. The inset shows the corresponding L-I curves of 10 % and 1 % duty cycle at 293 K.

microlasers using QWs near the same wavelength (980 nm) [18], which have a strong passing band spontaneous emission due to the step-like gain spectrum, the delta-function-like QD density of states helps the suppression of spontaneous emission from the passing band such as wetting layer state emissions, especially at high injection currents. The reflectivity of the DBR was estimated to be 0.9934 (top 19 DBR pairs) and 0.9979 (bottom 32 DBR pairs).

The overall cavity modal gain G (i.e. intrinsic loss + mirror loss) is $\sim$ 146 cm^{-1}, and the longitudinal confinement factor Γ_l could be calculated by the ratio of total SML QDs layer thickness to the optical cavity length and was found to be 0.0538. The material gain per QD layer required for the laser action should be $G^t_{th} = G/(\chi\Gamma_l) = 1,356$ cm^{-1}, where $\chi \approx 2$ is the longitudinal enhancement factor (assuming ideal case). Assuming a nominal dot size of 10 nm and the density of 3×10^{10} cm^{-2} [55], the threshold material gain should be achievable at room temperature. Compared with our previous work using five quantum wells with a similar structure, which requires an overall modal gain of 150 cm^{-1} [18], the use of only three groups (8 nm each) of QDs may require a higher injection current for smaller diameters. The QD lasers provide efficient carrier confinement and show a wider laser operation current before rollover than the QW devices. The smallest device exhibiting room-temperature laser operation at pulsed mode is 4 μm in diameter. Smaller devices (i.e. 1, 2, and 3 μm) were also successfully fabricated with cavity modes observed under electrical injection at room temperature. Further optimization on a better cavity resonance wavelength design taking into account modal dispersion and the improvement of the quality factor using a hybrid metal-DBR reflector is in progress for further size reduction. Increasing the dot density, uniformity, and the number of QD layers inside the cavity will improve the optical gain, confinement factor, and the laser threshold toward room temperature nanoscale laser operation.

6.1.3 Size effect

To investigate the possibility of size reduction, devices with various diameters were fabricated on the same structure. Different from previous devices, the silver coating was made thicker and the output power came only from the bottom (through the substrate). Figure 6.4 shows a series of L-I and I-V measurements of devices with different sizes. The measurement was done at room temperature where the active cooling was absent. The smallest working device is of a diameter 1 μm operating under pulsed current injection at 0.1 %. The threshold

is around 3.6 mA with an averaged output of several nanowatts. In Fig. 6.4 (b)-(f), a pulsed current source of duty cycle 1.0 % was used to drive the devices of a diameter 2 to 10 μm. As the size gets smaller, due to the shrinking of cross section, the series resistance

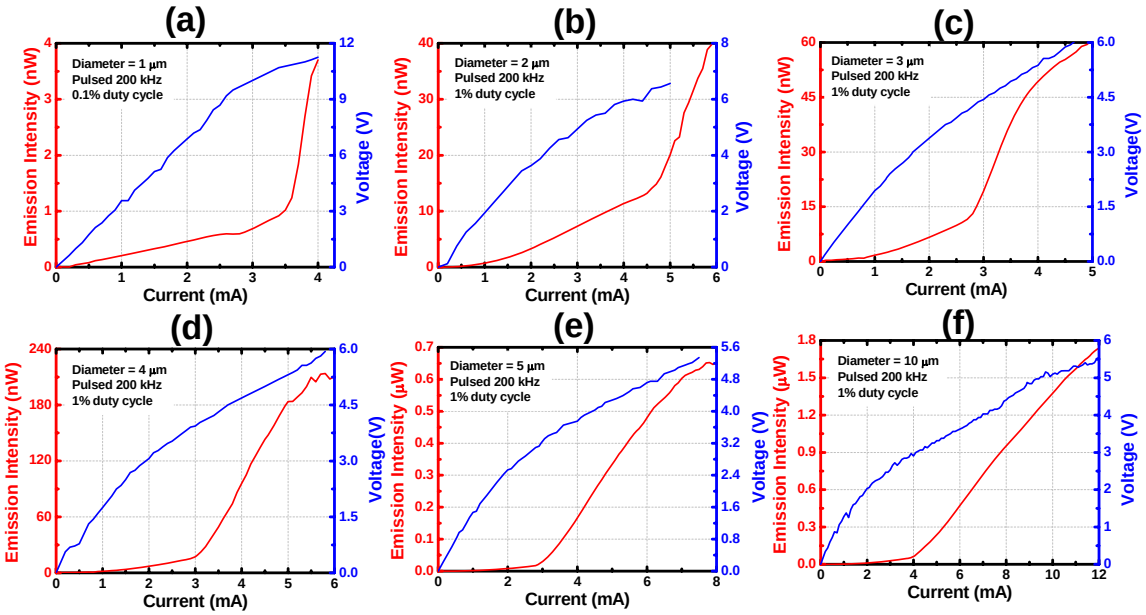

Figure 6.4: The L-I and I-V curves of devices with different diameters. The measurement was done under room temperature with pulsed current injection. (a) D = 1 μm @ 0.1% duty cycle, (b) D = 2 μm, (c) D = 3 μm, (d) D = 4 μm, (e) D = 5 μm, and (f) D = 10 μm @ 1% duty cycle.

increases dramatically. Figure 6.5 (a) shows the I-V curves of different devices with different sizes. In Fig. 6.5 (b), the diameter-dependent series resistances are shown for diameters 1, 2, 3, 4, 5, and 10 μm. The series resistance increases to over 4 kΩ for the smallest 1 μm working devices and has a low value of $\sim$ 400 Ω for the 10-μm device. Continuous-wave lasing was observed for devices of diameters from 10 μm down to 4 μm, as shown in Fig. 6.6. Devices with a diameter of 2 μm can work up to 5 % duty cycle, and 3 μm up to 10 % duty cycle. The diameter-dependent threshold current densities (J_{th}) are plotted in Fig. 6.7 (a). The threshold current density increases rapidly as the size approaches the wavelength. The origins of the increase of the threshold current density for small devices come from geometry effect such as the vertical sidewall, surface roughness, and etching profile uniformity. More importantly, the material damage from the surface contributes to the current leakage and

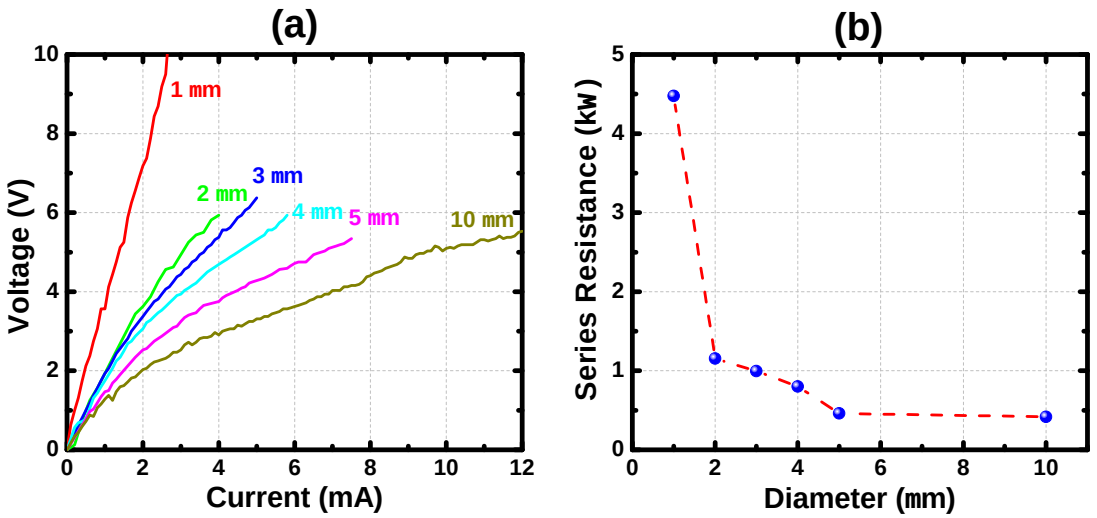

Figure 6.5: (a) Current-voltage curves of devices with diameters 1, 2, 3, 4, 5, and 10 μm. (b) Diameter-dependent series resistance after the device turn-on. The resistance increases dramatically with decreasing size, reaching over 4 kΩ for the 1 μm device

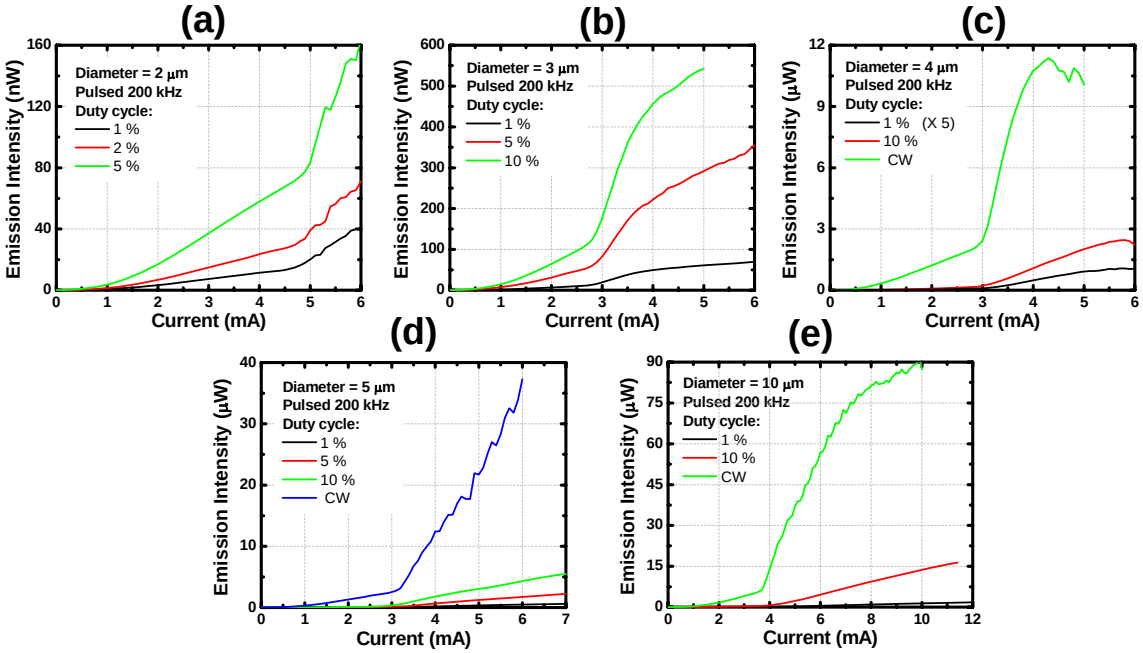

Figure 6.6: L-I curves under different conditions for various devices with different diameters. (a) 2-μm device working up to 5 % duty cycle, (b) 3-μm device working up to 10 % duty cycle, (c) 4-μm device working at continuous-wave mode, (d) 5-μm device working at continuous-wave mode, (e) 10-μm device working at continuous-wave mode.

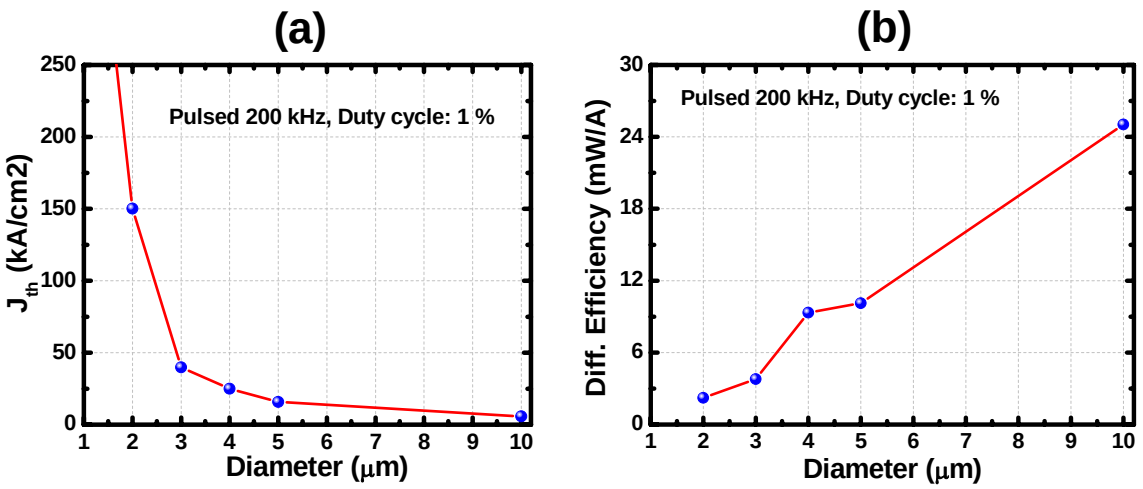

Figure 6.7: (a) The threshold current densities of devices with different diameters. The measurements were done under pulsed current injection with duty cycle of 1 % (except the 1-μm-diameter device: 0.1 %). The threshold current density increases significantly when the device diameter approaches the wavelength. The smallest device with 1 μm diameter shows a threshold current density of 452 kA/cm^2. (b) The diameter-dependent differential efficiencies of different devices. The efficiency decreases with reduced diameters for increased metal loss and possibly current leakage. The efficiency ranges from 25 mW/A for 10-μm devices to 2.2 mW/A for 2-μm devices.

can become severe when the surface to volume ratio increases. Although the metal coating tightly confines the optical field inside the pillar, the introduction of ohmic loss gives rise to the low quality factor especially for devices with the size approaching the wavelength. On the other hand, the modal dispersion further shifts the resonance wavelength away from the high reflection window, especially when the device diameters are small. All these strongly size-dependent parameters affect the radiation loss, intrinsic loss from metal, current leakages, and scattering loss due to surface. The shift of the phase and the resulting lowering of the reflectivity lead to the increase of required gain for achieving laser action. For the smallest devices (1 μm diameter and operating at 0.1 % duty cycle), the value goes up to 452 kA/cm^2. Figure 6.7(b) shows the differential efficiency (η) for the devices with different diameters. For the simplest case, the differential efficiency should be

$$\eta = \eta_i \left(\frac{\alpha_m}{\alpha_m + \alpha_i} \right) \times \left(\frac{P_{laser}}{P_{rad}} \right) \tag{6.1}$$

where η_i is the internal overall efficiency which accounts for internal electrical to optical power conversion, α_m and α_i are the mirror loss and intrinsic loss, and P_{laser}/P_{rad} is the ratio of laser output power to total radiated power out of the cavity. For small devices, the intrinsic loss starts to increase significantly due to the proximity to the metal. Meanwhile, the injection efficiency also drops due to the leakage current from the surface recombination and other non-radiative processes. Scattering and diffraction due to a small aperture could also lower the power. In Fig. 6.7(b), the efficiency ranges from 25 mW/A for 10-μm devices to 2.2 mW/A for 2-μm devices and shows a decreasing trend due to increasing loss and poor injection for small devices.

6.1.4 Size-dependent properties: cavity modes

To investigate the issues for further size reduction, a study of a series of diameter-dependent cavity modes was performed. The devices were kept at room temperature on top of a metal heatsink without an active cooling. A continuous wave current source was used to drive the device to have a stable spectrum and avoid any transient effects resulting from frequent switches of the device. The collected light was dispersed by a monochromator equipped with array Si-CCD detectors. Figure 6.8 shows the current-dependent spectra of a 10-μm-diameter device. The cavity modes are clearly resolved with the fundamental HE_{11} mode with the longest wavelength at around 967 nm. When the current increases, the cavity modes also shift as a result of both the cavity expansion and the refractive index change due to heating. At the same time, observing from the amplified spontaneous emission spectra, the gain spectra also shift due to band-filling (blue) and bandgap-shrinkage (red).

Figure 6.9 shows the current-dependent emission mapping of a 4 μm-diameter device. The more sparse mode spacing ($\sim$ 1.8 nm) compared to that ($\sim$ 0.3 nm) in Fig. 6.8. The shift of the cavity modes toward longer wavelength was observed. Due to the heating of the cavity, the cavity length expands (assuming a minimal expansion in radial direction which is usually large compared to longitudinal cavity length) and the refractive index shrinks

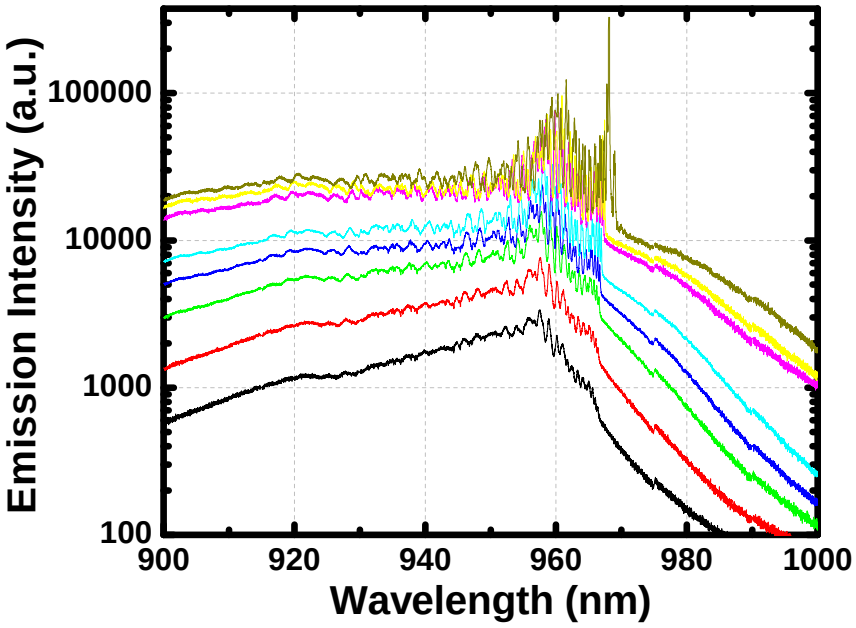

Figure 6.8: Spectra of a 10-μm-diameter device under continuous-wave current injection at room temperature. The cavity modes were observed with the fundamental mode HE_{11} at the longest wavelength side. The red shift of the cavity mode comes from both the cavity expansion and the refractive index change due to heating effect.

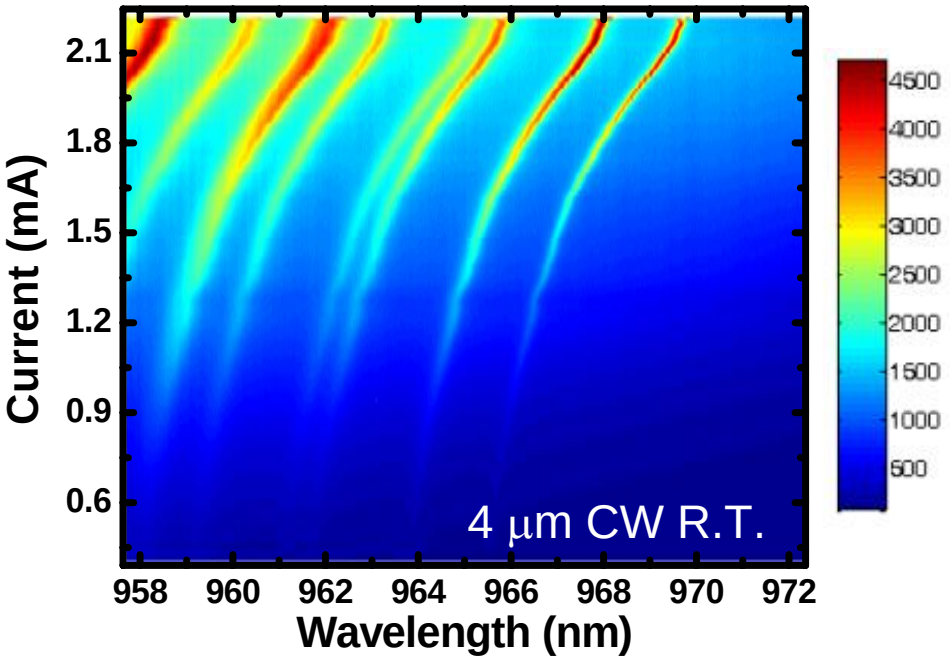

Figure 6.9: Current-dependent spectra mapping of a 4 μm-diameter device.

due to bandgap renormalization and carrier-induced screening. Assuming a linear thermal impedance at low current injection and a linear relation between the cavity temperature and the cavity resonance wavelength, the red-shift of cavity resonance wavelength ($\lambda_c(I)$) follows the quadratic current (power) relation ($\lambda_c(I) - \lambda_c(I=0) \propto I^2$). At high current injection, however, as a result of large heat accumulation and the large temperature gradient between cavity and the environment, the generation and dissipation of heat reach a steady state and give a constant temperature when injecting more current, and, thus, the cavity resonance stops moving. The size shrinkage will also give rise to larger mode separation as a result of the increased spacing between the radial wave vectors ($k_\rho \sim 1/a$). The size-dependent spectra are shown in Fig. 6.10. The first two modes HE_{11} and TE_{01} are identified in the

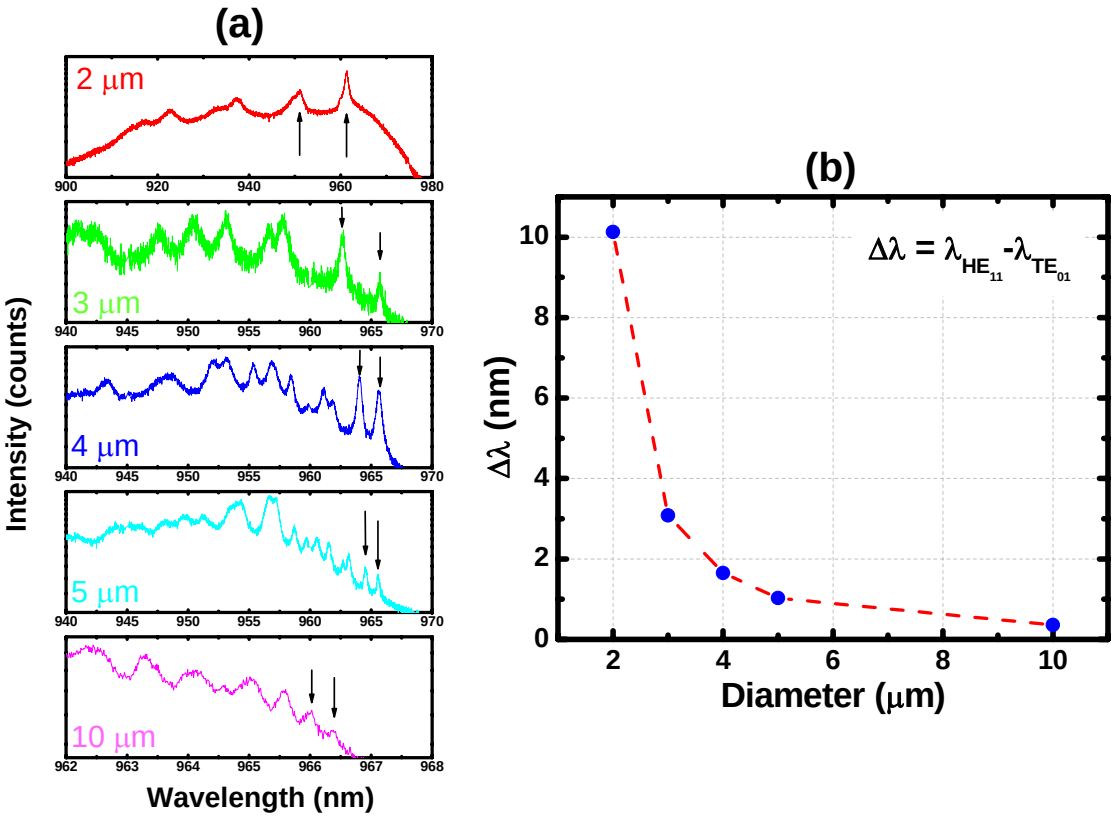

Figure 6.10: (a) Size-dependent spectra of devices with diameters of 2 μm, 3 μm, 4 μm, 5 μm, and 10 μm. The arrows indicate the first two modes (HE_{11}: right and TE_{01}: left). (b) The mode spacing Δ_λ between HE_{11} and TE_{01} modes. The spacing increases from $\sim$ 0.3 nm for a 10 μm-diameter device to $\sim$ 10 nm for a 2 μm-diameter device.

spectra of devices with different diameters. In Fig. 6.10(a), the mode spacing ($\Delta\lambda$) increases as the size shrinks. The corresponding results as a function of device diameters are plotted in Fig. 6.10(b). The mode spacing increases from $\sim$ 0.3 nm for a 10 μm-diameter device up to $\sim$ 10 nm for a 2 μm-diameter device. Figure 6.11(a) shows the fitting result using Fabry-Pérot formula developed in the previous chapters. The results show a good agreement

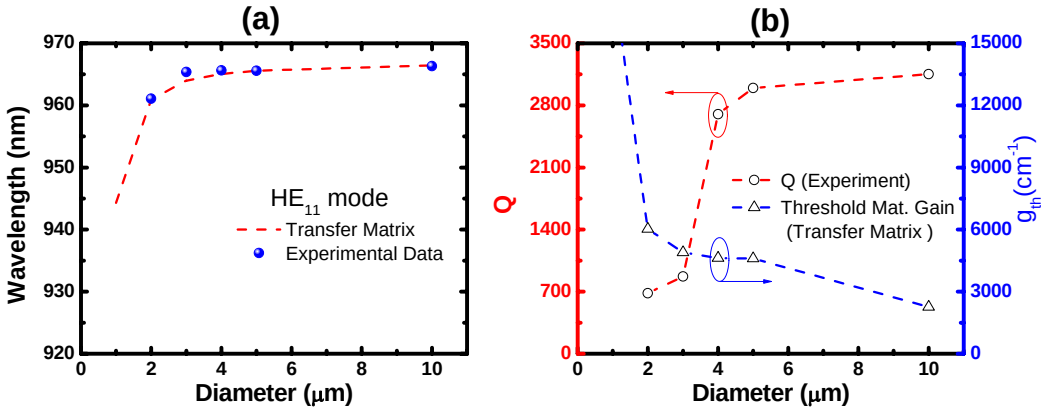

Figure 6.11: (a) The resonance wavelength of the fundamental HE_{11} mode of different diameter devices under low bias current ($\leq$ 0.5 mA). The solid symbols represent the experimental data and the dashed line shows the theoretical calculation by the Fabry-Pérot model. (b) The diameter-dependent quality factors extracted from the spectra and the corresponding threshold material gain calculation by the Fabry-Pérot model.

between the theory and the experiment. The rapid falling of resonance wavelength for smaller diameters results from the inverse proportional relation between the radial wave vector and the diameter. From the linewidth of the cavity modes at low current injection, the quality factors of the fundamental mode HE_{11} can be determined. The results are shown in Fig. 6.11(b) along with the calculated threshold material gain by the Fabry-Pérot model. The quality factor drops when the size reduces due mainly to the detuning from high reflection window of the cavity as well as the metallic loss from the sidewalls. The simulated threshold material gain (assuming uniform quantum well for quantum dots) also reflects the result of low quality factor for small devices.

6.2 Metal-Cavity Quantum-Well Surface-Emitting Nanolasers

To investigate the advantages of QDs, comparison devices were made with an almost identical structure except that the active region is replaced by quantum wells (QWs). The laser structure was grown by molecular beam epitaxy. The active region consists of three quantum wells (compressive well: $In_{0.17}Ga_{0.83}As$ - 6 nm, with strain-balanced barriers: $Ga_{0.92}As_{0.08}P$ - 4 nm). Distributed Bragg reflectors formed by alternating $Al_{0.9}Ga_{0.1}As$/ $Al_{0.12}Ga_{0.88}As$ were grown to serve as the top (bottom) mirror, in-between which the optical cavity is sandwiched. The quantum wells are in a $3\lambda/2$ cavity with 23/38 p-doped/n-doped DBR pairs. Devices were fabricated parallel under the same condition as QDs devices. Figure 6.12 shows the size dependent L-I curves and I-V curves under pulsed operation. For a fair comparison, the measurement was done at the pulse mode to eliminate the heating effect which might be

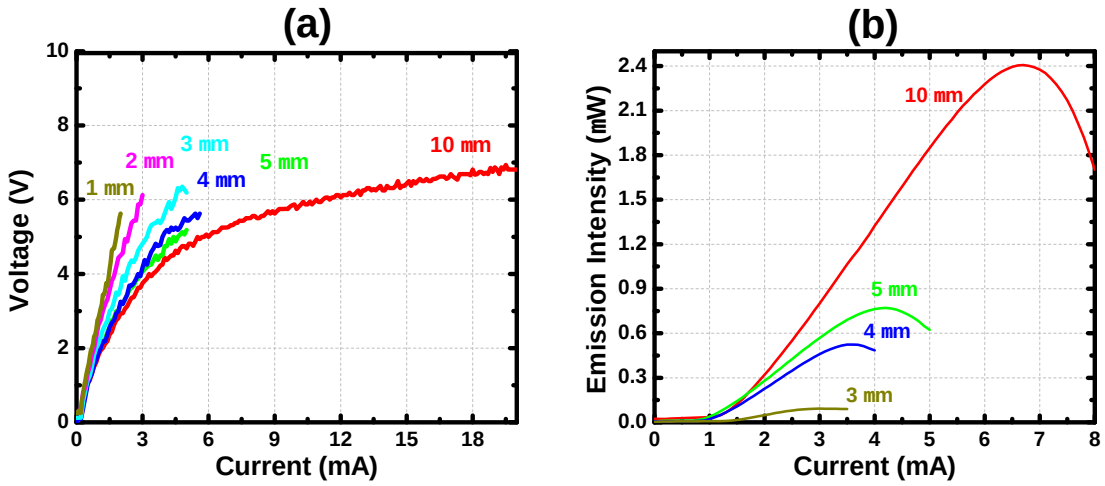

Figure 6.12: (a) I-V curves and (b) L-I curves for various devices with different diameters. The measurement was done at room-temperature without active cooling under pulsed current injection (200 kHz) 1 % duty cycle. The smallest working device is 3 μm in diameter.

different due to nonidentical doping levels in these two layer structures, and this can be seen from the I-V curves as shown in Fig. 6.12(a). The devices stop lasing when the diameter is smaller than 3 μm. The L-I-V curves of individual devices with different diameters are plotted in Fig. 6.13.

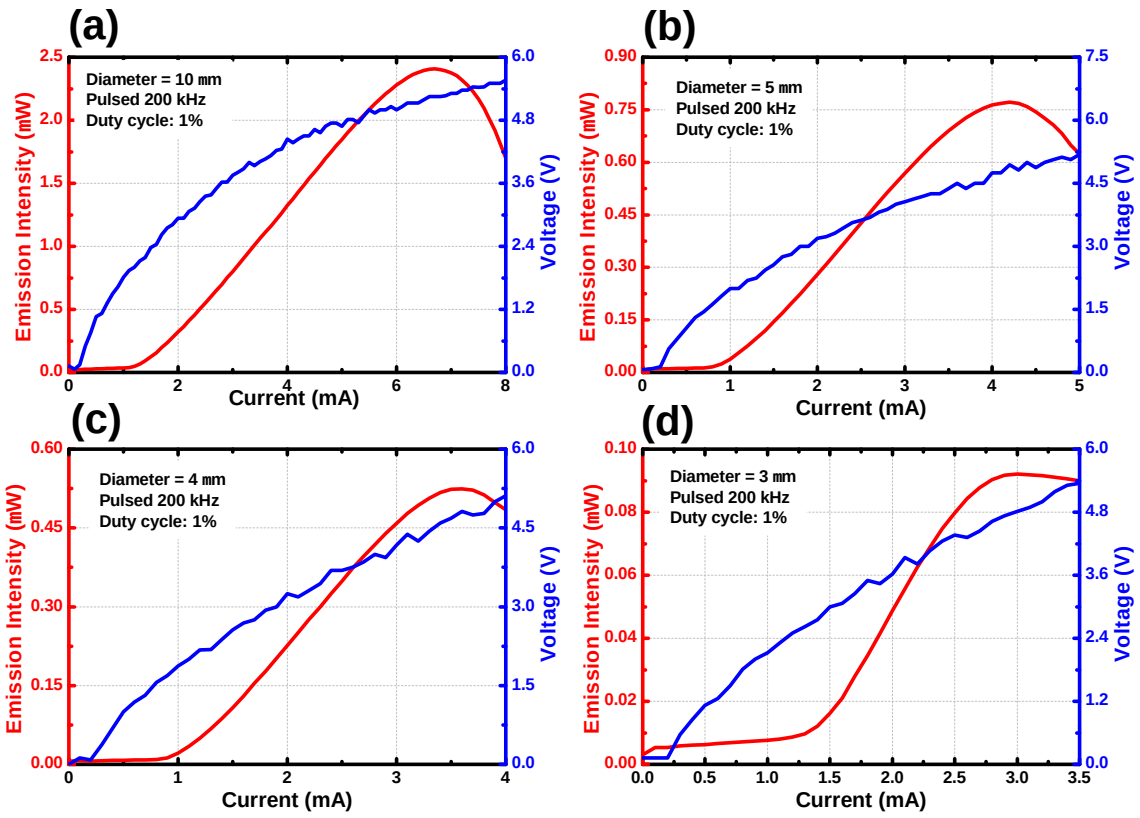

Figure 6.13: L-I-V curves of QW devices with different diameters (a) 10 μm, (b) 5 μm, (c) 4 μm, and (d) 3 μm. The testing condition was pulsed current injection with repetition rate 200 kHz and duty cycle 1 %. No active cooling was performed and the devices were tested at room temperature.

Compared to the data of QD devices in the previous section, the QW devices with the same size show a lower threshold current (or threshold current density) due to the complete two dimensional filling in the transverse direction. The transverse confinement factor, therefore, differs a lot for QW devices and QD devices. Assuming the same loss from the material and the radiation (i.e. same α_i and α_m) for QD and QW device structures, due to the larger transverse confinement factors of QW, the QW active materials usually show a larger modal gain compared to the QD materials. Figure 6.14 shows the comparison of the threshold current densities and the corresponding threshold currents under the same testing environment. The temperature was controlled by a thermoelectrically cooled copper heat sink.

Figure 6.15(a) shows the temperature-dependent L-I curves under pulsed current injection

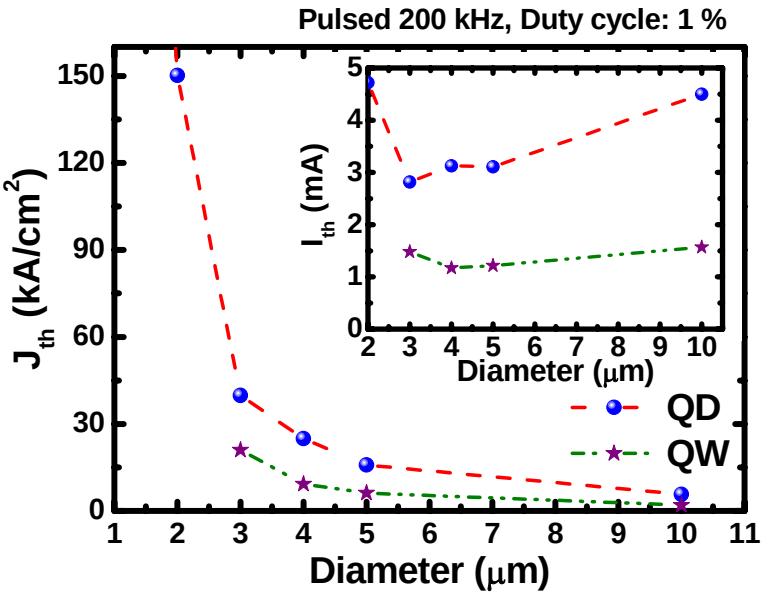

Figure 6.14: The comparison of QD size-dependent threshold current densities with those of quantum wells. The testing condition was pulsed electrical injection with a repetition rate of 200 kHz and duty cycle of 1 %. The samples were kept at room temperture without active cooling. The collection is through the substrate.

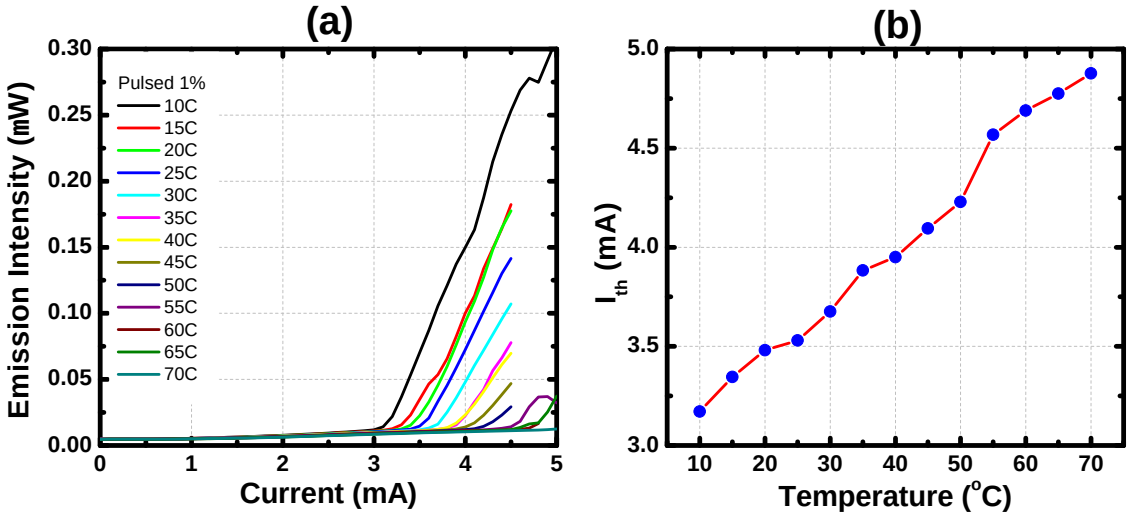

Figure 6.15: (a) Temperature-dependent L-I curves of QD metal-cavity microlasers under pulsed current injection (1 % duty cycle). The diameter of the device is 4 μm. (b) The threshold currents at different tempertaures. A positve charactersitic temperature is observed due to the pulsed operation and the metal cavity, which minimize the heat generation.

with duty cycle of 1 %. The device lases from 10 ^{o}C up to 70 ^{o}C (limited by the equipment). Due to the pulsed operation and metal-assisted heat removal, the heating effect was not obvious and the threshold currents exhibit a monotonic increase. Under this configuration, the gain spectrum is less sensitive to the current heating compared to the continuous-wave case which usually results in a negative characteristic temperature [58]. Figure 6.16 shows the QW metal-cavity microlaser results on the temperature L-I of a 4 μm devices for comparison. The devices lase with a lower threshold current and quickly saturate at around 2.2 mA. A positive chracteristic temperature was also observed in the QW case.

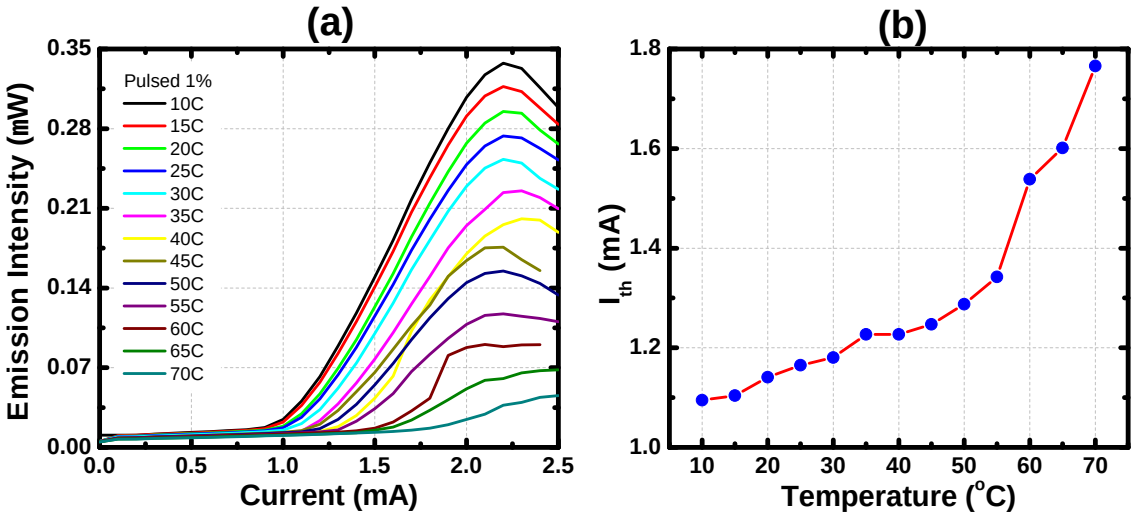

Figure 6.16: (a) Temperature-dependent L-I curves of QW metal-cavity microlasers under pulsed current injection (1 % duty cycle). The diameter of the device is 4 μm. (b) The threshold currents at different tempertaures. Compared to the QD devices, the threshold current is higher, however, the saturation occurs at higher current densities.

6.3 Toward the Realization of Metal-Cavity Nanolasers

The basic principles and demonstrations are shown in previous chapters. To realize the size-reduction, several approaches can be used. The general idea is to shrink the size, either laterally or vertically, and at the same time, to keep the quality factor at a decent value for laser action. Figure 5.1 in previous chapter shows the general idea of reducing the number

of DBR pairs to have a shorter pillar structure. As shown in Fig. 6.17, a lateral reduction can be made by reducing the diameter of the pillar; examples are shown in the previous sections for both QD and QW devices. Figure 6.18 shows the SEM images describing the size reduction through reducing the number of DBR pairs. The optimization can be made through adjusting the optical buffer layers to reduce the metal loss and fine-tuning the metal thicknesses. The main goal is to achieve a low volume of λ_0^3 with an output of 2 μW at room temperature. Redesigning the structure for higher optical feedback can also be done.

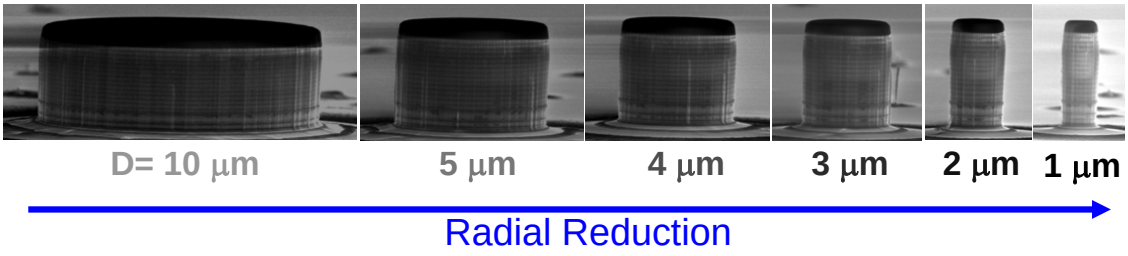

Figure 6.17: Scanning electron micrographs showing the diameter reduction from 10 μm to 1 μm.

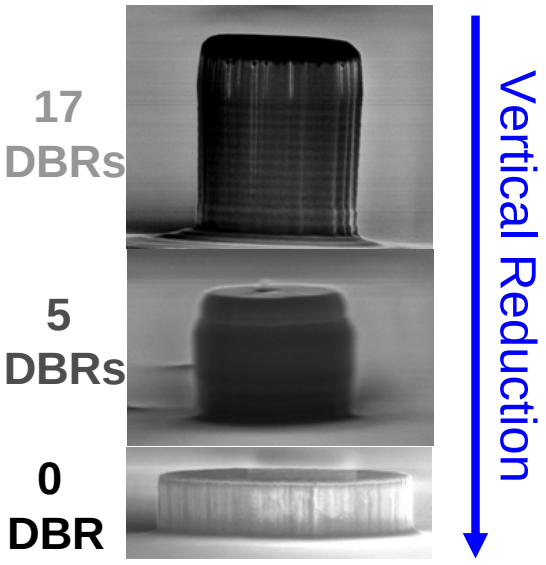

Figure 6.18: Scanning electron micrographs (SEMs) showing reduction of the number of DBR pairs from 17 pairs to 0 pair.

CHAPTER 7

OUTLOOK

To realize future photonic circuits with better performance than the current electronic platforms, future work such as high speed capability and parallel processing (array) remain open for metal-cavity nanolaser research. There are a lot of advantages of making ultrasmall lasers such as thresholdless current with almost zero power consumption. Nanolasers with a metal cavity can reduce the optical volume below the diffraction limit with the help of surface plasmon resonance. Also, with the use of the metal, it is possible to have a crosstalk-free environment for dense photonic integration. To further reduce the size, the metal reflectors are designed to replace or integrate with the reduced number of DBR pairs based on our strategy. A pure metal mirror without the DBR can be used, provided that special care is taken with the design of its thickness. To have good laser output power, the thickness of the metal reflector should be optimized. Recently, several ideas of metal-cavity nanolasers were proposed and some of them have been experimentally realized. To have a technology impact, the high speed properties should be studied. Recent results on high speed VCSEL have already shown the possibility of reaching 40 Gb/s for optical interconnect applications [58,59]. Further improvement can be made by using quantum dots as the active media; in addition, the compact size of nanolasers or nanoLEDs have been shown theoretically to improve the high speed modulation bandwidth [60,61]. With the introduction of metal, the loss increases (or equivalently, photon lifetime reduces) and can potentially lead to a higher modulation speed [62]. A proper design for high speed realization of metal-cavity nanolasers should involve an extensive investigation on the contact design since the compact size will usually show a capacitance limit. A design model for contact layout will be an important future

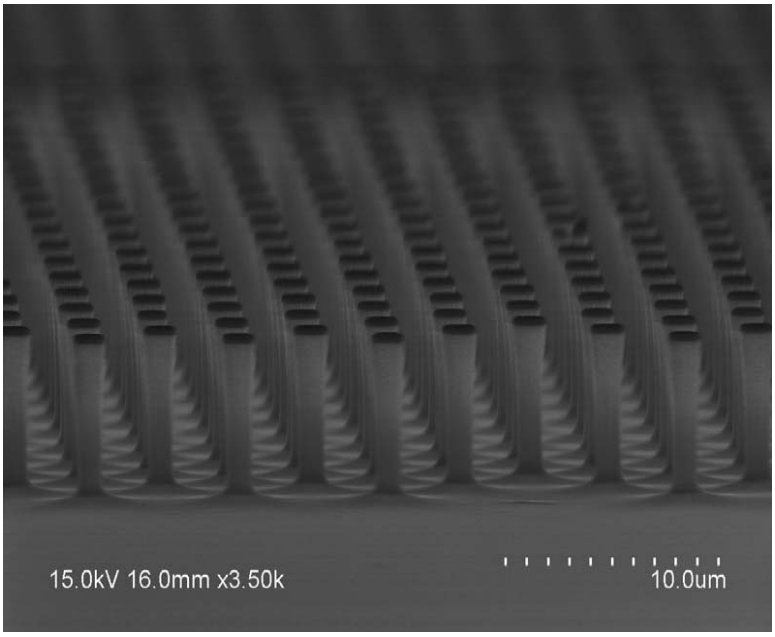

Figure 7.1: SEM showing a closed-packed array. With metal shielding, these devices could potentially work individually or coherently.

activity on metal-cavity nanolasers. The tremendous amount of data transmission nowadays all relies on the parallel processing on the electronic platform. The photonic counterpart, because of the size and crosstalk, cannot be directly integrated with current electronic platforms which are usually much smaller in size. The metal-cavity nanolasers, with complete metal coverage, would help the increase of density of devices. Figure 7.1 shows one example of a surface-emitting micropillar array. The application of metal can potentially push the distance between adjacent devices to the penetration depth of metal and give a crosstalk-free environment. The surface-emitting configuration also makes the alignment and parallel coupling a lot easier. With metal shielding, those devices could potentially work individually or coherently. This thesis work gives the basic idea of metal-cavity surface-emitting nanolasers and shows their promising future as a building block for the next generation photonic integrated circuits. The photonic circuits should have better thermal management, a higher modulation speed, and be more energy efficient if realized with metal-cavity lasers.

REFERENCES

[1] T. H. Maiman, *Nature*, vol. 187, p. 493, 1960.

[2] R. N. Hall, G. E. Fenner, J. D. Kingsley, T. J. Soltys, and R. O. Carlson, *Phys. Rev. Lett.*, vol. 9, p. 366, 1962.

[3] M. I. Nathan, W. P. Dumke, G. Burns, J. F. H. Dill, , and G. Lasher, *Appl. Phys. Lett.*, vol. 1, p. 62, 1962.

[4] J. N. Holonyak and S. F. Bevacqua, *Appl. Phys. Lett.*, vol. 1, p. 82, 1962.

[5] T. M. Quist, R. H. Rediker, R. J. Keyes, W. E. Krag, B. Lax, A. L. McWhorter, and H. J. Zeiger, *Appl. Phys. Lett.*, vol. 1, p. 91, 1962.

[6] H. Soda, K. Iga, C. Kitahara, and Y. Suematsu, *Jpn. J. Appl. Phys.*, vol. 18, p. 2329, 1979.

[7] A. F. J. Levi, R. E. Slusher, S. L. McCall, T. Tanbun-Ek, D. L. Coblentz, and S. J. Pearton, *Electron. Lett.*, vol. 28, p. 1010, 1992.

[8] H. G. Park, S. H. Kim, S. H. Kwon, Y. G. Ju, J. K. Yang, J. H. Baek, S. B. Kim, and Y. H. Lee, *Science*, vol. 305, p. 1444, 2004.

[9] D. A. B. Miller, *Proc. IEEE*, vol. 97, p. 1166, 2009.

[10] S. L. Chuang and D. Bimberg, *IEEE Photon. J.*, vol. 3, p. 288, 2011.

[11] P. Garrou, "Intel's Paniccia points to optical interconnect: Applied continues move into packaging," Apr. 2011. [Online]. Available: http://www.electroiq.com/blogs/insights_from_leading_edge/2011/04/ iftle-46-3dic-at-date-2011-intel-s-paniccia-points-to-optical-interconnect-applied-continues-mov.html

[12] K. Skaugen, "Petascale to exascale: Extending Intel's HPC commitment," in *ISC*, 2010.

[13] K. Nozaki, S. Kita, and T. Baba, *Opt. Express*, vol. 15, p. 7506, 2007.

[14] R. M. Ma, R. F. Oulton, V. J. Sorger, G. Bartal, and X. Zhang, *Nat. Mat.*, vol. 10, p. 110, 2011.

[15] C. Y. Lu, S. W. Chang, S. L. Chuang, T. D. Germann, and D. Bimberg, *Appl. Phys. Lett.*, vol. 96, p. 251101, 2010.

[16] C. Y. Lu, S. W. Chang, S. L. Chuang, T. D. Germann, U. W. Pohl, and D. Bimberg, *Semicond. Sci. Technol.*, vol. 26, p. 014012, 2011.

[17] S. W. Chang, C. Y. Lu, S. L. Chuang, T. D. Germann, U. W. Pohl, and D. Bimberg, *IEEE J. Sel. Top. Quantum Electron.*, vol. 17, p. 1681, 2011.

[18] C. Y. Lu, S. L. Chuang, A. Mutig, and D. Bimberg, *Opt. Lett.*, vol. 36, pp. 2447–2449, 2011.

[19] K. Yu, A. Lakhani, and M. C. Wu, *Opt. Express*, vol. 18, p. 8790, 2010.

[20] S. H. Kwon, J. H. Kang, C. Seassal, S. K. Kim, P. Regreny, Y. H. Lee, C. M. Lieber, and H. G. Park, *Nano Lett.*, vol. 10, p. 3679, 2010.

[21] M. P. Nezhad, A. Simic, O. Bondaenko, B. Slutsky, A. Mizrahi, L. Feng, V. Lomakin, and Y. Fainman, *Nat. Photon.*, vol. 4, p. 395, 2010.

[22] M. T. Hill, Y. S. Oei, B. Smalbrugge, Y. Zhu, T. deVries, P. J. van Veldhoven, F. W. M. van Otten, T. J. Eijkenmans, J. P. Turkiewicz, H. de Waardt, E. J. Geluk, S. H. Kwon, Y. H. Lee, R. Notzel, and M. K. Smit, *Nat. Photon.*, vol. 1, p. 589, 2007.

[23] M. T. Hill, M. Marell, E. S. P. Leong, B. Smalbrugge, Y. Zhu, M. Sun, P. J. van Veldhoven, E. J. Geluk, F. Karouta, Y. Oei, R. Notzel, C. Z. Ning, and M. K. Smit, *Opt. Express*, vol. 17, p. 11107, 2009.

[24] C. Manolatou and F. Rana, *IEEE J. Quantum Electron.*, vol. 44, p. 4535, 2008.

[25] J. H. Lee, A. Simic, M. Khajavikhan, O. Bondarenko, Q. Gu, M. P. N. B. Slutsky, and Y. Fainman, "Electrically pumped subwavelength metallo-dielectric laser with low threshold gain," in *CLEO:2011 -Laser Applications to Photonic Applications, OSA Technical Digest (CD) (Optical Society of America, 2011)*, 2011.

[26] J. L. Jewell, N. A. Olsson, S. L. McCall, Y. H. Lee, A. Scherer, J. P. Harbison, and L. T. Florez, *Opt. Eng.*, vol. 29, p. 210, 1990.

[27] W. H. Hofmann, P. Moser, P. Wolf, A. Mutig, M. Kroh, and D. Bimberg, "44 gb/s vcsel for optical interconnects," in *Optical Fiber Communication Conference, OSA Technical Digest (CD) (Optical Society of America)*, 2011.

[28] R. Safaisini, J. R. Joseph, and K. L. Lear, *IEEE J. Quantum Electron.*, vol. 46, p. 1590, 2010.

[29] M. Motoyoshi, *Proc. IEEE*, vol. 97, p. 43, 2009.

[30] N. W. Aschcroft and N. D. Mermin, *Solid State Physics*. Brooks/Cole Thomson Learning, 1976.

[31] A. Mizrahi, V. Lomakin, B. A. Slutsky, M. P. Nezhad, L. Feng, and Y. Fainman, *Opt. Lett.*, vol. 33, pp. 1261–1263, 2008.

[32] K. Ding, Z. Liu, L. Yin, H. Wang, R. Liu, M. T. Hill, M. J. H. Marell, P. J. van Veldhoven, R. Notzel, and C. Z. Ning, *App. Phys. Lett.*, vol. 98, p. 231108, 2011.

[33] J. A. Kong, *Electromagnetic Wave Theory*, 2nd ed. Cambridge, MA: EWM, 2008.

[34] L. Novotny and C. Hafner, *Phys. Rev. E*, vol. 50, p. 4094, 1994.

[35] P. B. Johnson and R. W. Christy, *Phys. Rev. B*, vol. 6, p. 4370, 1972.

[36] S. Adachi, *J. Appl. Phys.*, vol. 53, p. 5863, 1982.

[37] S. W. Chang, T. R. Lin, and S. L. Chuang, *Opt. Express*, vol. 18, p. 15039, 2010.

[38] S. W. Chang and S. L. Chuang, *IEEE J. Quantum. Electron.*, vol. 45, p. 1014, 2009.

[39] S. L. Chuang, *Physics of Photonic Devices*, 2nd ed. Hobokken, NY: Wiley, 2009.

[40] C. Y. Lu and S. L. Chuang, *Opt. Express*, vol. 19, p. 13225, 2011.

[41] A. N. AL-Omari, G. P. Carey, S. Hallstein, J. P. Watson, G. Dang, and K. L. Lear, *IEEE Photon. Technol. Lett.*, vol. 18, p. 1025, 2006.

[42] A. N. AL-Omari and K. L. Lear, *IEEE Photon. Technol. Lett.*, vol. 17, p. 1767, 2005.

[43] R. Pu, C. W. Wilmsen, K. M. Geib, and K. D. Choquette, *IEEE Photon. Technol. Lett.*, vol. 11, p. 1554, 1999.

[44] T. D. Germann, A. Strittmatter, U. W. Pohl, D. Bimberg, J. Rautiainen, M. Guina, and O. G. Okhotnikov, *J. Cryst. Growth.*, vol. 310, p. 5182, 2008.

[45] K. J. Greenberg, J. A. Summers, and J. A. Hudgings, *IEEE Photon. Technol. Lett.*, vol. 22, p. 655, 2010.

[46] L. A. Coldren and S. W. Corzine, *Diode Lasers and Photonic Integrated Circuits.* New York: Wiley, 1995.

[47] M. H. MacDougal, J. Geske, C. K. Lin, A. E. Bond, and P. D. Dapkus, *IEEE Photon. Technol. Lett.*, vol. 10, p. 15, 1998.

[48] C. S. Lee, S. W. Lee, and S. L. Chuang, *IEEE Trans. Microw. Theory Tech.*, vol. 34, pp. 773–785, 1986.

[49] S. L. Chuang, C. Y. Lu, and A. Matsudaira, "Metal-cavity nanolasers," in *OFC*, 2012.

[50] J. A. Kong, *Electromagnetic Wave Theory.* Cambridge, MA: EWM, 2008.

[51] J. D. Jaclson, *Classical Electrodynamics*, 3rd ed. New York: Wiley, 1989.

[52] R. S. Elliott, *Antenna Theorty and Design.* New Jersey, NJ: Prentice-Hall, 1981.

[53] P. Berini, *Phys. Rev. B*, vol. 61, pp. 10 484–10 503, 2000.

[54] E. Yablonvitch, C. E. Zah, T. J. Gmitter, and M. A. Koza, *Appl. Phys. Lett.*, vol. 60, pp. 371–373, 1992.

[55] F. Hopfer, A. Mutig, G. Fiol, M. Kuntz, V. A. Shchukin, V. A. Haisler, T. Warming, E. Stock, S. S. Mikhrin, I. L. Krestnikov, D. A. Livshits, A. R. Kovsh, C. Bornholdt, A. Lenz, H. Eisele, M. Dahne, N. N. Ledentsov, and D. Bimberg, *IEEE J. Sel. Top. Quantum Electron.*, vol. 13, pp. 1302–1308, 2007.

[56] F. Hopfer, A. Mutig, M. Kuntz, G. Fiol, D. Bimberg, N. N. Ledentsov, S. S. Mikhrin, D. A. Livshits, I. L. Krestnikov, A. R. Kovsh, N. D. Zakhorov, and P. Werner, *Appl. Phys. Lett.*, vol. 89, p. 141106, 2006.

[57] D. R. Matthews, H. D. Summers, P. M. Smowton, and M. Hopkinson, *Appl. Phys. Lett.*, vol. 81, p. 4909, 2002.

[58] A. Mutig, S. A. Blokhin, A. M. Nadtochiy, G. Fiol, J. A. Lott, V. A. Shchukin, N. N. Ledentsov, and D. Bimberg, *Appl. Phys. Lett.*, vol. 95, p. 131101, 2009.

[59] D. Bimber and U. W. Pohl, *Mat. Today*, vol. 14, pp. 388–397, 2011.

[60] T. Suhr, N. Gregersen, K. Yvind, and J. Mork, *Opt. Express*, vol. 18, pp. 11 230–11 241, 2010.

[61] E. Yablonovitch, "Metal optics, optical antennas, and spontaneous hyper-emission," in *Nanotechnology (IEEE-NANO), 2010 10th IEEE Conference on*, aug. 2010, pp. 13 –14.

[62] Y. Yamamoto, S. Machida, and G. Bjork, *Phys. Rev. A*, vol. 44, pp. 657–668, 1991.